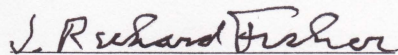THE CONNECTION BETWEEN
GALAXY KINEMATICS AND HI LINE WIDTHS
AS APPLIED TO THE DISTANCE SCALE
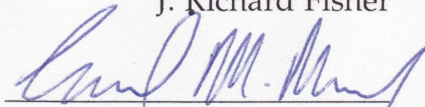
Alok Singhal
Haily Mandi, Gurgaon, India

B.Tech., Indian Institute of Technology, Kanpur, India – 1999
M.S., University of Virginia, Charlottesville, VA – 2003

A Dissertation Presented to the Graduate
Faculty of the University of Virginia
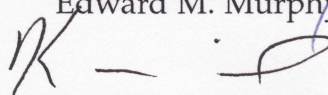in the Candidacy for the Degree of
Doctor of Philosophy

Department of Astronomy
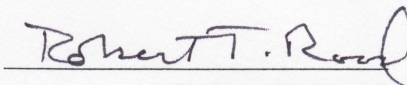
University of Virginia
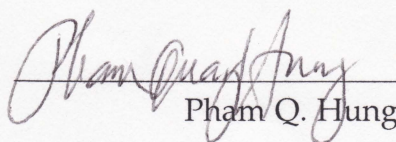May , 2008

J. Richard Fisher

Edward M. Murphy

Karen O'Neil

Robert T. Rood

Pham Q. Hung

ABSTRACT

I have created a 3-dimensional model of neutral hydrogen (HI) in disk galaxies, in order to better understand galaxy kinematics and the Tully-Fisher (TF) relationship. The model uses data from existing observations of galaxies (aperture synthesis and single-dish) to calculate some of their observed properties, such as single-dish line profiles, channel maps, and position-velocity diagrams. These can then be compared with the actual observations to study the differences between them. The effect of changing various galaxy parameters (such as inclination, and turbulent motion) on these quantities can then be studied. The model can also be used to study the effect of the parameters and commonly used corrections on the TF relation, such as turbulent motion correction and instrumental correction. Using the model, I have found that the the most commonly used turbulent motion corrections introduce a bias in the corrected line widths, particularly for galaxies with smaller rotation velocities. This can introduce a bias in the slope of the TF relation. Also, from the simulation, some galaxies show the presence of points on their line profiles where their HI line widths are independent of the turbulent motions. If such a point exists for all galaxies, then the determination of line widths at those points will require little or no correction due to tur-

bulent motion effects, and that width can be used in the TF relation instead of the commonly used line widths.

ACKNOWLEDGMENTS

> This is the only section that everyone who picks up your thesis will read. This is your chance to make obscure references to secret loves, damn various faculty members with faint praise, or be very mysterious by having no acknowledgments section at all so that everyone wonders what you're hiding.
>
> Robert Schulman and Virginia Fox,
> *How to Write a Ph.D. Dissertation*

I *did* think about having no acknowledgments section at all for a moment, not because I have no one to thank, but because this section is probably the hardest to write. For a long time this section simply read, 'Acknowledgments to be placed here.'

I would like to thank my advisor, Rick Fisher, first. He has been a great teacher and mentor to me. Over the past few years, I have asked him a lot of questions, many of them stupid, but he always answered them with such clarity (and patience, I am sure) that it made many of the 'complex questions' seem trivial after I understood his answers. He is an exceptional scientist, and I am always amazed at the breadth as well as the depth of his knowledge – from astronomy to complex engineering domains, including instrumentation, telescopes, and

programming. He answered my questions about galaxies, neutral hydrogen, observing strategies, program design, and even found a few of the critical bugs in my code when I was at my wits end looking for them (see the quote by Kernighan at the beginning of chapter 2). Finally, he read countless versions of my thesis, and gave valuable comments on them. Without his continued help and guidance, I could not have done this work.

Second, I would like to thank Ed Murphy. Ed's insights helped shape this project a lot. He looked at my insanely complicated plots and made sense out of them, suggested directions for my model, pointed out flaws in my arguments, and provided valuable suggestions on the content of the thesis. He is one of the best educators I have met, and can impart knowledge in an excellent way, whether it is to a group of 4-year old kids, or science teachers, or a graduate student who cannot understand calculation of position-velocity diagrams for disk galaxies.

I would also like to thank Karen O'Neil for her help with my work. She suggested features that I could build into my model, taught me about single-dish data processing and neutral hydrogen, and helped immensely with suggestions on how to find bugs in my model.

Next, thanks to the other members of my thesis committee, Robert Rood and Pham Hung. They read the thesis and provided many valuable suggestions.

Zhi-Yun Li helped me when I was in a fix regarding my course requirements for my graduation. It was great having him cool me down when I was all freaked out about how absent-minded I was, and for this I thank him.

Thanks are also due to the telescope operators at the Green Bank Telescope (GBT) and the Giant Meterwave Radio Telescope (GMRT). I could not have obtained the neutral hydrogen data for galaxies without their help and knowledge of the telescopes. Also, I thank Nirupam Roy at National Centre for Radio Astrophysics (NCRA), who observed many of the galaxies for me when I could not travel to the GMRT do conduct my own observations.

Thanks to Kiriaki Xiluri, Howard Powell, Tracy Halstead, Pat Murphy, Chris Clark, Wolfgang Baudler, and Darrel Schiebel for their help with computing issues.

Thanks to Virginia Bossong, Jackie Harding and Barbara Nicholson at UVa for helping me with funding questions, administrative issues, course registrations, and a lot of other countless issues.

I have to thank the wonderful workers at the NRAO Green Bank cafeteria. Not only they provided me with vegetarian food while I was there, they also gave me the master key when I locked myself out of my apartment for the n th time (the value of n is undisclosed to avoid embarrassment to the author). I can only imagine how many nights I would have spent in the Jansky Lab lounge at NRAO Green Bank if they didn't help me.

and backpacking trips I went on with him (how can I forget camping in a parking lot?!).

To Uday and Ravali for all the good times together, discussions on movies, Korean and Indian TV soaps, and the visibility of Pluto. To Neel and Jessie for cricket, hiking, bollywood and hollywood movies, and for great food. To Manish (Mau) and Archana for all the hospitality and the invitations of 'come over and play some tennis.' To Archana in particular for making delicious food from seemingly nothing to begin with.

Thanks to 'Saini' and Rinku – for being like a family away from India. The time I spent at your place, eating great Indian food, hanging out with Simrat, talking about all things Indian, and gossiping about the Indian community in Charlottesville helped me not miss India as much as I would have otherwise.

To my roommates Sri and Marios (Μάριος) – Sri, for being understanding when I left everything at home in disarray in the final few days of my defense, and for discussions on every topic under the sun: the US law, the Indian law, the characters in various TV programs, or the lack of lobbing being used by the professional tennis players. Marios, for all the jokes, including programming jokes (10 000 000+ errors in a program!), teaching me Greek (Μαλάκας!), and making awesome salad and lentil soup. Thanks to Molly for Piña Coladas, Christmas cookies, and numerous parties.

Thanks to my office mates in Charlottesville: to Greg for various discussions on astronomy, C, the department, and for his lecture notes from Quantum Physics class; to Howard for all stuff related to computing, and not burning my (non-software) files when I left them in his office for a period of $\sim$ 3 years; and to Libby for the story about the integral of the universe using hyperbolic functions.

Thanks are also due to my fellow astronomy grad students and other 'astro groupies' including Geneviéve de Messiéres, Jodie Morgan, Ricardo Muñoz, Jeff Oishi, Chan Park, Sangmo Tony Sohn, Joe Malone and Mosa.

Last, but not the least, I would like to thank everyone in my family. They provided constant support and encouragement throughout my graduate studies. Preeti is more than a sister to me – she is a friend, with whom I can talk to anytime. Arun has been a mentor and inspiration since I was a little kid, and he got me interested in numbers, mathematics, and science in general. Menka (I mean भाभी) for all the wishes and आशीर्वादs, and little Ahan for his utterances of चाचा. To Anuj, for all his practical advices, fights, and for great times together. And finally, words cannot express my gratitude toward my parents. They sacrificed a lot to get a good education for me, gave me their encouragement and support, and most importantly, their love, without which I would not be where I am today. Thank you!

CONTENTS

LIST OF FIGURES

LIST OF TABLES

LIST OF ACRONYMS

AIPS   Astronomical Image Processing System

BGPV   Bottinelli et al. (1983)

CCD   Charge-coupled device

CDS   Centre de Données astronomiques de Strasbourg

FWHM   Full-width at half-maximum

GBT   Green Bank Telescope

GMRT   Giant Meterwave Radio Telescope

HI   neutral hydrogen

IPAC   Infrared Processing and Analysis Center

LSB   low surface brightness

NASA   National Aeronautics and Space Administration

NCRA   National Centre for Radio Astrophysics

NED   NASA/IPAC Extragalactic Database

NGC   New General Catalogue of Galaxies

NRAO   National Radio Astronomy Observatory

SNR   signal-to-noise ratio

TF   Tully-Fisher

TFq   Tully & Fouqué (1985)

UGC   Uppsala General Catalogue of Galaxies

UML   Uson & Matthews (2003)

VLA   Very Large Array

VSR   Verheijen & Sancisi (2001)

WSRT   Westerbork Synthesis Radio Telescope

LIST OF SYMBOLS

For symbols that have more than one meaning in the text (such as *R*, W_c), the context in which the symbol is used disambiguates the meaning.

A Transition probability for the forbidden H**I** emission

a Semi-major axis

b Semi-minor axis

c Speed of light in vacuum, $2.997\,924\,58 \times 10^5\,\mathrm{km\ s^{-1}}$

d Distance to a galaxy

e_{corr} Corrected ellipticity

F Cumulative velocity distribution function

f Observed velocity distribution function

f_p Peak flux in the H**I** line profile

$f(s)$ Factor needed to give line-of-sight turbulent velocity from σ_z

g_1 Statistical weight of the lower level for H**I** emission

g_2 Statistical weight of the upper level for H**I** emission

h Planck's constant, $6.626\,068 \times 10^{-34}\,\mathrm{m^2\ kg\ s^{-1}}$

I Intensity of H**I** radiation

i Inclination angle of a galaxy

k Boltzmann constant, $1.380\,650\,3 \times 10^{-23}\,\mathrm{m^2\ kg\ s^{-2}\ K^{-1}}$

κ	Emmisivity
$k(l)$	Half-width of a Gaussian with dispersion 1 at l% of its peak
l	The level at which HI line width is measured
λ	Observed wavelength
λ_0	Rest-frame wavelength
M_{pg}	Absolute photographic magnitude of a galaxy
$M_\odot$	Mass of the sun, 1.98892×10^{30} kg
ν	Observed frequency
ν_0	Rest-frame frequency
$\nu_{H\textsc{i}}$	HI rest frequency, $1.420\,405\,751\,786 \times 10^9$ Hz
n_x	Number of cells in x-direction in the model
n_y	Number of cells in y-direction in the model
n_z	Number of cells in z-direction in the model
ψ	$0.5 \times$ FWHM, (defined by Giovanelli et al. 1997)
ψ	Galaxy rotation angle about the z-axis
q	Observed (optical) axial ratio of a disk galaxy
q_0	Intrinsic axial ratio of a disk galaxy
R	Maximum radius of a simulated galaxy
R	FWHM of the Gaussian representing instrumental resolution
r_{cyl}	Distance of a cell from the galaxy center, cylindrical coordinates
ρ	Surface HI density of a galaxy
S	Integrated flux, Jy km s^{-1}
s	σ_x / σ_z

σ_0	Line-of-sight turbulent velocity
σ_c	Dispersion of a Gaussian representing the convolution function due to turbulent motion and instrumental resolution broadening
σ_R	Dispersion of a Gaussian representing widening due to finite instrumental resolution
σ_x	Turbulent velocity along the x-axis
σ_y	Turbulent velocity along the y-axis
σ_z	Turbulent velocity along the z-axis
$S(v)$	Flux density as a function of the observed velocity
T	Morphological type of a galaxy
θ	Azimuthal angle
T_s	Spin temperature
$\Delta V(0)$	Corrected H$_I$ line width, as defined by Tully & Fisher (1977)
v_c	Circular speed
v_{flat}	Flat part of the rotation curve in a galaxy
v_{hel}	Heliocentric velocity of a galaxy
v_{los}	Line-of-sight velocity
v_{max}	Maximum rotation velocity in a galaxy
v_{opt}	Optical velocity
v_{radio}	Radio velocity
v_x	Velocity in the x-direction
v_y	Velocity in the y-direction
v_z	Velocity in the z-direction

δW_{20} Line profile broadening only because of finite instrumental resolution

W_{20} H I line width at 20% of the peak

W_{50} H I line width at 50% of the peak

W_c H I line profile width, corrected for inclination and maybe other effects

$W_{c,l}$ Parameter defining the transition region from linear to quadrature subtraction, accorting to TFq

W_l H I line width at l% of the peak

$W_{R,l}$ Turbulence corrected line width according to TFq

W_t Correction to the line width due to turbulent motions

x x-coordinate

y y-coordinate

z z-coordinate

z redshift

DEDICATION

To mom and dad

प्रणाम

1

INTRODUCTION

> 'Where shall I begin, please your Majesty?' he asked. 'Begin at the beginning,' the King said, gravely, 'and go on till you come to the end: then stop.'
>
> Lewis Carroll, *Alice's Adventures in Wonderland*

In this chapter, I will briefly describe the neutral hydrogen (H I) radiation and its properties. Then, I discuss the Tully-Fisher (TF) relation to find galaxy distances. Later, I will discuss recent developments in using the TF relation.

1.1 NEUTRAL HYDROGEN RADIATION

Neutral hydrogen consists of a single, uncharged, hydrogen atom. In addition to their other properties, the electron and the proton in an hydrogen atom have spins, which can either be parallel, or anti-parallel. These two configurations have slightly different ener-

gies, with the state with parallel spins having the lower energy. The frequency of the resulting line is (Rohlfs & Wilson, 2000):

$$\nu_{\mathrm{HI}} = 1.420\,405\,751\,786 \times 10^9 \, \mathrm{Hz}. \tag{1.1}$$

The transition has a very low probability of $A = 2.87 \times 10^{-15}\,\mathrm{s}^{-1}$, or equivalently, a half-life of $\sim 1.11 \times 10^7$ yr. The frequency, ν_{HI}, can be expressed in wavelengths as 21.1 cm, and therefore neutral hydrogen radiation is also known as 21-cm radiation.

Because of the very small transition probability, collisions have time to establish an equilibrium distribution in which the populations of the upper and lower levels (labeled 2 and 1 respectively) are given by the Boltzmann distribution:

$$\frac{N_2}{N_1} = \frac{g_2}{g_1} e^{-h\nu_{\mathrm{HI}}/kT_s}, \tag{1.2}$$

where k is the Boltzmann constant ($1.380\,65 \times 10^{-23}\,\mathrm{m}^2\,\mathrm{kg}\,\mathrm{s}^{-2}\,\mathrm{K}^{-1}$), h is the Planck's constant ($6.626\,068 \times 10^{-34}\,\mathrm{m}^2\,\mathrm{kg}\,\mathrm{s}^{-1}$), T_s is the equilibrium excitation temperature, known as the *spin temperature*, and g_2 and g_1 are the statistical weights of the upper and the lower levels, $g_2/g_1 = 3$ (Longair, 1994). Precise measurements of T_s are difficult, with the 'classical' adopted value being $T_s \approx 125\,\mathrm{K}$ (Rohlfs & Wilson, 2000). For neutral hydrogen radiation, $h\nu_{\mathrm{HI}}/k = 7 \times 10^{-2}\,\mathrm{K} \ll T_s$, and equation 1.2 gives $N_2/N_1 = 3$.

Assuming the H<small>I</small> region to be *optically thin* (nearly transparent), the *emissivity* of the gas, κ is then

$$\kappa = \frac{g_2}{g_1 + g_2} N_H A h \nu_{\mathrm{H\,I}} = \frac{3}{4} N_H A h \nu_{\mathrm{H\,I}}, \qquad (1.3)$$

where $N_H = N_1 + N_2$ is the total number of H<small>I</small> atoms. This gives the line intensity of radiation in a particular direction l as:

$$I = \frac{3}{16\pi} A h \nu_{\mathrm{H\,I}} \int N_H \mathrm{d}\, l, \qquad (1.4)$$

The integral has to be taken along the line of sight and also in frequency since the H<small>I</small> radiation is Doppler-broadened due to line of sight motions of hydrogen atoms. Carrying out the integral in equation 1.4, and using S_ν, where S_ν is the flux density (see Dickey 2002) gives:

$$\frac{M_{\mathrm{H\,I}}}{M_\odot} = 2.356 \times 10^5 d^2 \int S(v) \mathrm{d}\, v, \qquad (1.5)$$

where $M_\odot$ is the mass of the sun ($1.988\,92 \times 10^{30}$ kg), d is the distance in Mpc, and $S(v)$ is the flux density as a function of the observed velocity in Jy ($1\,\mathrm{Jy} = 10^{-26}\,\mathrm{W\,m^{-2}\,Hz}$).

Although the probability a single hydrogen atom undergoing spin-flip to produce the above radiation is very low, because of the high number of neutral hydrogen atoms in galaxies, the H<small>I</small> radiation from galaxies can be observed at the earth with radio telescopes. In disk galaxies, the mass of neutral hydrogen can be about $\sim 10^{10}\,\mathrm{M_\odot}$, see Roberts 1975).

1.2 GALAXY CLASSIFICATION

The base galaxy classification scheme follows Hubble's early classification of galaxies (Hubble, 1926). Hubble arranged galaxies in the famous 'tuning fork' diagram (see Figure 1.1), with elliptical galaxies on the left, and spiral galaxies on the right. In this scheme, the elliptical galaxies are noted as En, where n is a number ranging from 0 to 7. For an elliptical galaxy with observed axial ratio b/a (a is the semi-major axis, and b is the semi-minor axis), $n = 10(1 - b/a)$. Thus, circular elliptical galaxies are denoted $E0$, and ellipticals with highly elongated form are $E7$. To the right of $E7$ galaxies are lenticular galaxies, which show smooth central brightness condensation similar to elliptical galaxies, surrounded by a large region of less steeply declining brightness. These galaxies are sometimes denoted $S0$ or $SB0$, depending upon the presence of a central bar in them ($SB =$ barred).
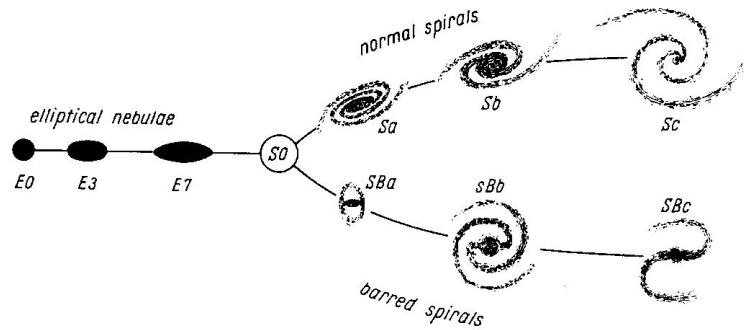
Figure 1.1: The 'tuning fork' diagram, reprinted from Sandage (1975).

After the $S0$ galaxies come the regular spiral (disk) galaxies. These show winding spiral arms and a central nucleus. They are denoted

by the letter *S*. The regular spiral galaxies can have a bar in the center, in which case they are denoted *SB*. Depending upon the relative brightness of the central bulge, the tightness of the spiral arms, and the degree of resolution of these arms into stars and emission nebulae, the spiral galaxies (*S* and *SB*) are further divided into subtypes. Spiral galaxies *Sa* and *SBa* have a conspicuous central bulge, and tightly wound spiral arms. Similarly, *Sd* and *SBd* galaxies have a small central bulge, and loose spiral arms. Spiral galaxies to the left in Figure 1.1 are called early-type galaxies, while galaxies to the right are known as late-type galaxies.

There have been many revisions of the base classification system. de Vaucouleurs (de Vaucouleurs, 1959) stated that the spiral galaxies can be further classified depending upon the presence of a ring around their nuclei, and whether spiral arms start from such a ring (*r* galaxies) or from the nucleus (*s* galaxies). The classification system of de Vaucouleurs is shown in Figure 1.2. For a full review of the development of galaxy classification according to morphology, and detailed description of those schemes, see Sandage (1975).

Figure 1.3 shows an the Hubble tuning fork diagram with real galaxies as examples (Keel, 2008).

The *morphological type T* of a galaxy is a number ranging from -5 for elliptical galaxies to 10 for irregular galaxies (*Irr I*). For disk galaxies, the morphological type goes from -2 for *S*o galaxies (lenticular galaxies) to 8 for *Sc–Irr* galaxies (see de Vaucouleurs & de
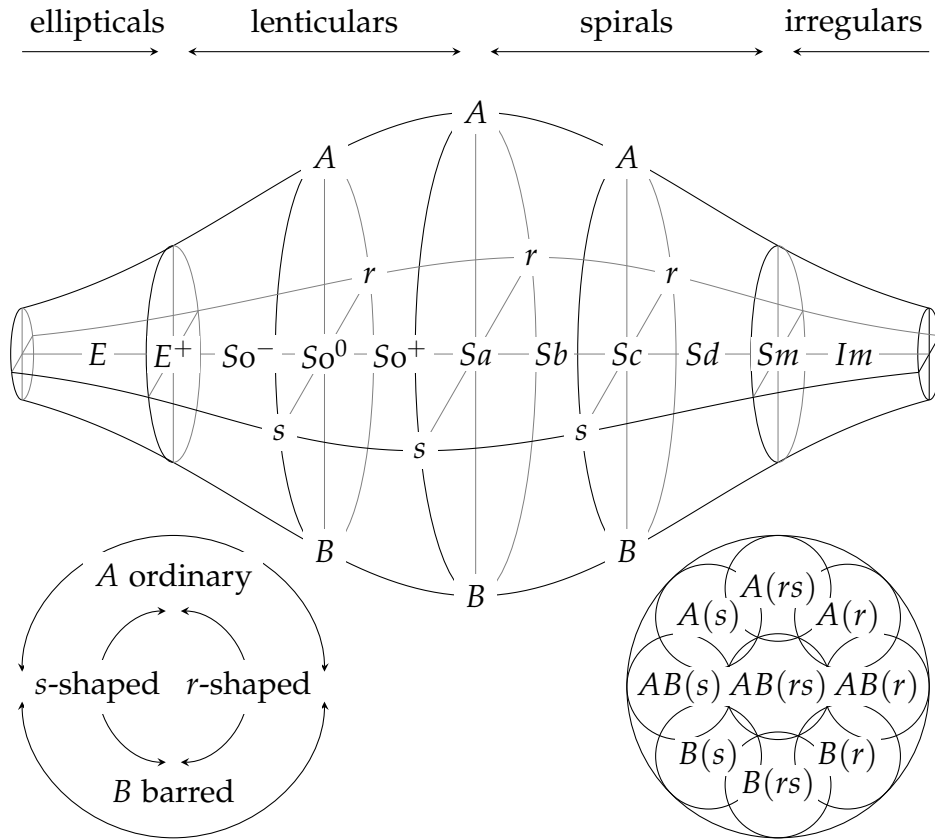
Figure 1.2: Galaxy classification diagram, as presented by de Vaucouleurs (1959). The elliptical galaxies are on the left, and spiral galaxies are on the right. *B* galaxies show bars, *A* do not. The *r* and *s* types are defined by whether the spiral arms start from the ring or the nucleus of a galaxy.
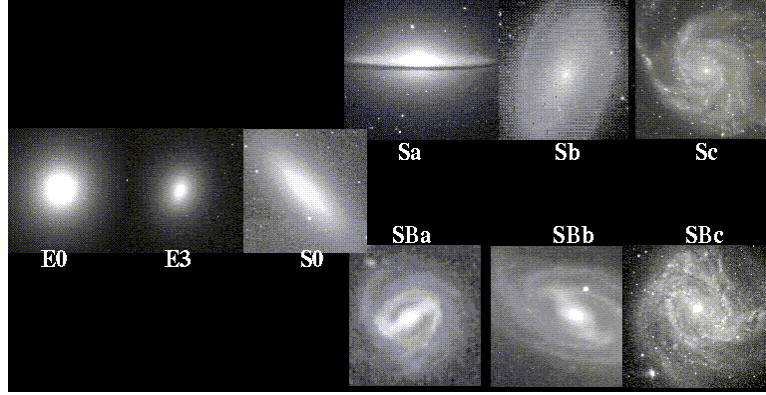
Figure 1.3: Hubble's tuning-fork diagram, from Keel (2008) using CCD images of galaxies.

Vaucouleurs 1972, RC2 hereafter, and Binney & Merrifield 1998 for more information).

1.3 OPTICAL AND RADIO VELOCITIES

In astronomy, two approximations of velocity are used by convention. *Optical* velocity is defined as:

$$v_{\text{opt}} = cz = c\frac{\lambda - \lambda_0}{\lambda_0} = c\frac{\nu_0 - \nu}{\nu}, \tag{1.6}$$

where c is the speed of light, z is the *redshift*, λ is the wavelength, and ν is the frequency. The values with subscript, 0, are the rest-frame values, and the unscripted values are the observed values.

Radio velocity is defined as:

$$v_{\text{radio}} = c\frac{\nu_0 - \nu}{\nu_0} = c\frac{\lambda - \lambda_0}{\lambda}. \tag{1.7}$$

Note that these two definitions of velocities are different from the relativistic Lorentz velocity v of the source, but they are nearly the same when $\lambda - \lambda_0 \ll \lambda_0$. The equation describing the relation between the observed frequency, the rest-frame frequency, and the relativistic velocity is:

$$\nu = \sqrt{\frac{1 - v/c}{1 + v/c}} \nu_0. \tag{1.8}$$

Using equations 1.6 and 1.8,

$$v_{\text{opt}} = c \left(\sqrt{\frac{1 + v/c}{1 - v/c}} - 1 \right). \tag{1.9}$$

In all the above cases, velocity is positive if the source and the receiver are moving away from each other.

1.4   HI LINE PROFILES

The stars, as well as neutral hydrogen in a disk galaxy, travel in nearly circular orbits around the galactic center. The rotation speed of a hypothetical star at a distance r from the center, $v_c(r)$, plotted as a function of r is called the *rotation curve* of the galaxy.

In general, the extent of neutral hydrogen in disk galaxies extends well beyond the optical disk. The rotation curves of most disk galaxies are more or less flat, except near the center, where the circular speed is zero. The fact that the rotation curves of disk galaxies do not fall

off expected from the gravitational potential due to the known mass of stars and gas suggests that most disk galaxies have dark matter halos that extend well beyond the observed size of the galaxy. In fact, for some galaxies, the rotation curve has a slight positive slope even at very large radii.

The spectrum of H I radiation from disk galaxies is broadened by the rotation of the gas in the disk. The amount of line broadening is dependent on the rotation velocity of the galaxy. Usually, the line profile from a galaxy is plotted as a function of velocity instead of frequency, because any given frequency can be mapped to a velocity as described in the last section. For H I line profiles, the *optical* definition of velocity is used by convention. The line-profile width can be specified as the width at a certain fraction of the peak of the profile. The most commonly used fraction is 20% of the peak, although 50%, and other values have also been used. The line-profile width at a percentage l of the peak is denoted as W_l. As an example, Figure 1.4 shows the H I line profile for the galaxy UGC 7321 (from Uson & Matthews 2003; UML hereafter).

Single dish radio telescopes are most commonly used to observe H I line profiles of galaxies. This is because single dish telescopes have a beam size of a few to about 20 arcminutes at 21 cm, and therefore most galaxies fall in one beam of the telescope. Single dish telescopes also make it easier to detect large-scale structure in galaxies, which can be missed with an interferometer.
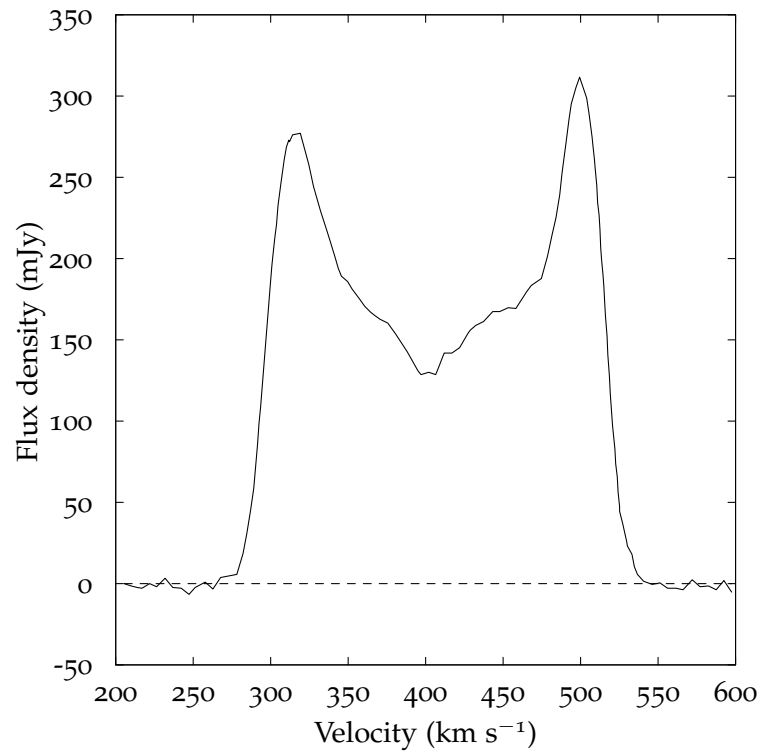
Figure 1.4: UGC 7321 line profile. Optical velocity is plotted on the *x*-axis, and flux density is on the *y*-axis. Flux density is measured in milli Janskys (mJy).

1.5 TULLY-FISHER RELATION

The absolute brightness of disk galaxies can be inferred from the width of their HI line profiles. The HI line-profile width of a galaxy is independent of its distance, since it depends only on factors such as HI density distribution, the rotation velocity, inclination angle, etc. An empirical connection between HI line width and absolute brightness can be used to determine the distances to disk galaxies. This connection is called the Tully-Fisher (TF) relationship (Tully & Fisher 1977).

Figure 1.5 shows the TF relation as published by Tully & Fisher (1977).
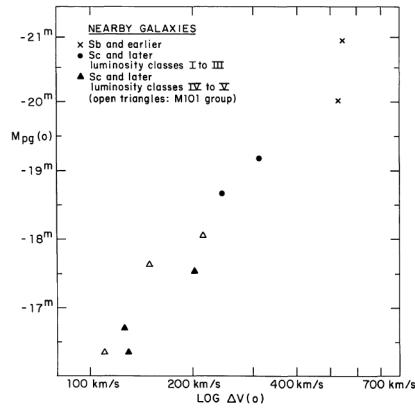
Figure 1.5: The Tully-Fisher relation as published by Tully & Fisher (1977). M_{pg} is the absolute photographic magnitude, and $\Delta V(o)$ is the corrected HI line-profile width at 20% of the peak. The figure shows nearby galaxies with previously well-determined distances.

Tully & Fisher (1977) gave the following relation between the absolute magnitude and line-profile width for the galaxies in their sample:

$$M = -6.25 \log W_{c,20} - 3.5 \qquad (1.10)$$

where $W_{c,20}$ is the inclination-corrected line width at 20% of the peak (see next section for information on these corrections).

TF relation can be used to calculate distances ranging from nearby galaxies to about 100 Mpc (megaparsecs), or about 100 times the distance to our nearest neighbor large galaxies. The beam size of even the largest single-dish radio telescopes at 21 cm is a few arcminutes, and beyond this distance, the angular size and separation of normal disk galaxies is small enough that there is a significant chance of confusion with other galaxies in the telescope beam.

A key issue with beam size is not missing any HI flux in the line profiles of nearby galaxies. Beam sizes that are smaller than the galaxy HI disk size will miss flux in the outer (faster rotating) parts of the galaxy, thus giving inaccurate line profiles (see Hewitt et al. 1983, Springob et al. 2005). Another related issue is that the pointing inaccuracies in the single dish telescopes can cause the observed flux to be smaller than the actual flux.

Usually, the line-profile width at 20% of the peak is used in the TF relations. For luminosities, Tully and Fisher used *B*-band luminosities, but various other optical and infrared bands have been used since

then. Particularly useful is the I band ($\lambda = 850\,$nm), because it minimizes extinction effects due to dust in galaxies.

A galaxy's inclination affects the TF relation in two ways. First, it determines the amount of inclination correction to be applied to the observed HI line widths. Second, it affects the corrections to the luminosity of a galaxy due to extinction. Higher inclination angles (more edge-on galaxies) result in lower corrections to the HI line widths (see section 1.7.1), but because of higher extinction due to dust absorption, it results in a higher correction to the luminosities (Giovanelli et al., 1997). The luminosities must also be corrected for extinction within our Galaxy (Burstein & Heiles, 1978). Internal extinction correction can be expressed as:

$$\Delta m_i = -\gamma \log(a/b), \qquad (1.11)$$

where a and b are the observed semi-major and semi-minor axes, m_i is the I band magnitude, and γ is a parameter that depends on the velocity width of the galaxy (see Giovanelli et al. 1997 for more information). For a detailed description of the type and amount of optical corrections involved, see Haynes et al. (1999).

The TF relationship is strictly empirical. For the past few years, there has been an effort to find a physical basis for the TF relationship. In particular, it has been suggested that the line-profile width, corrected for effects such as turbulent motions and broadening due to finite resolution of the telescope (see section 1.7) is related to the

maximum of the rotation velocity of the H$\textsc{i}$ disk, v_{max}. For some galaxies, v_{max} is different from the flat part of the rotation curve v_{flat}, and there is some evidence that the line-profile width correlates better with v_{flat} than v_{max} (Verheijen & Sancisi 2001, VSR hereafter).

1.6 ASYMMETRY IN H$\textsc{i}$ LINE PROFILES

After analyzing approximately 1700 H$\textsc{i}$ line profiles of galaxies from various surveys, Richter & Sancisi (1994) concluded that more than 50% of field spiral galaxies show asymmetries in their line profiles. The same result has since been confirmed by other investigators, using higher spatial resolution data (see Sancisi 1999 for a review, and also Haynes et al. 1998). The fraction of galaxies with asymmetric line profiles could be higher for galaxies in clusters and groups. The asymmetry in line profiles could result from many factors, such as high-velocity clouds, warping and flaring of the H$\textsc{i}$ layer, small companion galaxies in the main telescope beam, and telescope pointing errors (Haynes et al., 1998).

Asymmetric line profiles raise several questions on calibration of the TF relation, since calculating line-profile widths of such asymmetric profiles may not accurately estimate the maximum rotational velocity of these galaxies. The method used to determine line-profile widths in asymmetric galaxies is important because it is known that the galaxies with low H$\textsc{i}$ content show more asymmetric profiles (Ko-

rnreich et al., 2001), and any errors introduced in measured the corrected line widths for asymmetric galaxies will cause a bias in the TF relation.

1.7 CORRECTIONS TO THE LINE-PROFILE WIDTH

The observed HI line-profile width must at least be corrected for the inclination of the galaxy with respect to the line of sight and random motions of the gas before it can be used in the TF relation. In this section, I describe some of the corrections to HI line-profile widths that have been applied by investigators in the past. In chapter 4, the effect of these corrections on the line profiles created from the model is discussed.

1.7.1 *Inclination correction*

The *inclination angle* of a galaxy is defined as the angle between the normal to the galaxy disk and the line of sight (see Figure 1.6).

With this definition of inclination, the component of the observed line profile of a galaxy due to its planar rotation is narrowed by a factor $\sin i$, where i is the inclination angle. Thus, in order to calculate
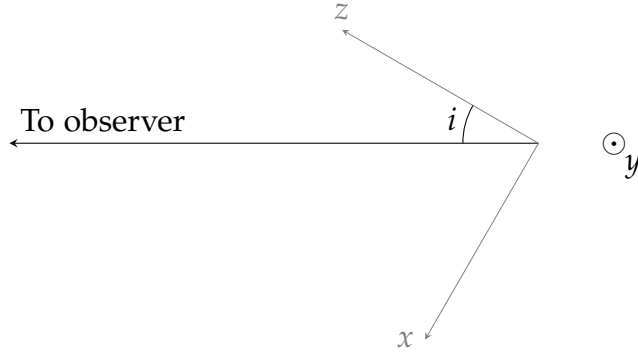
Figure 1.6: Inclination angle i of a galaxy. The galaxy disk is in x-y plane, and z-axis is normal to the disk.

the inclination-corrected width of the line profile, we need to divide the observed line-width by $\sin i$:

$$W_{c,l} = \frac{W_l}{\sin i} \qquad (1.12)$$

The inclination of a galaxy is determined from observations. Following Hubble (1926), the inclination angle of a galaxy is derived from its observed axis ratio ($q = b/a$, where a and b are the major and minor axis lengths of an ellipse describing a locus of constant surface brightness):

$$\cos^2 i = \frac{q^2 - q_0^2}{1 - q_0^2}. \qquad (1.13)$$

The parameter q_0 denotes the intrinsic axial ratio, determined from optical images of galaxies seen edge-on. The above definition of inclination saturates at 90° for $q = q_0$.

Hubble (1926) used and empirically derived value of $q_0 = 0.2$. The motivation behind choosing $q_0 = 0.2$ comes from observations of

various galaxies, and then using the average value of q for the most inclined galaxies (Holmberg 1946).

Heidmann et al. (1972) used two separate galaxy catalogs, Holmberg (1958) and de Vaucouleurs & de Vaucouleurs (1964) (BGC), and determined q_0 as a function of T for both. They showed that the value of q_0 is dependent on the morphological type T of a galaxy. They found that $q_0(\text{Holmberg}) \approx q_0(\text{BGC}) + 0.04$.

Bottinelli et al. (1983) (BGPV hereafter) used the same method used by Heidmann et al. (1972) on the *Second Reference Catalog of Bright Galaxies* (RC2), and obtained:

$$- \log q_0 = \begin{cases} 0.60 + 0.045T & \text{for } T \leq 7, \\ 0.65 & \text{for } T > 7. \end{cases} \tag{1.14}$$

Fouqué et al. (1990) used all the galaxies in the catalog of 2096 galaxies in the Vigro Cluster area (Binggeli et al., 1985), and not just the most inclined, to obtain:

$$- \log q_0 = \begin{cases} 0.43 + 0.053T & \text{for } T \leq 7, \\ 0.38 & \text{for } T > 7. \end{cases} \tag{1.15}$$

Giovanelli et al. (1997) considered the effect of *seeing* (full-width at half-maximum of a point source in an image due to atmospheric

turbulence) on the observed axial ratio, q. They define e_{corr} as the corrected *ellipticity* ($1 - a/b$, where a/b is the axial ratio), given by:

$$e_{corr} = 1 - \sqrt{\frac{(1 - \bar{e})^2 - \psi^2}{1 - \psi^2}}, \qquad (1.16)$$

where $\psi = 0.5\text{FWHM}$, and FWHM is the Full-width at half-maximum of the seeing disk. They used the value of e_{corr} to determine q. They chose $q_0 = 0.13$ for *Sbc* and *Sc* galaxies ($4 \leq T \leq 6$), and $q_0 = 0.2$ otherwise.

Using Monte-Carlo simulations, and assuming that q_0 has a Gaussian distribution for a given T, Yuan & Zhu (2004) derived two separate linear relations for q_0:

$$\log q_0 = \begin{cases} (-0.580 \pm 0.016) - (0.067 \pm 0.004)\, T & \text{for } T \leq 7, \\ (-2.309 \pm 0.347) + (0.185 \pm 0.040)\, T & \text{for } T > 7. \end{cases}$$

$$(1.17)$$

(There is a typo in their paper, where the equation above is written as $(-0.580 \pm 0.016) + (0.067 \pm 0.004)\, T$ for $T \leq 7$.)

To understand the effect of using these different definitions of q_0 on the derived value of inclination, see Figures 1.7 and 1.8. In Figure 1.8, the derived value of $1/\sin i$ (a factor that describes the amount of inclination correction) is plotted as a function of the observed axial ratio q, for three different values of q_0.
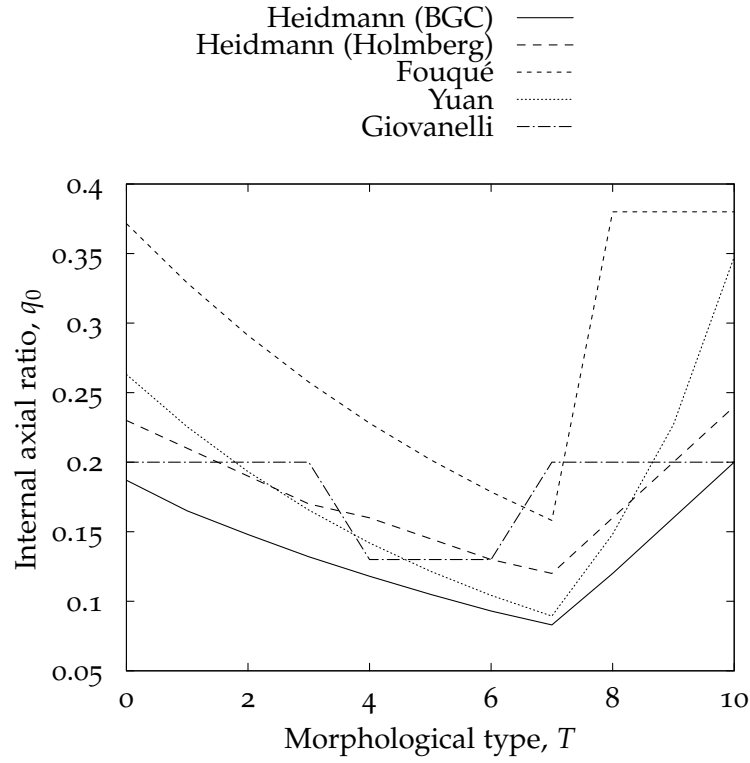
Figure 1.7: Variation of the intrinsic axial ratio, q_0 as a function of morphological type, T of a galaxy, as described by various authors (see text). *Heidmann (BGC)* and *Heidmann (Holmberg)* refer to two different catalogs used by Heidmann et al. (1972)
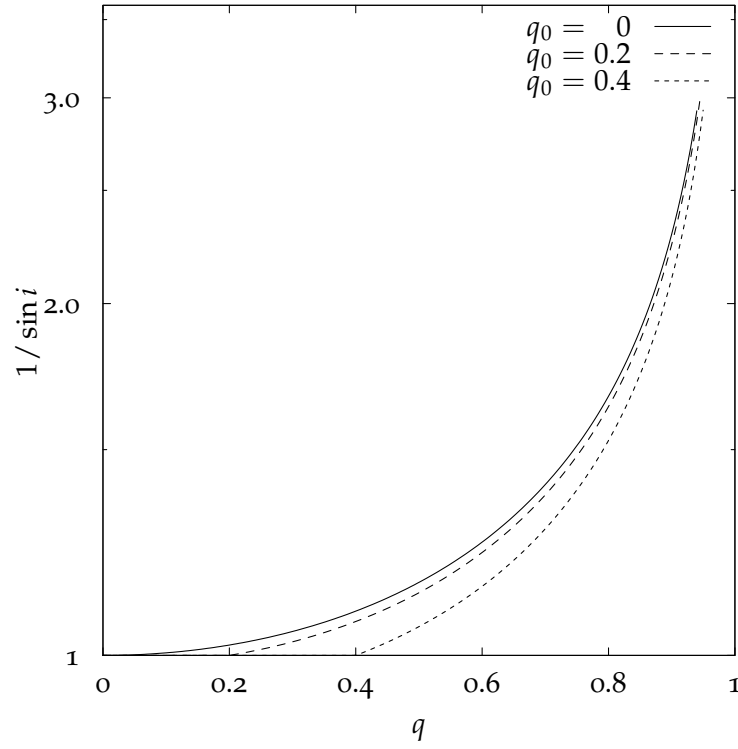
Figure 1.8: Values of $1/\sin i$ (using equation 1.13) for three different values of q_0. Inclination is assumed to be 90° if $q \leq q_0$. Since inclinations closer to face-on are not very useful in the TF relation, the plot shows only the values of $1/\sin i$ that are smaller than 3. The y-axis is logarithmic in the above plot.

1.7.2 *Turbulent motion correction*

In a galaxy, the hydrogen gas has random motions in addition to the circular motions. While the maximum rotation velocity in galaxies for which the TF relation generally applies ranges from $\sim 40 \, \mathrm{km \, s^{-1}} - 300 \, \mathrm{km \, s^{-1}}$, the random motions are $10 \, \mathrm{km \, s^{-1}}$ (see Kamphuis & Sancisi 1993 for example). The effect of these random motions is to widen the observed line profile.

If the line-of-sight random motions (turbulent velocities) are σ_0 across the galaxy, then the line-profile widening is given by a convolution of the circular-speed line profile with by a Gaussian of standard deviation (or dispersion) σ_0. The Gaussian function $f(x)$ with standard deviation σ_0 is:

$$f(x) = \frac{1}{\sqrt{2\pi}\sigma_0} e^{-\frac{x-\mu}{2\sigma_0^2}}, \tag{1.18}$$

where μ is the mean. The width of the Gaussian of standard deviation σ_0 at a level l percent of its peak is given by:

$$W_{t,l} = 2\sigma_0 \sqrt{2\ln\left(\frac{100}{l}\right)}$$
$$= 2\sigma_0 k(l). \tag{1.19}$$

As mentioned in section 1.5, the TF relation is a strictly empirical one, and the corrected line widths may or may not represent the

maximum (v_{max}) or the flat (v_{flat}) portion of the rotation curves of galaxies. Assuming that the H$\textsc{i}$ line-profile width is used as an indicator of the maximum rotation velocity of the galaxy, we need to correct the observed H$\textsc{i}$ line widths for the random motions in the gas. The observed line width can then be written as:

$$W_{l,\mathrm{observed}} = 2v_{\mathrm{max}} \sin i + W_{t,l}. \tag{1.20}$$

(Unless otherwise stated, $W_{l,\mathrm{observed}}$ is abbreviated as W_l in this document.) BGPV assumed that the turbulent motions in the gas are isotropic in the plane of the galaxy disk, and the ratio of the turbulent motions in and normal to the plane of the galaxy disk are given by a constant s. Specifically, if $\sigma_x = \sigma_y$ is the dispersion in the random motions in the galaxy plane, then $\sigma_z = \sigma_x/s$, and $s \geq 1$ (see Figure 1.9, adapted from BGPV).

The equation of the ellipse in the x-z plane is:

$$\frac{z^2}{\sigma_z^2} + \frac{x^2}{\sigma_x^2} = 1, \tag{1.21}$$
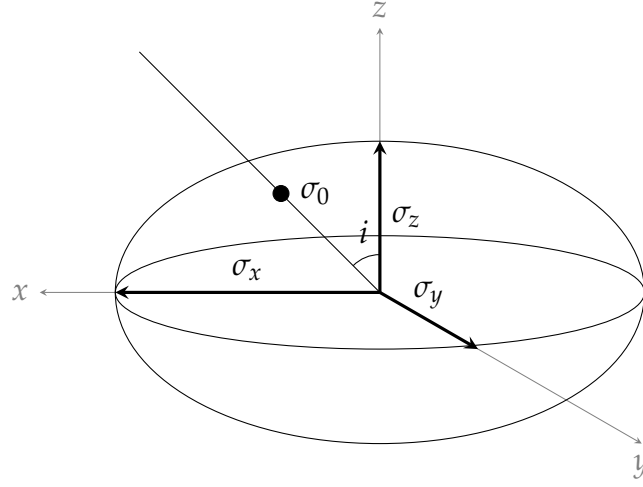
Figure 1.9: Velocity ellipsoid for a galaxy. In this case, $\sigma_x = \sigma_y = s\sigma_z$, and $s \geq 1$. σ_0 is the line-of-sight turbulent velocity.

where $z = \sigma_0 \cos i$, and $x = \sigma_0 \sin i$. Making the above substitutions in equation 1.21 above, we get:

$$\frac{\sigma_0^2}{\sigma_z^2} \left(\frac{\sin^2 i}{s^2} + \cos^2 i \right) = 1$$

$$\Rightarrow \sigma_0 = \sigma_z \frac{s}{\sqrt{s^2 - (s^2 - 1) \sin^2 i}} \qquad (1.22)$$

$$= \sigma_z f(s) \, .$$

By analogy with the then known kinematic properties of the flattest components in our Galaxy (Hɪ, Hɪɪ, ᴏʙ stars), ʙɢᴘᴠ used $s = 1.5$, although in recent work, it has been customary to assume $s = 1$, which means that the random motions are isotropic in all the dimensions (see for example de Vaucouleurs et al. 1983, van der Kruit & Shostak 1982). For $s = 1$, $\sigma_0 = \sigma_x = \sigma_y = \sigma_z$.

BGPV found that the turbulent motion corrections needed were more than if they assumed Gaussian peculiar velocities. In particular, assuming a Gaussian gives $k(20) = 1.80$ (equation 1.19), but they found that using $k(20) = 1.89$ resulted in a lower scatter in the TF relation in their sample. Similarly, $k(50) = 1.18$, but they found that $k(50) = 0.71$ resulted in a better TF relation for line widths at 50% of the peak.

BGPV assumed that the increase in the line width due to the line-of-sight turbulent motions is equal to the width at the level of measurement of a Gaussian with dispersion σ_0. In general, this will be true only if the line profile shape is two delta functions (two sharp peaks with no or little flux at velocities immediately surrounding the peaks). If this is not the case, a more analytical method of correction is needed.

Tully & Fouqué (1985) (TFq hereafter) assumed that a linear subtraction should work for galaxies with large line widths, but a quadrature subtraction is needed for galaxies with smaller line widths. They proposed a formula to correct for the turbulent motions, which degenerates to linear subtraction in the case of large line widths, but performs quadrature subtraction for smaller widths (see Figure 1.10):

$$W_{R,l}^2 = W_l^2 + W_{t,l}^2 - 2W_l\,W_{t,l}\left(1 - e^{-\left(\frac{W_l}{W_{c,l}}\right)^2}\right) - 2W_{t,l}^2\,e^{-\left(\frac{W_l}{W_{c,l}}\right)^2},$$

$$(1.23)$$

where $W_{R,l}$ is the line width after correction for turbulent motions at level l; $W_{t,l}$ is the increase in line width at level l due to random motions (equation 1.19); and $W_{c,l}$ is a parameter that defines the transition region from linear to quadrature subtraction. The generally assumed values of $W_{c,l}$ are $W_{c,20} = 120\,\mathrm{km\,s^{-1}}$ and $W_{c,50} = 100\,\mathrm{km\,s^{-1}}$. TFq also found deviations from Gaussian in turbulent motion correction, and suggested $k(20) = 1.96$. They assumed isotropic turbulent motion ($s = 1$), and $\sigma_0 = 12\,\mathrm{km\,s^{-1}}$.
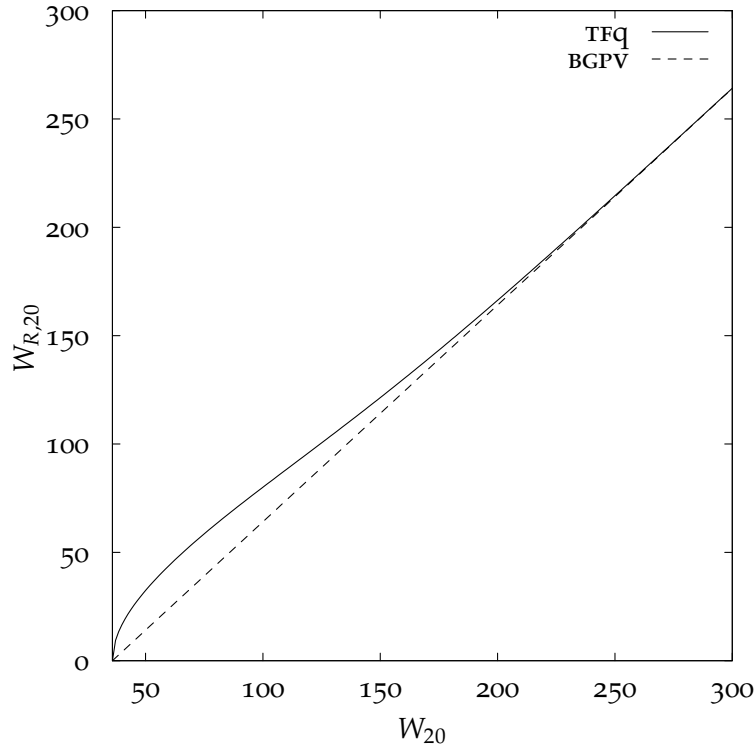
Figure 1.10: The turbulence-corrected line width as a function of observed line width, for linear and quadrature subtractions. The quadrature subtraction is less when the observed line width is small.

Broeils (1992) tried a similar method. He did not decouple σ_0 and $k(l)$. He also realized that v_{max} may be greater than v_{flat}, the velocity at the flat portion of a rotation curve. He then determined the corrections needed by empirically finding $W_{t,l}$ for which the corrected (turbulence and inclination) line width was equal to v_{max} or v_{flat}. The results from his method had a large scatter, so he rejected them.

VSR used HI data from the Ursa Major Cluster of Galaxies, and did the turbulent motion correction in two steps. First, they corrected for line broadening due to instrumental resolution (see section 1.7.3). After applying that correction, they determined the correction due to turbulent motion in a method similar to Broeils (1992), but with their higher signal-to-noise ratio (SNR) data. After applying their formulation for instrumental resolution correction, which is different from the one applied by Bottinelli et al. (1990) (see the next section), they found that:

$$
\begin{aligned}
W_{t,20} &= 22 \, \text{km s}^{-1}, \\
W_{t,50} &= 2 \, \text{km s}^{-1},
\end{aligned}
\tag{1.24}
$$

where $W_{t,l}$, when used in equation 1.23 gives $W_{R,l}$, which is twice the the maximum part of the rotation curve v_{max}. As in Broeils (1992), VSR also considered v_{max} and v_{flat} in their determination of turbulence correction. They also found that it is extremely difficult

and unreliable to retrieve the v_{flat} in a mixed sample of galaxies, but determination of v_{max} is easier. For more details, see VSR.

Springob et al. (2005) did not measure the line width at a given percentage of the peak. After identifying the peak flux level f_p for each horn of the line profile, they fit a polynomial between the levels of 15% and $f_p - rms$, where rms is the root-mean-square noise per channel in the observed line profile. The fitted polynomial is different for each edge of the line profile. If V_l is the velocity at the rising edge where the corresponding polynomial has a flux of 50% of $f_p - rms$, and similarly, V_u for the falling edge, they defined the line width, W_{F50} as the $V_u - V_l$. They also defined other line widths: W_{M50} is the width measured at 50% of the mean flux density, W_{P50} is the width measured at 50% of $f_p - rms$, W_{P20} is the width at 20% of $f_p - rms$, and W_{2P50} is the width at 50% of each of the two peaks minus the rms value.

1.7.3   Instrumental resolution correction

Because of a finite resolution (in velocity/frequency) of the observing instrument, the line profile is further broadened. If the resolution of the observing instrument (a single-dish telescope, for example)

is R (FWHM), then the broadening can be approximated by a convolution with a Gaussian with dispersion σ_R given by:

$$\sigma_R = \frac{R}{\sqrt{8\ln 2}} \tag{1.25}$$

Since the convolution of two Gaussians is another Gaussian, the combined effect of turbulent motions and finite instrumental resolution is to broaden the line profile by convolving it with a Gaussian of dispersion σ_c, where:

$$\sigma_c = \sqrt{\sigma_0^2 + \sigma_R^2}, \tag{1.26}$$

where σ_R is defined above in equation 1.25.

The most common and widely used method of determining and correcting for instrumental broadening is given by Bottinelli et al. (1990). Based upon H I data of many galaxies, they found that:

$$W_{l,R=0} = W_{l',R} + (0.014l' - 0.83)R - 0.56(l - l'), \tag{1.27}$$

where l and l' are the two different levels at which line-profile widths are measured. If $l = l'$, then the above equation takes a simpler form, and the equations for $l = 20$ and $l = 50$ are:

$$W_{20,R=0} = W_{20,R} - 0.55R$$
$$W_{50,R=0} = W_{50,R} - 0.13R. \tag{1.28}$$

The widths above are not corrected for turbulent motions in the galaxy.

Following vsr, the observed line width at 20% of the peak is broadened from the case of zero turbulence and zero instrumental resolution by (see equation 1.19):

$$
\begin{aligned}
\Delta W_{20} &= \sigma_c \sqrt{8\ln 5} \\
&= \sqrt{\sigma_0^2 + \sigma_R^2}\,\sqrt{8\ln 5}.
\end{aligned}
\tag{1.29}
$$

Then, the broadening just due to the finite instrumental resolution is given by:

$$
\begin{aligned}
\delta W_{20} &= \Delta W_{20} - \sigma_0 \sqrt{8\ln 5} \\
&= \sigma_0 \sqrt{8\ln 5}\left[\sqrt{1 + \frac{(R/\sigma_0)^2}{8\ln 2}} - 1\right] \\
&= 3.59\sigma_0\left[\sqrt{1 + \frac{(R/\sigma_0)^2}{5.55}} - 1\right].
\end{aligned}
\tag{1.30}
$$

1.8 OUTLINE OF THE THESIS

Based upon the previous discussion, it can be seen that many different factors affect the calibration and application of the tf relation, and some of those factors could be inter-dependent. For example, higher

values of inclinations lead to smaller corrections in the observed line widths (equation 1.12). Similarly, the turbulent motion correction is higher if one over-estimates the line-of-sight turbulent motion in a galaxy (1.20).

The aim of this thesis is to understand kinematics of disk galaxies, and in particular the various factors that go into the Tully-Fisher relationship. In order to do that, I have developed a detailed 3-dimensional kinematic model of HI in disk galaxies.

Chapter 2 describes the physical model in detail. It also describes the implementation of the model, including algorithms used in the implementation.

In chapter 3, I discuss the results from the model. I also compare the output of the model for a sample of galaxies. I discuss the differences in the output and the observations. I also study the effect of varying various parameters on the output from the model.

In chapter 4, I discuss few of the general results from the model. In particular, I discuss various methods of turbulent motion and inclination correction and their effects on the corrected line profile widths.

Finally, in chapter 5, I summarize the results and discuss future directions.

2

MODELING H I IN GALAXIES

> Beware of bugs in the above code; I have only proved it correct, not tried it.
>
> Donald Knuth

> Debugging is twice as hard as writing the code in the first place. Therefore, if you write the code as cleverly as possible, you are, by definition, not smart enough to debug it.
>
> Brian W. Kernighan

I have created a model of neutral hydrogen (H I) in disk galaxies in order to study the connection between galaxy kinematic properties and the measured H I line width. The model is written in the programming language Python. In this chapter, a detailed description of the model is presented.

2.1 MOTIVATION

The motivation for the model comes from many of the factors mentioned in chapter 1.

In particular, the empirical assumptions used in line width corrections need to be tested to see if they make physical sense. For example, the broadening of line profiles as defined by equations 1.20 and 1.30 both assume that the effect of turbulent motions and finite instrumental resolution of the observing telescope is to widen the line profiles by an amount that is equal to the width of an appropriate Gaussian at the level of the measurement of the line profile. As mentioned in section 1.7.2, mathematically, this works only if the H$\textsc{i}$ line profiles are two delta functions. Since this is not the case for real galaxies, it is important to test if the corrections for these effects are correct.

Galaxies, even of the same type, have different rotation curve shapes. The effect of rotation curve shapes on the H$\textsc{i}$ line profiles and the TF relation needs to be understood more clearly.

There may or may not be a direct connection between W_l and v_{max} or v_{flat}. It is important to determine if such a connection is real, giving us a stronger physical basis for the TF relation, or if the TF relation works even without this connection. The original relation, as proposed by Tully & Fisher (1977), is empirical.

If the rotation curves and surface H$\textsc{i}$ density distributions derived from the Very Large Array (VLA), Westerbork Synthesis Radio Telescope (WSRT), or any other interferometric telescope are used in a kinematic model, then the kinematic model should reproduce reproduce the observed H$\textsc{i}$ and velocity field. This not only verifies the

accuracy of the kinematic model, but also is a check on the observed data and their analysis.

Once the model is tested for a few galaxies, it can be used to do a study of HI line profile parameters.

The maximum rotation speed of a galaxy contributes the most to its HI line profile width. The other effects that widen the line profile are random motions, the velocity resolution of the observing telescope, and presence of other factors such as high-velocity clouds in the galaxy. The actual rotation curve shape, the surface density distribution, and the distribution of random motions define the shape of the line profile. In addition, for galaxies that are not completely edge-on, the line profile is narrowed by a factor $\sin i$, where i is the inclination of the galaxy disk.

In general, these parameters (circular speed, $v_c(r)$, surface density, $\rho(r)$, and random motions, $\sigma_0(r)$) are not azimuthally symmetric in a galaxy disk. In cylindrical coordinates, it is more correct to have the above depend not only on r, but also on the azimuthal angle, θ. In practice, $v_c(r)$ and $\rho(r)$ are derived from radio observations, such as from the VLA and the WSRT, and usually they are calculated for two sides of the galaxy, the approaching side and the receding side. For example, AIPS task `gal` can be used to fit tilted-ring models to the approaching and receding sides of a galaxy at different radii, and return the rotation curve for the two sides separately. The random motions are usually assumed to be isotropic.

Another factor that influences the line profile shape is the z-dependency of velocity and density, where z is the axis perpendicular to the galaxy disk. The density in z is usually taken to be exponential, with a characteristic z as the *scale height*.

2.2 THE MODEL

The model itself consists of a 3-dimensional distribution of v_c, ρ, σ_0, and other galaxy properties such as inclination, scale height, galaxy distance, etc. (see below). Using these parameters, it is possible to create H$\textsc{i}$ line profiles, maps of neutral hydrogen intensity as seen on the sky, channel maps (to compare them with the channel maps from the radio telescopes), and position-velocity diagrams for a galaxy.

As a test, the above parameters come from the observations of H$\textsc{i}$ in galaxies, and the properties derived from the model are compared with the observed properties for those galaxies.

A galaxy in the model consists of three-dimensional cells, in the x, y, and z dimensions. The total number of cells of H$\textsc{i}$ in a galaxy is $n_x \times n_y \times n_z$, where n_i is the number of cells in the ith dimension. The number of cells in a typical model is $\approx 10^6$ ($n_x = n_y = 10^3$).

A galaxy has certain global properties:

- distance, d in Mpc

- inclination angle, i in degrees ($0°$ is face-on)

- surface density distribution, in $M_\odot/pc^2$

- circular velocity distribution, in km s^{-1}

- scale height of the disk, z_{max} in pc

- heliocentric velocity, v_{hel} in km s^{-1}; positive if receding

- semi-major axis, a in pc

- position angle of the major axis on the sky in degrees

- its position in the sky (R.A. and declination)

The last three parameters – the galaxy semi-major axis, the galaxy position angle and the galaxy position – are not necessary for the model, but they are known, and they allow direct comparison of the modeled data with the observations.

In addition to the above properties, a galaxy has other parameters associated with it, which describe the parameters for a particular (single-dish and/or array of telescopes such as the VLA and the WSRT) observation of the galaxy. We will talk about these parameters in detail later.

2.2.1 *Coordinate system*

For an edge-on ($i = 90°$) galaxy, the x-axis points toward the observer. The y-axis points to the right, as seen by the observer, looking toward the galaxy. The z-axis completes a right-hand coordinate system (thus,

the z-axis points along the vector normal to the plane of the galaxy, centered at the galaxy).

This coordinate system is attached to the galaxy. Therefore, in a galaxy inclined at an angle i, the coordinate system is rotated counter-clockwise about the y-axis (as seen from $+y$-axis). In addition, a galaxy can be rotated in its plane (about the z axis). This rotation angle is denoted as ψ, which is positive if the rotation is counter-clockwise about the z-axis, as seen from $+z$-axis (Figure 2.1). ψ is usually $0°$, but it can be useful to test the effect of nonzero ψ on the observed galaxy properties, such as line profiles in the absence of axial symmetry.

As described at the beginning of this section, the rotation curves and the surface density profiles for galaxies are usually published for the approaching and receding sides separately. These are az-imuthal averages of the velocity and surface density values for the approaching and receding sides respectively. By rotating the galaxy in the x-z plane, it is possible to see the differences introduced by such a rotation on the line profile shape, and line widths. This is done in chapter 4.

Line-of-sight velocity is positive for the receding parts in the galaxy, and negative for the approaching parts.
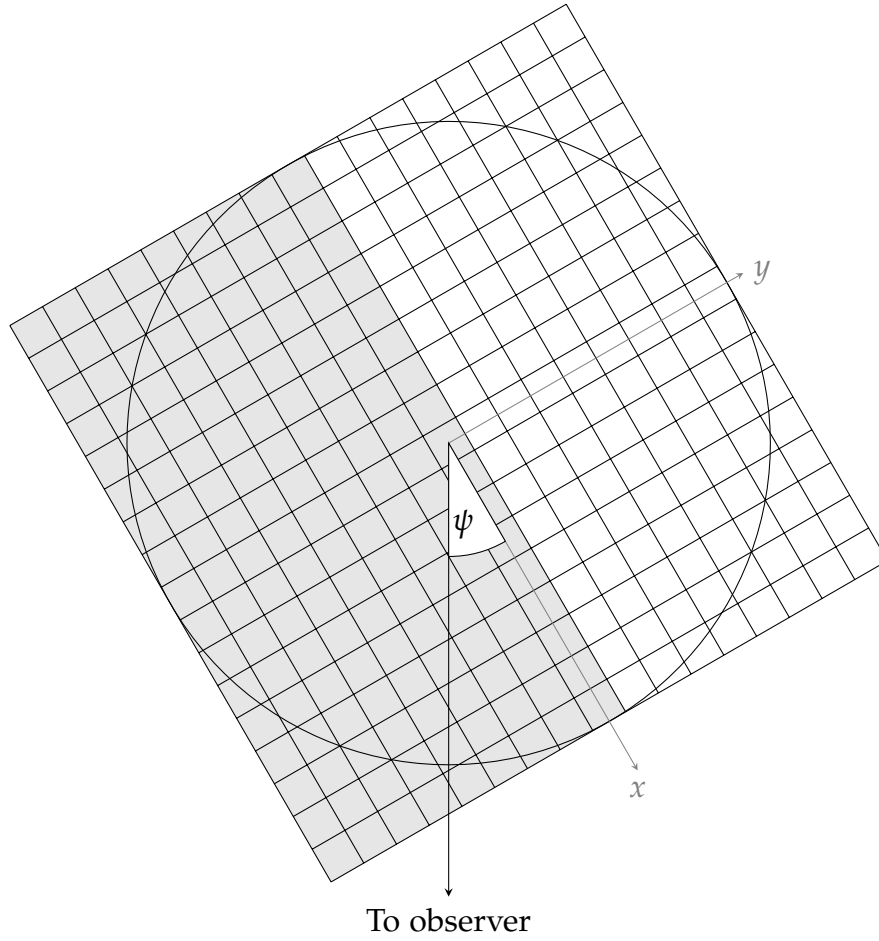
Figure 2.1: Partitioning a galaxy into cells, as seen from the 'top'. The cells marked □ get their density and circular speeds from the 'approaching' part of the surface density profiles and rotation curves, while and the cells marked as □ get their values from the 'receding' part of the data. Note that the filled and the unfilled cells are approaching and receding respectively only if $\psi = 0°$. In the above figure, $n_x = n_y = 17$, $i = 90°$ and $\psi = 30°$.

2.2.2 *Cells in a galaxy*

The number of cells in each dimension (n_i, as described above) is an odd number. This insures that the central cell in the galaxy is exactly centered at the origin of the coordinate system defined above (see Figure 2.1).

Each cell has certain properties associated with it:

- the surface density at the center of the cell, in $M_\odot/pc^2$, which is the cumulative density at the cells looking directly down the z-axis. The sum of densities of all the cells along a given z direction equals the surface density of the galaxy at that point. The model assumes that the galaxy is symmetric about $z = 0$ plane.

- the three dimensional velocity at the center of the cell (v_x, v_y, v_z).

- the three dimensional turbulent velocity (assumed to be a Gaussian distribution) at the center of the cell (σ_x, σ_y, σ_z).

2.2.3 *Creating line profiles*

Each point (cell) in the galaxy generates a line profile that is a Gaussian centered at the line-of-sight velocity at that cell, and with a

dispersion σ_0, which is equal to the line-of-sight turbulent velocity at that cell.

Also, as mentioned in section 1.7.3, the observed line profile for a galaxy is broadened because of finite velocity resolution of the observing telescope. If the instrumental resolution (after any smoothing of the line profile) is R (FWHM), then the effect of that instrumental resolution is as if the actual line profile of the galaxy is convolved with a Gaussian with a dispersion σ_R (see equation 1.25).

Given that the convolution of two Gaussians is another Gaussian, we can calculate the line profile by first assuming that each cell generates a 'line profile' centered at its line-of-sight velocity, and then convolving it with a Gaussian that has dispersion σ_c given by:

$$\sigma_c = \sqrt{\sigma_R^2 + \sigma_0^2}. \qquad (2.1)$$

The area under the line profile from a cell is proportional to the H$\textsc{i}$ mass of that cell (see equation 2.2).

For most disk galaxies, the assumption that the turbulent velocity is independent of position in the galaxy works well. In some cases, the z-axis turbulent velocity is assumed to be different from the x- and y-axis turbulent velocity. Even in those cases, as long as the x-, y-, and z-components of the turbulent velocities are constant across the galaxy, the line-of-sight turbulent velocity will be isotropic (see section 1.7.2).

The line profile from each cell is such that the area under the profile (in Jy km s^{-1}), S, is given by (see equation 1.5:

$$\frac{M_{\text{HI}}}{M_\odot} = 2.356 \times 10^5 d^2 S, \tag{2.2}$$

where d is the galaxy distance in Mpc, M_{HI} is the cell-HI mass, and $M_\odot$ is the mass of the sun ($1.988\,92 \times 10^{30}$ kg).

In cylindrical coordinates, we have the following relations:

$$
\begin{aligned}
r_{\text{cyl}} &= x^2 + y^2, \\
\theta &= \tan^{-1}\left(\frac{y}{x}\right), \\
z &= z,
\end{aligned}
\tag{2.3}
$$

and:

$$
\begin{aligned}
v_x &= -v_c(r)\sin\theta, \\
v_y &= v_c(r)\cos\theta, \\
v_z &= 0.
\end{aligned}
\tag{2.4}
$$

In the above equation v_z represents non-circular, non-planar motions, and is 0, assuming purely circular motions parallel to $z = 0$ plane. In order to calculate the line of sight velocity of a cell, we

first calculate the velocity assuming $i = 90°$. For this, referring to figure 2.2, we see that:

$$
\begin{aligned}
v_{\text{los},i=90°} &= v_c \cos\left(\frac{\pi}{2} - (\psi + \theta)\right) \\
&= v_c \sin(\psi + \theta) \\
&= v_c (\sin\psi \cos\theta + \cos\psi \sin\theta) \\
&= v_y \sin\psi - v_x \cos\psi.
\end{aligned}
\tag{2.5}
$$
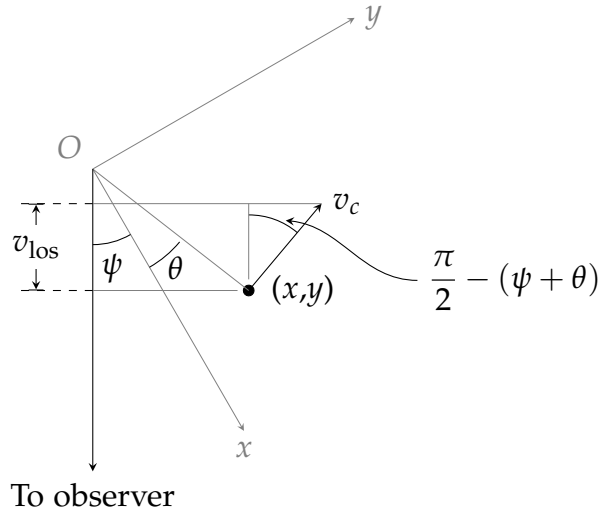
Figure 2.2: Calculating the line-of-sight velocity for a point in the galaxy. The point (x,y) makes an angle $\theta = \tan^{-1}\left(\frac{y}{x}\right)$ with the x-axis. The vector v_c is the circular velocity, which is perpendicular to the radial line from the origin (O) to the point (x,y). ψ is the galaxy rotation angle, and $\psi = 30°$, as in Figure 2.1.

It can be shown that the above formula is valid even when the point (x,y) lies in any of the four quadrants in the x-y plane.

Now, for an inclination $i \neq 90°$, the line-of-sight velocity is:

$$
\begin{aligned}
v_{\text{los}} &= v_{\text{los},i=90°} \sin i + v_z \cos i + v_{\text{hel}} \\
&= \left(v_y \sin \psi - v_x \cos \psi\right) \sin i + v_z \cos i + v_{\text{hel}}.
\end{aligned}
\tag{2.6}
$$

The addition of v_{hel} in equation 2.6 is due to the motion of the galaxy at a speed v_{hel} with respect to the sun (heliocentric velocity).

The line of sight turbulent velocity is given by:

$$
\sigma_0 = \frac{\sigma_x \sigma_z}{\sqrt{\left(\sigma_x \cos i\right)^2 + \left(\sigma_z \sin i\right)^2}}.
\tag{2.7}
$$

2.3 THE SOFTWARE MODEL

For all the calculations involving real numbers, double precision floating point numbers are used. Even with double precision, some calculations may give results that are mathematically invalid. This is a due to the particular format the floating-point numbers are stored in computers, and is different from rounding errors. All effort has been made to minimize such cases. For a discussion of some of the issues with floating-point numbers, see Goldberg (1991), Kahan (2004), Monniaux (2007).

2.3.1 *The galaxy*

The software manifestation of a galaxy is a data structure that holds various galaxy parameters, such as the density and velocity distribution, the distance to the galaxy, etc. The data structure also holds parameters relevant to a particular observation of the galaxy, such as the instrumental resolution of the telescope, the beam size of the telescope, etc. For a complete description of the parameters, see appendix B. In addition to these parameters, the galaxy data structure uses many functions to calculate line profiles, channel maps, position-velocity (p-v) diagrams, etc.

In addition, there are some 'utility functions' that are used to read the galaxy density and velocity data from files, plot the line profiles, etc.

2.3.2 *Rotation curves and density profiles*

The data from H<small>I</small> observations of galaxies can be used to determine their H<small>I</small> rotation curves and surface density profiles. It is usually possible to fit rotation curves separately for the approaching and the receding sides. The model uses these fitted curves to assign density and velocity to each cell in the galaxy. To do this, a few things are done.

First, the distance of each cell (in pc) from the galaxy center is determined. The coordinate system that is the most useful for this kind of analysis is the cylindrical coordinate system. Hence, each cell's position is converted to cylindrical coordinates. After determining the distances, the circular velocity and the density at the cell is determined by linearly interpolating the rotation curve and the density profile. If the rotation curve and/or the surface density profile is available for the approaching and the receding side separately, the appropriate part of the curve is used for interpolation depending upon the y coordinate of the cell.

Second, the maximum radius of the published rotation curves are not necessarily the same as the maximum radius of the published surface density profiles (see section 3.3). In case the two maximal radii are different, the model extrapolates the data with lower maximum radius to match with the higher radius.

After determining each cell's H<small>I</small> density and velocity, the line profile from the cell is created as described in section 2.2.3. Adding the line profiles from all the cells gives the total H<small>I</small> line profile for the galaxy.

3

COMPARING THE MODEL WITH THE OBSERVATIONS

> There is something fascinating about science. One gets such wholesale returns of conjecture out of such a trifling investment of fact.
>
> Mark Twain

In this chapter, I discuss the results obtained from the model and compare them with the observations for 7 galaxies. The aim is to successfully generate line profiles for galaxies with known rotation curves and surface density profiles, and compare them to their observed HI profiles.

I first present the results for a sample of density and velocity distributions to test the model, and compare the results with the expected analytical results. Once the model is verified using the sample distributions, I use it on galaxies from observations, and compare the results from the model with the observed properties. I discuss the differences, if any, in the simulated line profiles and actual line profiles for these galaxies.

The galaxies used for modeling in this chapter cover a wide range of rotation curve types, maximum rotation velocities, and inclinations.

Thus, the galaxies cover a reasonable range of galaxy cases in the TF relation.

3.1 SIMPLE 'GALAXIES'

A few simple density and velocity distributions can be used to make sure that the numerical model produces the same line profiles as predicted analytically. Since, in general, predicting line profile intensities is non-trivial except for really simple distributions, I compare three such distributions and briefly discuss the results.

3.1.1 *Constant circular speed, uniform density*

The simplest case is of an edge-on ($i = 90°$) galaxy with a constant circular velocity in the disk, uniform HI density, and no random motions ($\sigma_0 = 0$). See table 3.1 for details on the parameters for such a galaxy. This galaxy is referred to as *the simple galaxy* in this document.

Figure 3.1 shows a ring at radius r in such a galaxy. Referring to the figure, we have:

$$v = v_c \sin \theta$$
$$\Rightarrow \theta = \sin^{-1} \left(\frac{v}{v_c} \right).$$

(3.1)

Parameter	Symbol	Value
Distance	d	10 Mpc
Inclination	i	90°
Surface density	ρ	1 M$_\odot$/pc²
Circular speed	v_c	100 km s^{-1}
Radius	R	2×10^4 pc

Table 3.1: The parameters used in modeling a constant circular speed, uniform density galaxy.
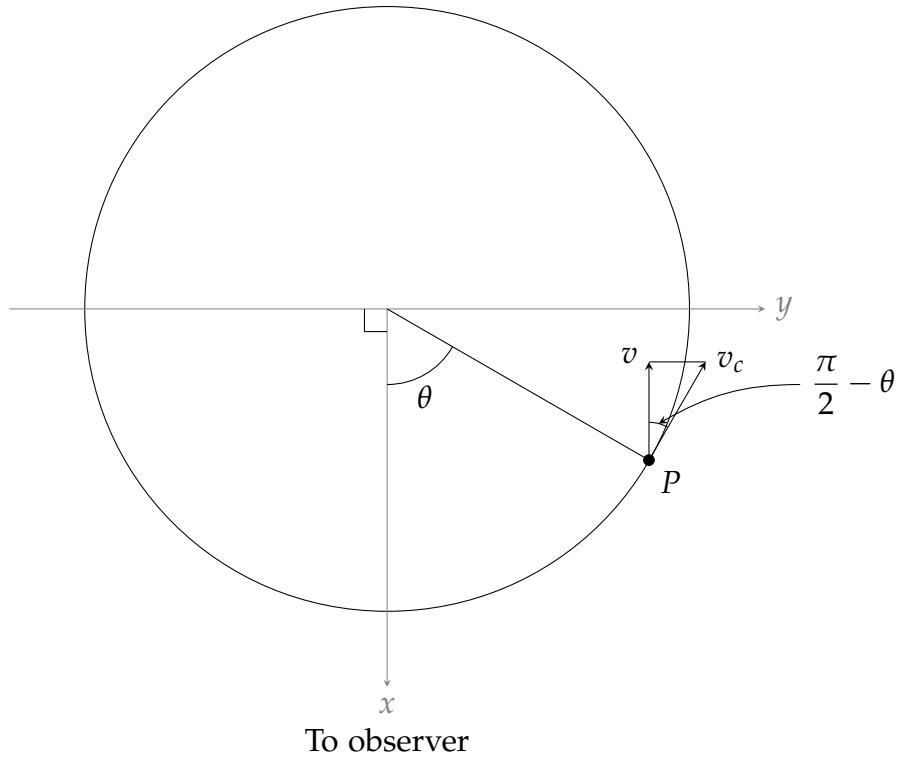
Figure 3.1: A constant circular-speed galaxy, with uniform H I density. Only a ring of H I at a radius r is shown.

If we denote the line of sight velocity by v_{los}, then the observed velocity distribution function, $f(v)$ is found by differentiating the cumulative velocity distribution function, $F(v_{\text{los}} \leq v; v_c)$, where

$$F\left(v_{\text{los}} \leq v; v_c\right) = \frac{\pi/2 + \theta}{\pi}. \tag{3.2}$$

The cumulative velocity distribution, $F(v_{\text{los}} \leq v; v_c)$ is the probability of observing a line of sight velocity that is less than or equal to v, given that the (constant) circular speed of the galaxy is v_c.

Thus,

$$\begin{aligned}
f(v) &= \frac{\mathrm{d}}{\mathrm{d}\,v} F\left(v_{\text{los}} \leq v; v_c\right) \\
&= \frac{\mathrm{d}}{\mathrm{d}\,v} \frac{\theta}{\pi} \\
&= \frac{1}{\pi} \frac{\mathrm{d}}{\mathrm{d}\,v} \sin^{-1}\left(\frac{v}{v_c}\right) \\
&= \frac{1}{\pi v_c \sqrt{1 - \left(\dfrac{v}{v_c}\right)^2}}.
\end{aligned} \tag{3.3}$$

If the surface density, in $M_{\odot}/\text{pc}^2$ of the galaxy is ρ and the disk has a radius of R (pc), the mass of the galaxy is $M = \rho \pi R^2 M_{\odot}$. Then, using equation 2.2, the integrated H$\textsc{i}$ flux of the galaxy is:

$$S = \frac{\rho \pi R^2}{2.356 \times 10^5 d^2} \qquad \text{Jy km s}^{-1}. \tag{3.4}$$

From equations 3.3 and 3.4, we have the flux as a function of the observed velocity:

$$S(v) = S \times f(v)$$

$$= \frac{\rho R^2}{2.356 \times 10^5 d^2 v_c \sqrt{1 - \left(\frac{v}{v_c}\right)^2}} \quad \text{Jy.} \qquad (3.5)$$

Substituting the values of ρ, R, d, and v_c from table 3.1, we get:

$$S(v) = \frac{0.170}{\sqrt{1 - \left(\frac{v}{100}\right)^2}}. \qquad (3.6)$$

Figure 3.2 shows the numerical line profile from the model and the analytic line profile from equation 3.6. As expected, the calculated flux at line-of-sight velocities whose magnitude is greater than $100 \, \text{km s}^{-1}$ is zero, because there is no point on the galaxy surface with these (line-of-sight) velocities.

3.1.2 *Solid body rotation*

The galaxy has a uniform surface density, and has a rotation speed that is linearly proportional to the radial distance from the center:

$$v_c(r) = \omega r \qquad (3.7)$$
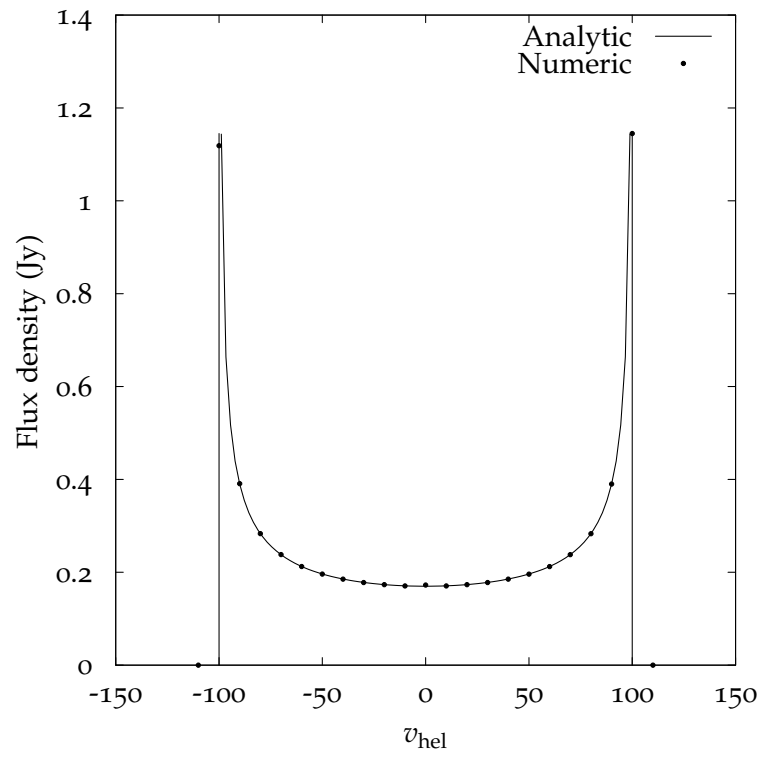
Figure 3.2: Simulated (points) and theoretical (line) line profiles for a galaxy with constant circular speed.

Parameter	Symbol	Value
Distance	d	$10\,\mathrm{Mpc}$
Inclination	i	$90°$
Surface density	ρ	$1\,\mathrm{M_\odot/pc^2}$
Circular speed	$v_c(r)$	$\omega r\,\mathrm{km\ s^{-1}}$
Angular velocity	ω	$5 \times 10^{-3}\,\mathrm{rad\ s^{-1}}$
Semi-major axis	R	$2 \times 10^4\,\mathrm{pc}$

**Table 3.2:** The parameters used in modeling a solid-body rotation curve galaxy.

The test galaxy is almost the same as the constant circular speed galaxy, but with $v_c(0) = 0\,\mathrm{km\ s^{-1}}$ and $v_c(R) = 100\,\mathrm{km\ s^{-1}}$ (see table 3.2).

Figure 3.3 shows an infinitesimally thin ring of thickness $\mathrm{d}r$ at a radius r for such a galaxy.

For the ring in the figure, the reasoning of section 3.1.1 applies, but with the difference that the area of the galaxy is replaced by the area of the ring, and the result is integrated for all r. Thus, equation 3.4 now becomes:

$$\mathrm{d}S = \frac{\rho \times 2\pi r}{2.356 \times 10^5 d^2}\,\mathrm{d}r \qquad \mathrm{Jy\ km\ s^{-1}}. \tag{3.8}$$
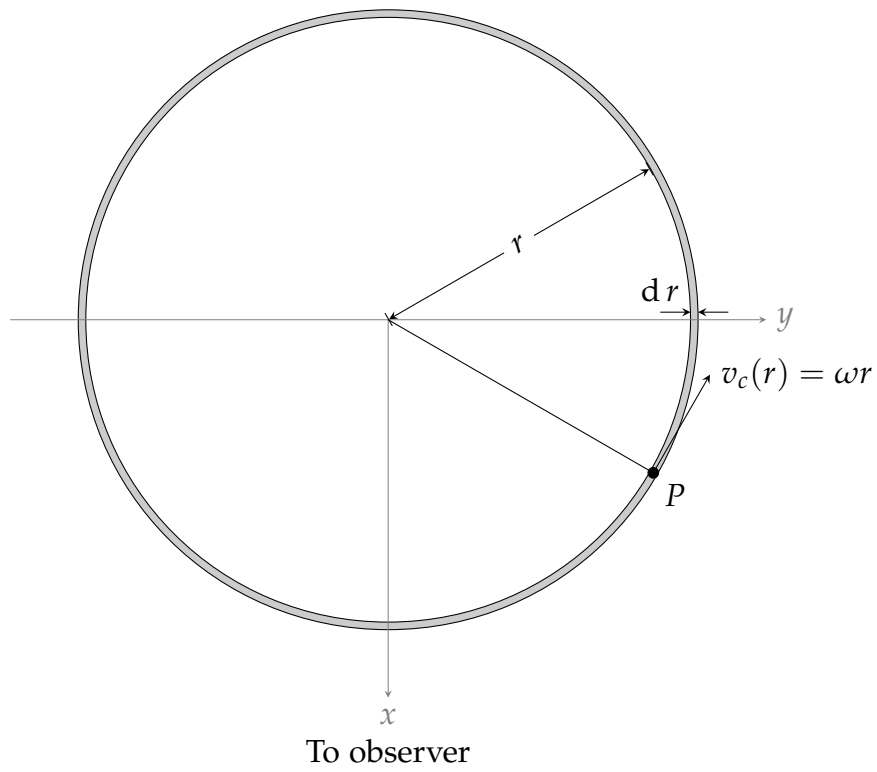
Figure 3.3: A solid-body rotation curve galaxy, with uniform Hɪ density. A ring at radius r, with thickness $\mathrm{d}\,r$ is shown. The rest of the details are the same as in Figure 3.1.

Therefore, we have:

$$
\mathrm{d}\,S(v) = \mathrm{d}\,S \times f(v)
$$

$$
= \frac{2\rho r}{2.356 \times 10^5 d^2 v_c\,(r)\,\sqrt{1 - \left(\dfrac{v}{v_c\,(r)}\right)^2}}\,\mathrm{d}\,r \tag{3.9}
$$

$$
= \frac{\alpha}{\sqrt{1 - \left(\dfrac{v}{v_c\,(r)}\right)^2}}\,\mathrm{d}\,r \quad \text{Jy,}
$$

where,

$$
\alpha = \frac{2\rho}{2.356 \times 10^5 d^2 \omega}. \tag{3.10}
$$

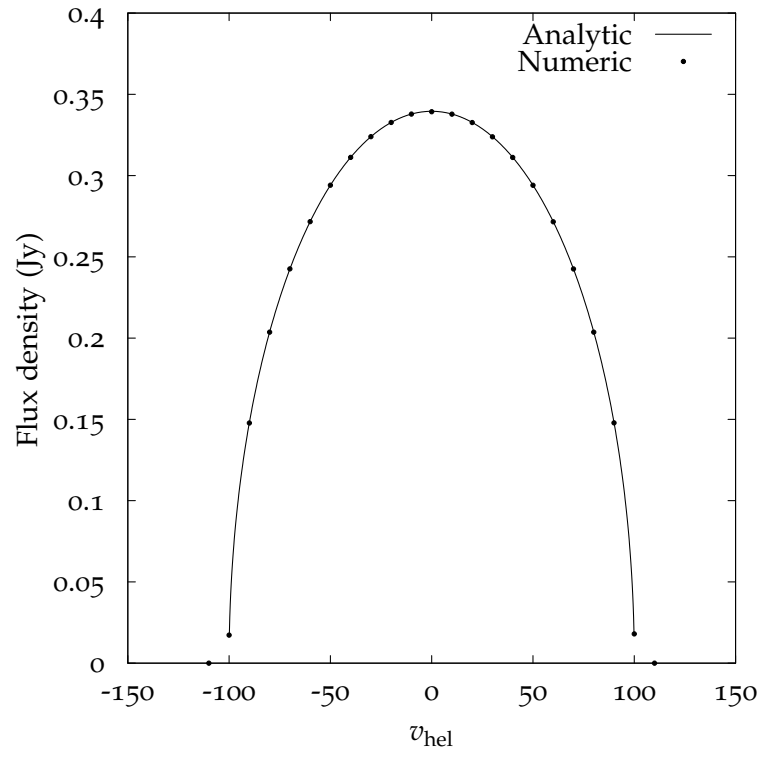The above equations are valid only for $|v| \leq v_c(r)$, or equivalently, $r \geq |v|/\omega$.

We can now calculate $S(v)$:

$$
S(v) = \int_{\frac{|v|}{\omega}}^{R} \frac{\alpha}{\sqrt{1 - \left(\dfrac{v}{\omega r}\right)^2}}\,\mathrm{d}\,r \tag{3.11}
$$

$$
= \alpha R \sqrt{1 - \left(\frac{v}{\omega R}\right)^2} \quad \text{Jy.}
$$

Substituting the values from table 3.2 into equations 3.10 and 3.11, we get:

$$
S(v) = 0.340 \sqrt{1 - \left(\frac{v}{100}\right)^2} \quad \text{Jy.} \tag{3.12}
$$

Figure 3.4 shows the simulated line profile for the galaxy described in table 3.2, as well as the profile described by the equation 3.12.

Figure 3.4: Numeric (points) and analytic (line) line profiles for a galaxy with a solid-body rotation curve as specified in table 3.2.

Parameter	Symbol	Value
Distance	d	$10\,\mathrm{Mpc}$
Inclination	i	$90°$
Surface density	ρ	$a - br$
	a	$1\,\mathrm{M_\odot/pc^2}$
	b	$5 \times 10^{-5}\,\mathrm{M_\odot\,pc^{-3}}$
Circular speed	$v_c(r)$	cR for $r \leq R_1$,
		$100\,\mathrm{km\,s^{-1}}$ otherwise
	c	$0.02\,\mathrm{km\,pc^{-1}\,s^{-1}}$
	R_1	$5 \times 10^3\,\mathrm{pc}$
Semi-major axis	R	$2 \times 10^4\,\mathrm{pc}$

Table 3.3: The parameters used in modeling a rising+flat rotation curve, linear density galaxy. The values a and b are chosen such that $\rho(0) = 1\,\mathrm{M_\odot/pc^2}$, and $\rho(R) = 0$.

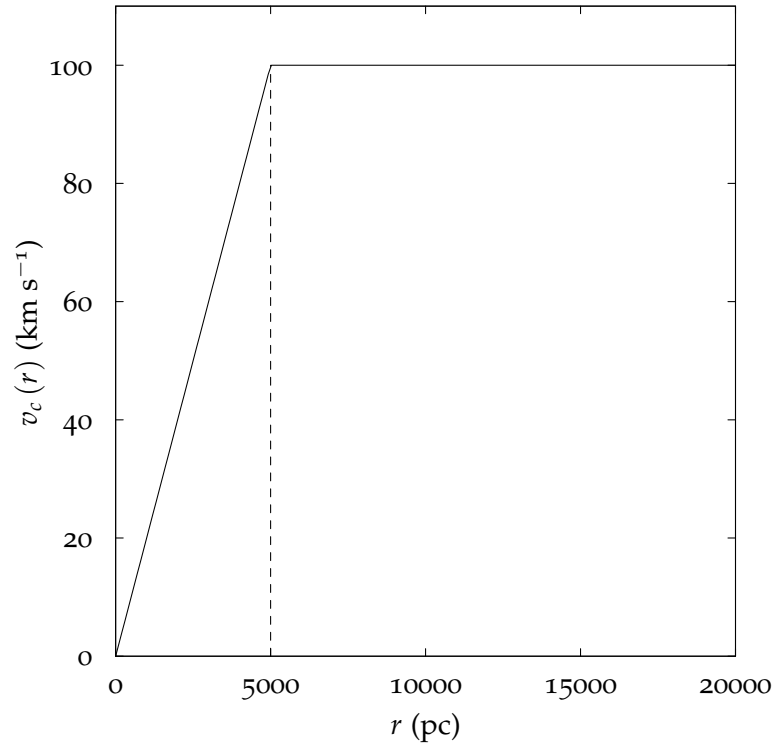### 3.1.3 *Rising+flat rotation curve, linear density fall-off*

In the final 'simple' galaxy, $\rho(r)$ linearly falls as the radial distance, and the rotation curve linearly rises in the inner part before flattening out for large radii. Mathematically,

$$\rho(r) = a - br, \tag{3.13}$$

and,

$$v_c(r) = \begin{cases} cr & \text{for } 0 \leq r \leq R_1, \\ cR_1 & \text{for } R_1 < r \leq R, \end{cases} \tag{3.14}$$

where a, b, c, and R_1 are constants. The simulated galaxy has the values chosen such that $\rho(R) = 0$ (so, $a = bR$; see table 3.3).

Figure 3.5: Rotation curve for a galaxy with linearly rising and flat rotation
curve, and linearly falling surface density.

The rotation curve and the density distribution for the simulated
galaxy are shown in figures 3.5 and 3.6.
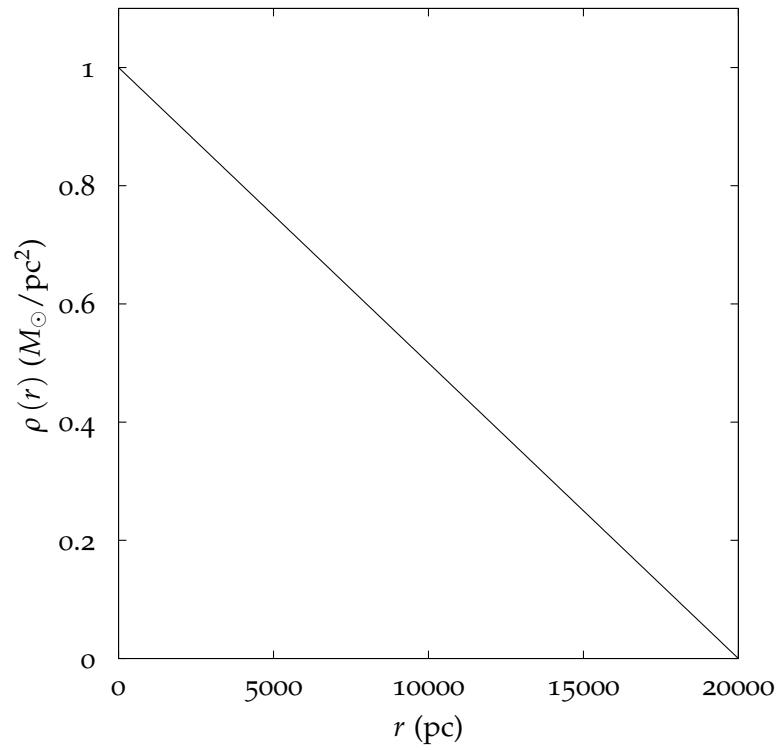
Figure 3.6: Surface density distribution for a galaxy with linearly rising and flat rotation curve, and linearly falling surface density.

For this case, $f(v)$ is given by equation 3.3, and $\mathrm{d}\,S$ is given by equation 3.8. Substituting equation 3.13 in the first expression of equation 3.9, we get:

$$\mathrm{d}\,S(v) = \frac{(a-br)\times 2\pi r}{2.356\times 10^5 d^2} \times \frac{1}{\pi v_c\,(r)\,\sqrt{1-\left(\dfrac{v}{v_c\,(r)}\right)^2}}\,\mathrm{d}\,r$$

$$= \frac{2\,(a-br)\,r}{2.356\times 10^5 d^2 v_c\,(r)\,\sqrt{1-\left(\dfrac{v}{v_c\,(r)}\right)^2}}\,\mathrm{d}\,r \qquad (3.15)$$

$$= \beta\frac{(a-br)\,r}{v_c\,(r)\,\sqrt{1-\left(\dfrac{v}{v_c\,(r)}\right)^2}},$$

where

$$\beta = \frac{2}{2.356\times 10^5 d^2}. \qquad (3.16)$$

To get the equation for the line profile in this case, integrating equation 3.15 gives:

$$S(v) = \beta\int_{\frac{|v|}{c}}^{R_1} \frac{(a-br)}{c\sqrt{1-\left(\dfrac{v}{cr}\right)^2}}\,\mathrm{d}\,r + \frac{\beta}{cR_1\sqrt{1-\left(\dfrac{v}{cR_1}\right)^2}}\int_{R_1}^{R}(a-br)\,r\,\mathrm{d}\,r.$$

$$(3.17)$$

Solving the integral in equation 3.17 gives:

$$S(v) = \frac{\beta a R_1}{c}\sqrt{1 - \left(\frac{v}{cR_1}\right)^2} -$$

$$8\beta bc\left[c^2 R_1^2\sqrt{1 - \left(\frac{v}{cR_1}\right)^2} - v^2\log\left(\frac{|v|}{cR_1\left(1 + \sqrt{1 - \left(\frac{v}{cR_1}\right)^2}\right)}\right)\right] +$$

$$\frac{\beta}{cR_1\sqrt{1 - \left(\frac{v}{cR_1}\right)^2}}\left[\left(\frac{aR^2}{2} - \frac{bR^3}{3}\right) - \left(\frac{aR_1^2}{2} - \frac{bR_1^3}{3}\right)\right]. \quad (3.18)$$

Finally, substituting the values of the constants in equation 3.18 from table 3.3, we get:

$$S(v) = 0.019\sqrt{1 - \left(\frac{v}{100}\right)^2} -$$

$$2.65 \times 10^{-7}v^2\log\left(\frac{100 \times \left(1 + \sqrt{1 - \left(\frac{v}{100}\right)^2}\right)}{|v|}\right) +$$

$$\frac{0.048}{\sqrt{1 - \left(\frac{v}{100}\right)^2}}. \quad (3.19)$$

Figure 3.7 shows the theoretical and simulated line profiles for a galaxy described in table 3.3.
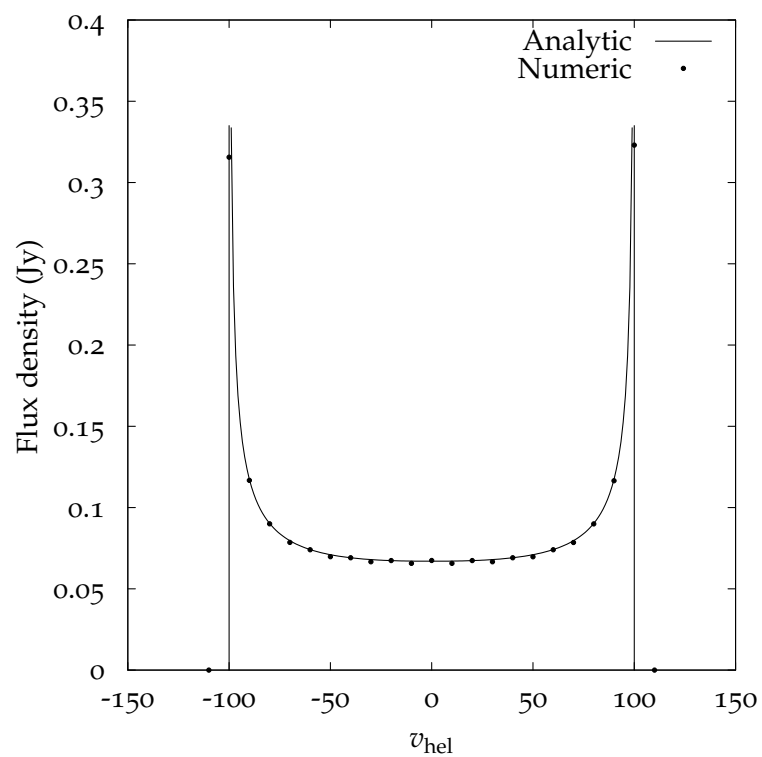
Figure 3.7: Numeric (points) and analytic (line) line profiles for a galaxy with linearly rising and flat rotation curve, and linearly falling surface density.

## 3.2 EFFECT OF VARIOUS PARAMETERS ON THE LINE PROFILE

Before discussing the modeling of actual galaxies, I will discuss the effect of altering various parameters on the overall shape and structure of an H𝟙 line profile.

3.2.1 *Effect of inclination*

Assuming that the H𝟙 motion is in the *x*-*y* plane ($v_z = 0$ as in equation 2.4), and not considering the random motions in a galaxy, the line-of-sight velocity of a galaxy inclined at an angle i is a factor $\sin i$ smaller than that for the same galaxy edge-on (see equation 2.6). Thus, the H𝟙 line profile of a galaxy inclined at an angle i is narrowed by a factor $\sin i$. The galaxy flux (in Jy km s^{-1}) is proportional to the galaxy mass. Therefore, in the absence of self-absorption, the observed H𝟙 flux is independent of inclination. Because of the reduction in width of the H𝟙 profile, the observed flux density at a given velocity increases by a factor $1/\sin i$.

3.2.2 *Effect of random motions*

As shown in section 1.7.3, the effect of random motions is to broaden the line profile of a galaxy. Again, since the integrated flux remains constant as the magnitudes of the random motions are changed in
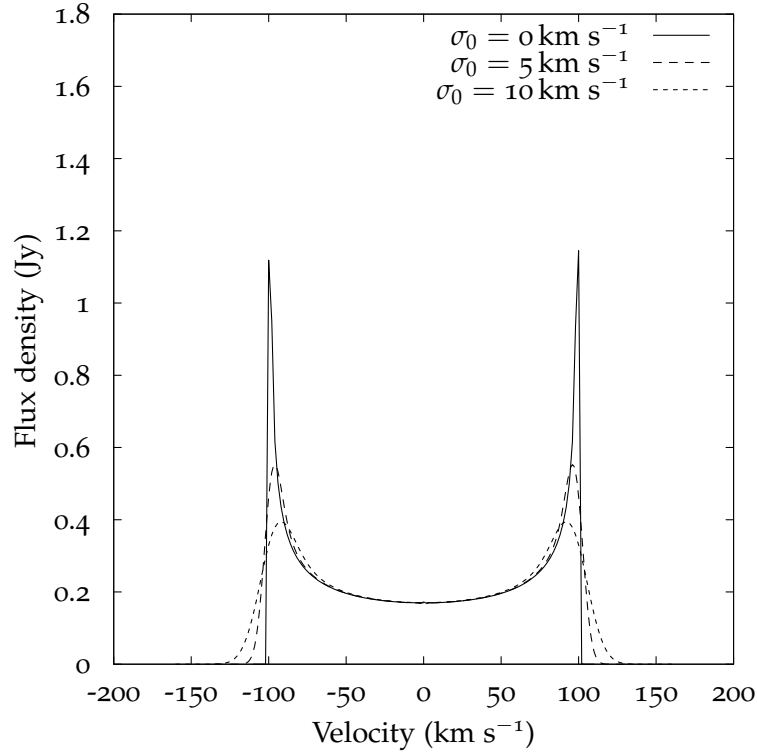
Figure 3.8: Line profile for a galaxy with constant circular speed and uniform density, and three different values of random motions (0, 5, and 10 km s^{-1}).

a in a galaxy, the overall effect is to broaden the profile and bring the peaks of the line profile down. Figure 3.8 shows the effect of changing the turbulent motions on the line profile for the constant circular speed, uniform density galaxy. The effect of finite velocity resolution of the radio telescope is similar.

3.2.3 *Effect of distance*

The effect of galaxy distance is to decrease the total observed flux. The flux density goes down as $1/d^2$, where d is the distance to the galaxy.

3.3 ACTUAL GALAXIES

In this section, I describe the results of the model for some real galaxies for which the rotation curve, density distribution, inclination etc., are available from published data. In order to test the model and make useful predictions from the simulations, the galaxies simulated have a range of inclination angles, line profile widths, and rotation curves. Most of the simulated galaxies are in the Ursa Major Cluster of galaxies, for which aperture high angular resolution aperture synthesis data comes from VSR. These observations allow comparison of a consistent set of data with the simulation, and hence it is easier to compare the model with the observations.

From observations, it is possible to determine the rotation curve and the surface density profiles of a galaxy. The rotation curve is usually obtained by fitting tilted rings to the HI map of the galaxy. Because the SNR in the outer parts of the galaxy is low, and because the line-of-sight velocity is measured only at the approaching and the receding edges of the galaxy, the determination of rotation curve

from aperture synthesis observations is usually limited to radii which are smaller than the radii for which the surface density can be determined. Hence, the published rotation curves usually go out to smaller radii than the surface density plots.

In such cases, two approaches are used to model the galaxy. First, the rotation curve is extrapolated to the same radius as the surface density profile using the last value of velocity as the rotation velocity for all the higher radii. Another approach used is to linearly extrapolate the velocity based upon the last two values of the rotation curve. Because the density in the outer parts of a galaxy is low, these two approaches do not result in any significant differences in the simulated line profiles. Hence, we have used only the first method of extrapolation of velocities for higher radii.

Also, since the tilted ring method of fitting a rotation curve relies on the inclination of the galaxy being known, if the true inclination angle of a galaxy is different than the published value, the rotation curve would also be different. To first order, small changes in inclination modify the rotation curve only by a scale factor in velocity, which has little effect on the conclusions drawn from the galaxy model.

Both instrumental and turbulence broadening have been applied to all the generated line profiles in this section.

3.3.1   UGC 7321

UGC 7321 is a late-type (*Sd*), nearly edge-on ($i = 88° \pm 1°$), low surface brightness (LSB) galaxy. The distance to the galaxy is not certain, with values ranging from ~ 5 Mpc from a kinematical model of the local supercluster (Tully et al., 1992), to 14.9 Mpc from *B*-band TF relation (García-Ruiz et al., 2002). Matthews (2000) used the brightest resolved stars in UGC 7321 from the Hubble Space Telescope to estimate its distance in the range of 10 Mpc $\pm$ 3 Mpc. UGC 7321 is a 'superthin' galaxy. Superthin galaxies have nearly edge-on orientation ($i \approx 90°$), show a near absence of any spheroidal component, and have highly flattened stellar disks ($a/b \gtrsim 10$). UML observed the galaxy with the VLA , and found that the HI distribution ($\rho(r)$) in UGC 7321 is fairly regular and symmetric, and extends to ≈ 1.5 times the stellar radius. The outer disk shows signs of flaring and warping. Matthews & Wood (2003) simulated high-latitude gas in UGC 7321 and found that they got the best fit to the observed data when they included both flaring and warping in their model. UGC 7321 has no nearby neighbors to cause gravitational distortion (UML), so the reasons for the warping and flaring are not clearly understood.

The various parameters of UGC 7321 used in our model are shown in table 3.4. Most of the values in the table come from UML.

Figures 3.9 and 3.10 show the rotation curve and the surface density profile of UGC 7321, as derived by UML.

Parameter	Value	Unit
R.A., α (1950)	12:17:33.8	
Declination, δ (1950)	+22:32:25	
Hubble type (T)	*Sd IV*	
Distance	10	Mpc
P.A.	$82° \pm 0.5°$	
Inclination	$88° \pm 1°$	
D_{HI}	$8'.15 \pm 0'.05$	
Integrated flux	45.3 ± 0.5	Jy km s^{-1}
W_{20}	234.3	km s^{-1}
W_{50}	219.8	km s^{-1}
v_{hel}	406.8	km s^{-1}
Turbulent velocity, σ_0	9	km s^{-1}
Velocity resolution, R	5.2	km s^{-1}

Table 3.4: The parameters used in modeling of UGC 7321. The values are from UML.
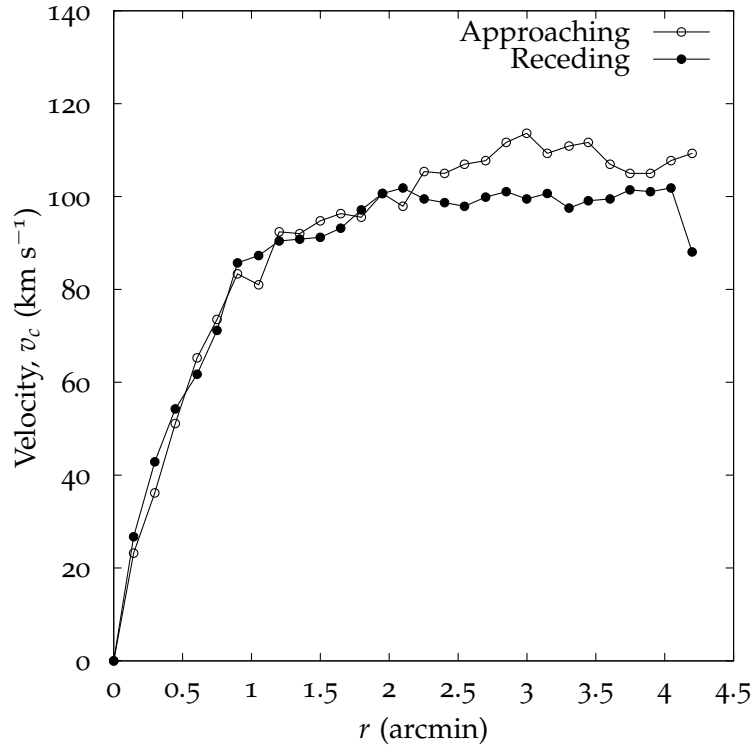
Figure 3.9: Rotation curve for UGC 7321, from UML.
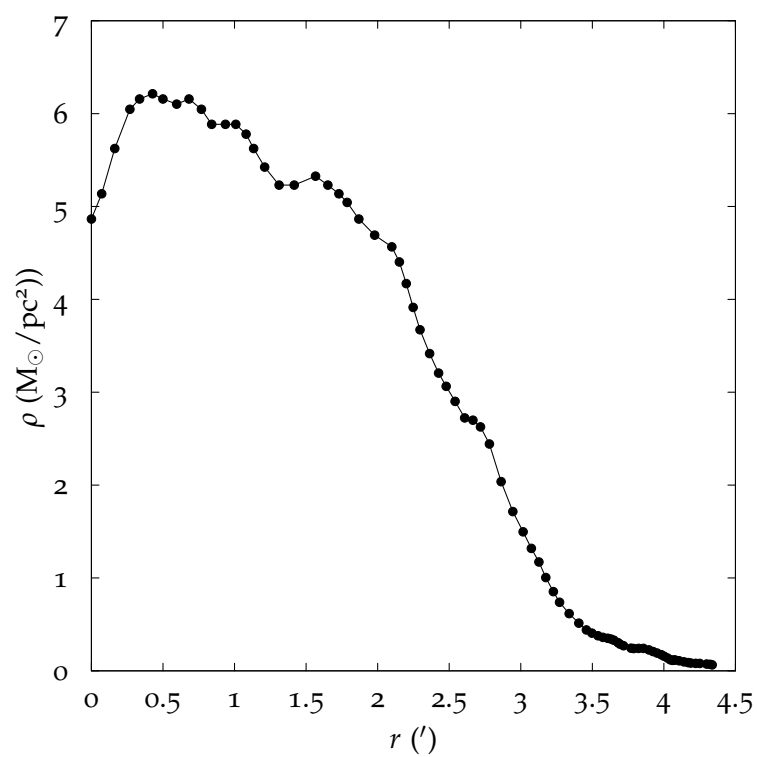
Figure 3.10: Surface density profile for UGC 7321, from UML.
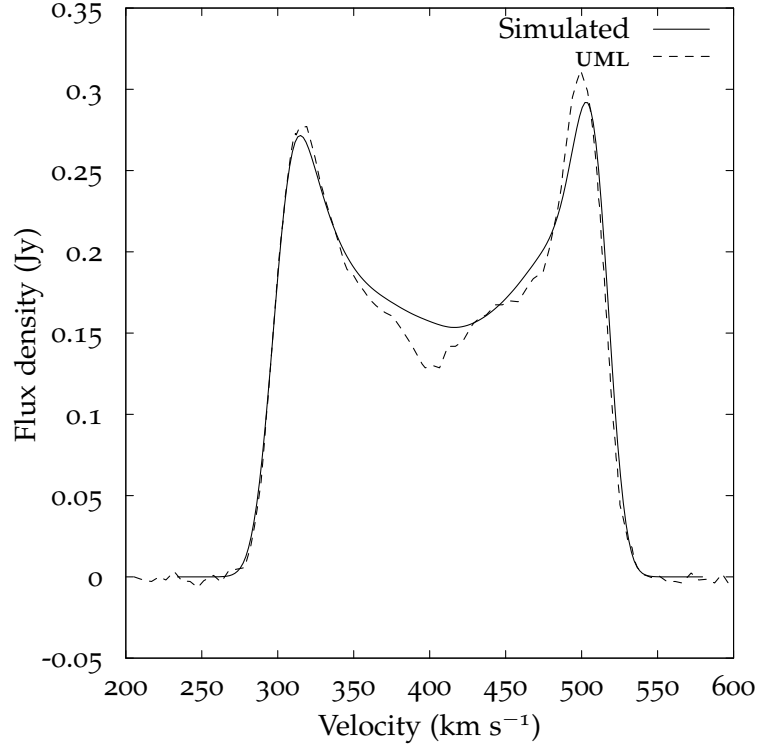
Figure 3.11: Simulated H I line profile for UGC 7321, with parameters from table 3.4, rotation curve from Figure 3.9, and surface density from Figure 3.10. The data for the simulation is from UML.

Using the published rotation curve and density profile, and the parameters from table 3.4, the simulated line profile is shown in Figure 3.11.

The integrated flux in the simulated line profile is 46.1 Jy km s^{-1}, while the flux as measured by UML is 45.3 Jy km s^{-1} (see table 3.4). The linewidths of the simulated profile are $W_{20} = 238.0$ km s^{-1}, $W_{50} = 222.3$ km s^{-1}.

3.3.2 NGC *4088*

NGC 4088 is an *Sbc* galaxy in the Ursa Major Cluster of galaxies, and has been observed in HI by VSR. They found evidence of non-circular motions in the galaxy, so this galaxy serves as a useful test for the model. For the simulation, the turbulent motions have been assumed to be isotropic. The galaxy inclination angle is 69°, and its rotation curve flattens at $v_{\text{flat}} \approx 183 \, \text{km s}^{-1}$. The galaxy rotation speed is much faster than that of UGC 7321, and the inclination angle is closer to face-on. This galaxy therefore serves as a good test for the model in addition to UGC 7321.

Figures 3.12 and 3.13 show the rotation curve and the surface density plot of NGC 4088.

The galaxy parameters used in the simulation are listed in table 3.5.

The simulated line profile, overlaid with the actual line profile of the galaxy is shown in Figure 3.14. The flux in the simulated line profile is 98.9 Jy km s^{-1}, whereas the flux as observed by VSR is 102.9 Jy km s^{-1}. The simulated line widths are $W_{20} = 366.2 \, \text{km s}^{-1}$ and $W_{50} = 340.8 \, \text{km s}^{-1}$.

The simulated line profile shows a few important differences from the observed profile. First, the slopes of the rising and the falling edges are steeper in the simulated profile. This could be due to many factors, such as inclination angle in the simulated
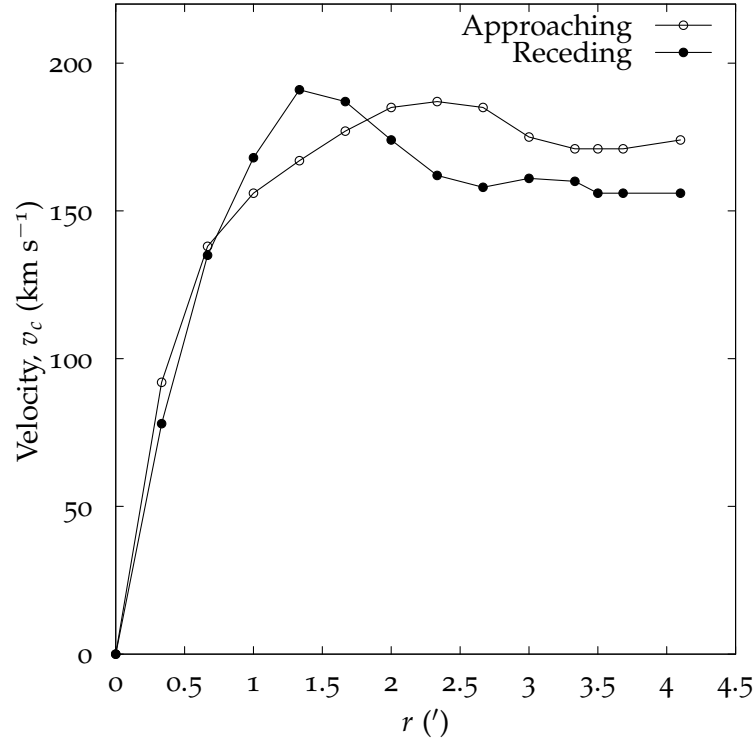
Figure 3.12: Rotation curve for NGC 4088, from VSR.

Parameter	Value	Unit
R.A., α (1950)	12:03:01.9	
Declination, δ (1950)	+50:49:04	
Hubble type (T)	*Sbc*	
Distance	13	Mpc
P.A.	231°	
Inclination	69°	
D_{HI}	8.5′	
Integrated flux	102.9 $\pm$ 1.1	Jy km s^{-1}
W_{20}	371.4	km s^{-1}
W_{50}	342.1	km s^{-1}
v_{hel}	756.7	km s^{-1}
Turbulent velocity, σ_0	10	km s^{-1}
Velocity resolution, R	19.8	km s^{-1}

Table 3.5: The parameters used in modeling of NGC 4088. The values are from VSR.
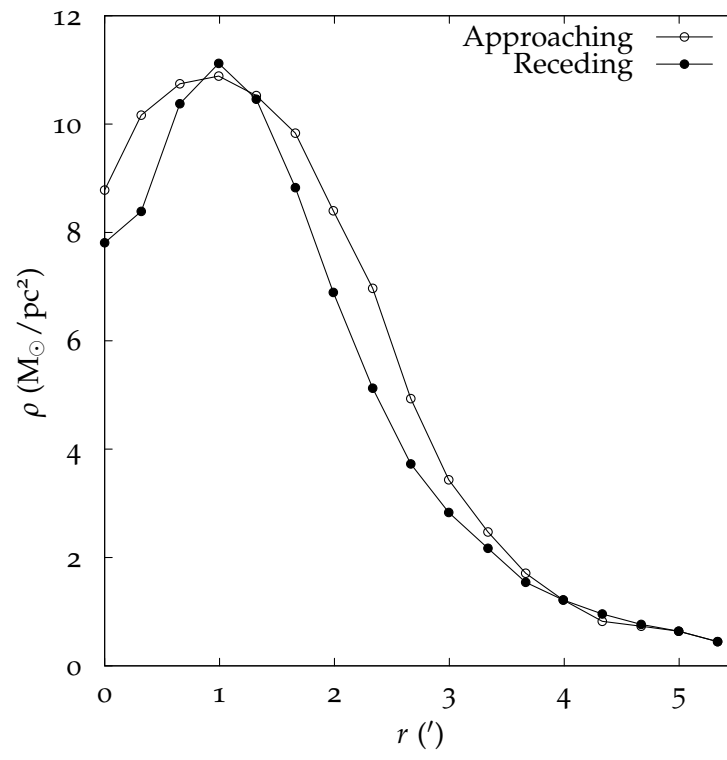
Figure 3.13: Surface density profile for NGC 4088, from VSR.
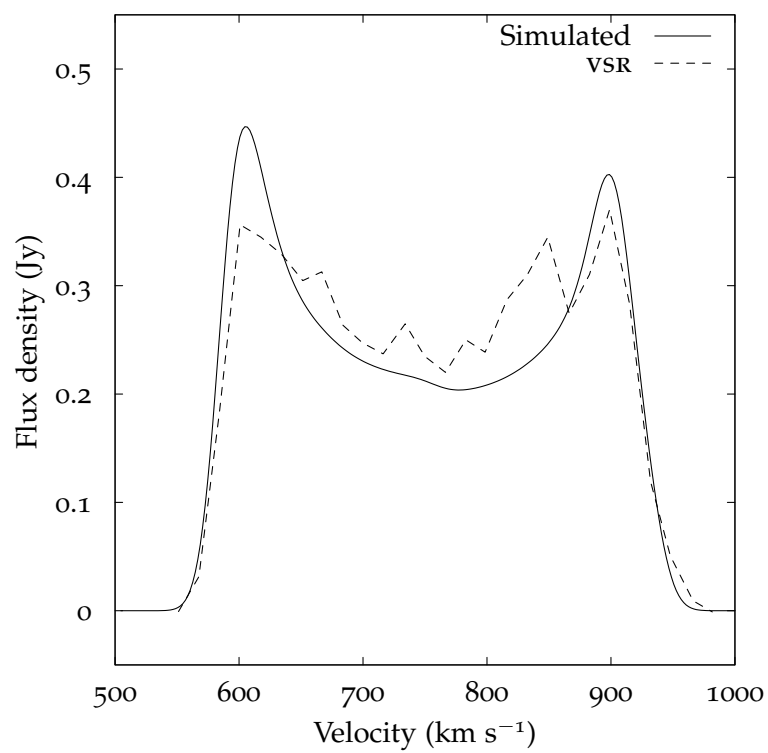
Figure 3.14: Simulated and observed line profiles for NGC 4088.

galaxy being smaller than the 'true' inclination of the galaxy, or the random motions in the simulated profile being lower than that in the galaxy (see section 3.2.2 and 3.2.1). It could also be that the algorithms for deriving rotation curves from aperture synthesis data are subject to minor errors. The effect of making inclination angle larger is to decrease the flux density in the central part of the profile, while an increase in the turbulent velocity does not change that flux – instead, it brings the peaks of the profile down. Increasing the inclination angle also makes the profile wider. The best match is obtained with a turbulent velocity of $15 \, \text{km s}^{-1}$, and an inclination of $65°$. Figure 3.15 shows the simulated line profile in that case. The integrated flux is the same as before (see section 3.2). The line widths now are $W_{20} = 365.0 \, \text{km s}^{-1}$ and $W_{50} = 335.6 \, \text{km s}^{-1}$.

3.3.3   NGC 4100

NGC 4100 is an *Sbc* galaxy observed by VSR using the WSRT . The galaxy parameters are presented in table 3.6. With a declining rotation curve, the galaxy has $v_{\text{max}} \neq v_{\text{flat}}$. Thus, the galaxy serves as an important test for the model.

The galaxy rotation curve and the surface density profile are shown in figures 3.16 and 3.17.

Using the rotation curve and the density profile, and the parameters from table 3.6, the simulated line profile for NGC 4100 is shown
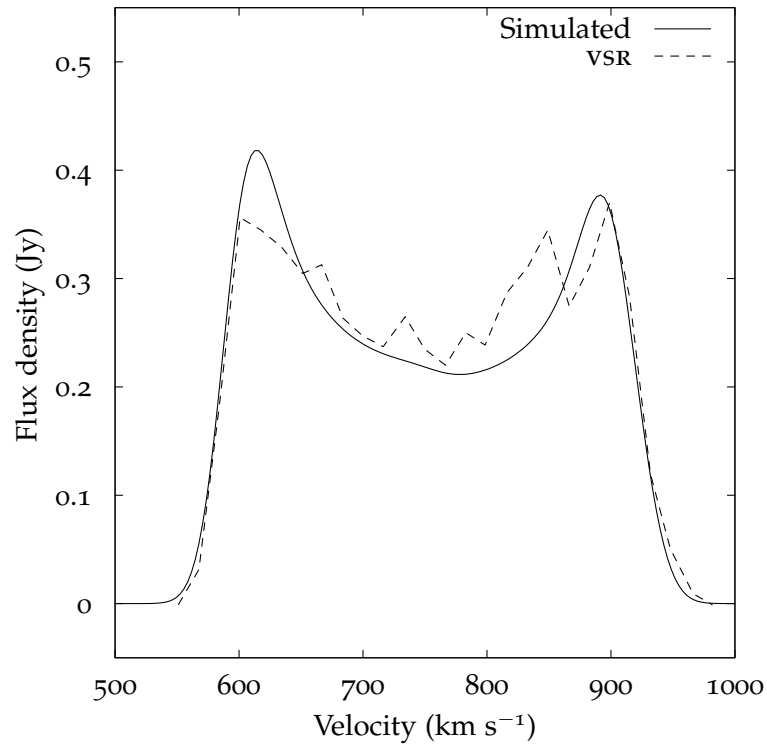
Figure 3.15: Simulated and observed line profiles for NGC 4088. The incli-
nation angle is changed from 69° to 65°, and the turbulent
velocity is changed to 15 km s⁻¹.
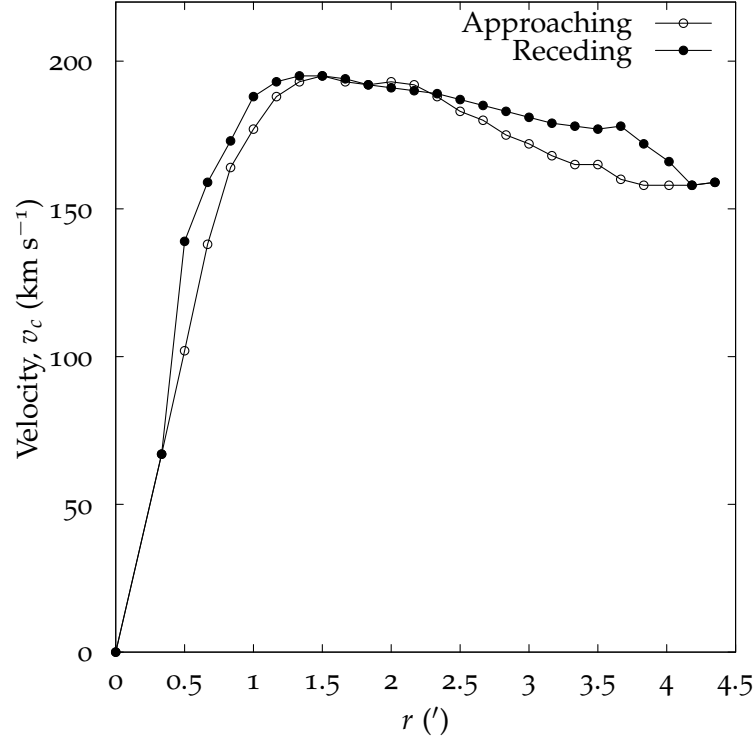
**Figure 3.16:** Rotation curve for NGC 4100, from VSR.

| Parameter	Value	Unit
R.A., α (1950)	12:03:36.4	
Declination, δ (1950)	+49:51:40	
Hubble type (T)	*Sbc*	
Distance	15.6	Mpc
P.A.	347°	
Inclination	70°	
D_{HI}	6.9′	
Integrated flux	41.6 ± 0.7	Jy km s^{-1}
W_{20}	401.8 ± 2.0	km s^{-1}
W_{50}	380.5 ± 1.8	km s^{-1}
v_{hel}	1074.4 ± 1.3	km s^{-1}
Turbulent velocity, σ_0	10	km s^{-1}
Velocity resolution, R	19.93	km s^{-1}

Table 3.6: The parameters used in modeling of NGC 4100. The values are from VSR.
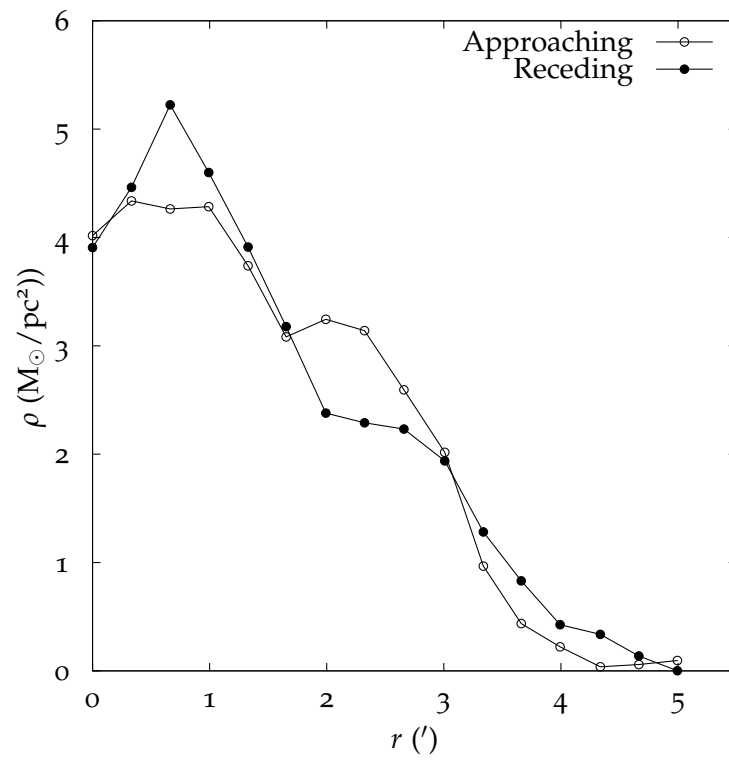
Figure 3.17: Surface density profile for NGC 4100, from VSR.
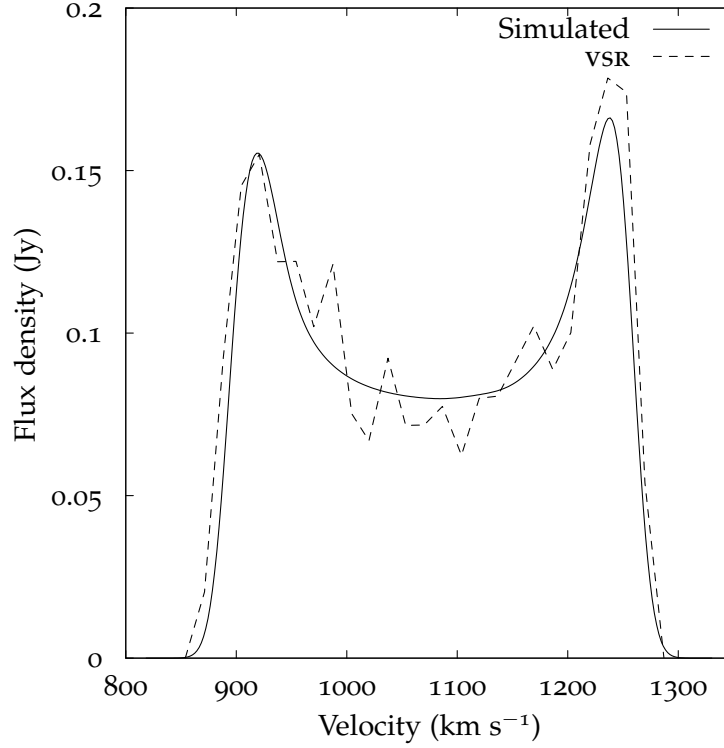
**Figure 3.18:** Simulated and observed line profiles for NGC 4100.

in Figure 3.18. The line profiles are in good agreement, with little difference in the line widths. In particular, the simulated line profile has a width that is a little smaller than the observed width. The integrated H I flux of NGC 4100 as reported by VSR is 41.6 Jy km s^{-1}, whereas the simulated line profile has a flux of 39.6 Jy km s^{-1}. The simulated values for W_{20} and W_{50} are 389.0 km s^{-1} and 367.5 km s^{-1}, which are about 10 km s^{-1} smaller than the observed line widths. This difference could be due to the factors mentioned for NGC 4100.

3.3.4   NGC *4010*

NGC 4010 is an *SBd* galaxy in the Ursa Major Cluster of galaxies, and has been observed by VSR with the WSRT . Table 3.7 lists the relevant parameters for NGC 4010, and figures 3.19 and 3.20 show the rotation curve and the surface density profile for the galaxy. With a rotation curve that keeps rising till almost the end of the observable radius, the galaxy also serves as an important test for the model.

NGC 4010 presents interesting problems for the model, because of the presence of strong warps (VSR). In such a case, accurate determination of inclination, surface density, and precise rotation curve from the observations becomes extremely difficult. As such, the values that are the 'best fit' from the observational data may not be very accurate. Thus, the model has two problems: first, the inclination and density profile data might not be very accurate, and second, the presence of warps means that the line profile is shape could be very different from the non-warped case.

As mentioned above, the simulated line profile is a poor fit to the actual line profile. For getting better results, warps need to be incorporated into the model. The integrated H I flux of NGC 4010 as reported by VSR is 38.2 Jy km s^{-1}, whereas the simulated line profile has a flux of 29.7 Jy km s^{-1}. The simulated values for W_{20} and W_{50} are 274.4 km s^{-1} and 254.4 km s^{-1}, which are in close agreement with the observed values. However, this is probably a coincidence, or the
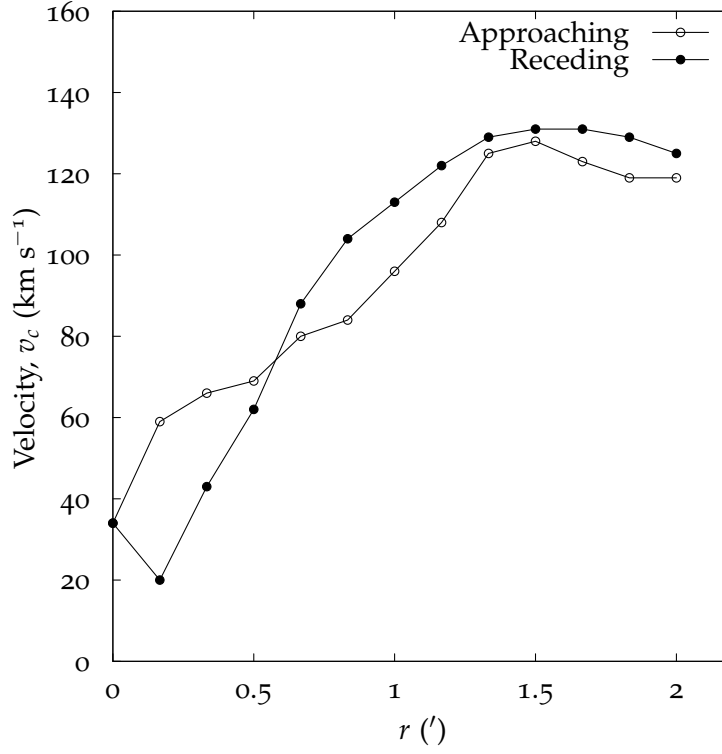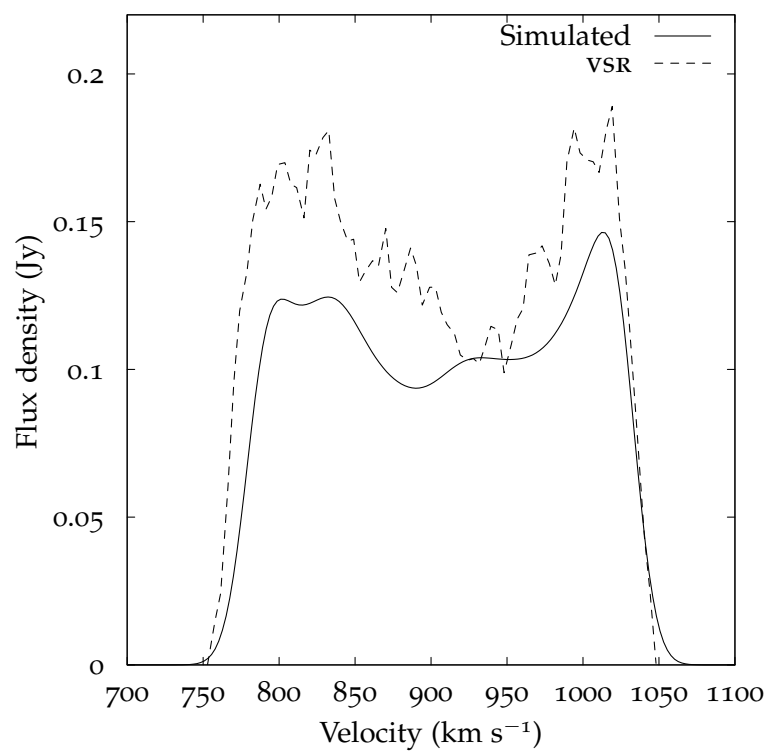
Figure 3.19: Rotation curve for NGC 4010, from VSR.

Parameter	Value	Unit
R.A., α (1950)	11:56:01.6	
Declination, δ (1950)	+47:32:14	
Hubble type (T)	*SBd*	
Distance	15.3	Mpc
P.A.	62°	
Inclination	77°	
D_{HI}	6.7′	
Integrated flux	38.2 ± 0.3	Jy km s^{-1}
W_{20}	277.7 ± 1.0	km s^{-1}
W_{50}	264.1 ± 1.2	km s^{-1}
v_{hel}	901.9 ± 0.8	km s^{-1}
Turbulent velocity, σ_0	10	km s^{-1}
Velocity resolution, R	8.29	km s^{-1}

Table 3.7: The parameters used in modeling of NGC 4010. The values are from VSR.
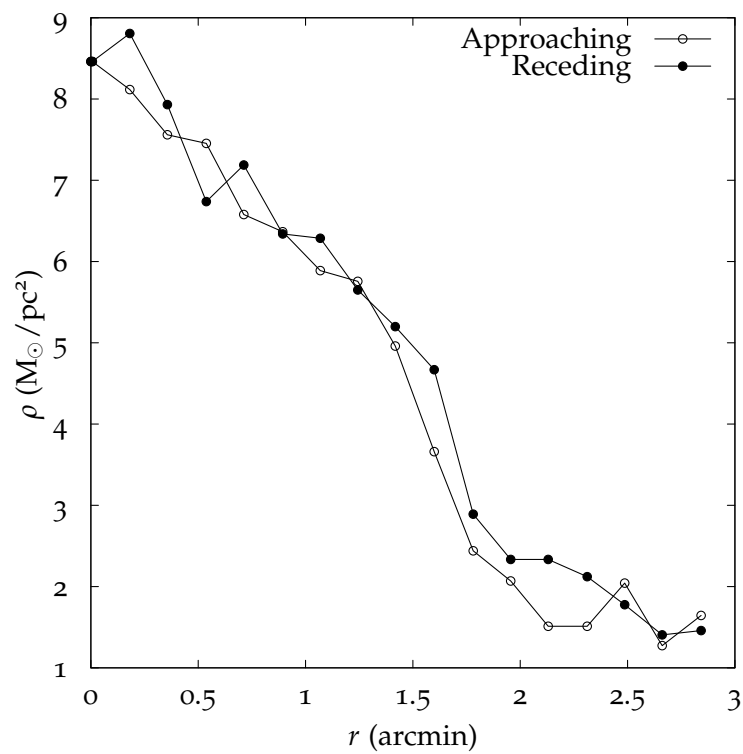
Figure 3.20: Surface density profile for NGC 4010, from VSR.

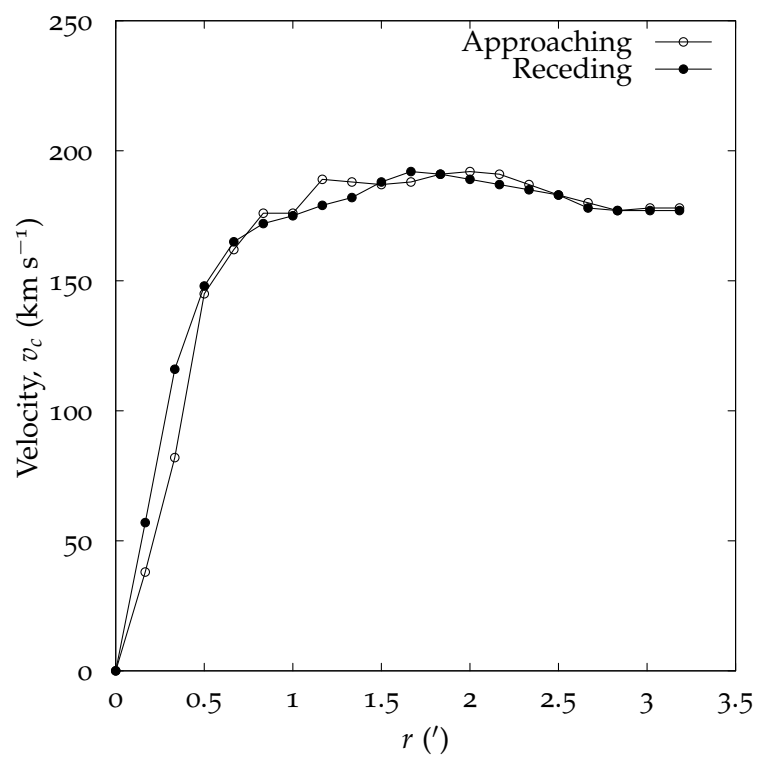**Figure 3.21:** Simulated and observed line profiles for NGC 4010.
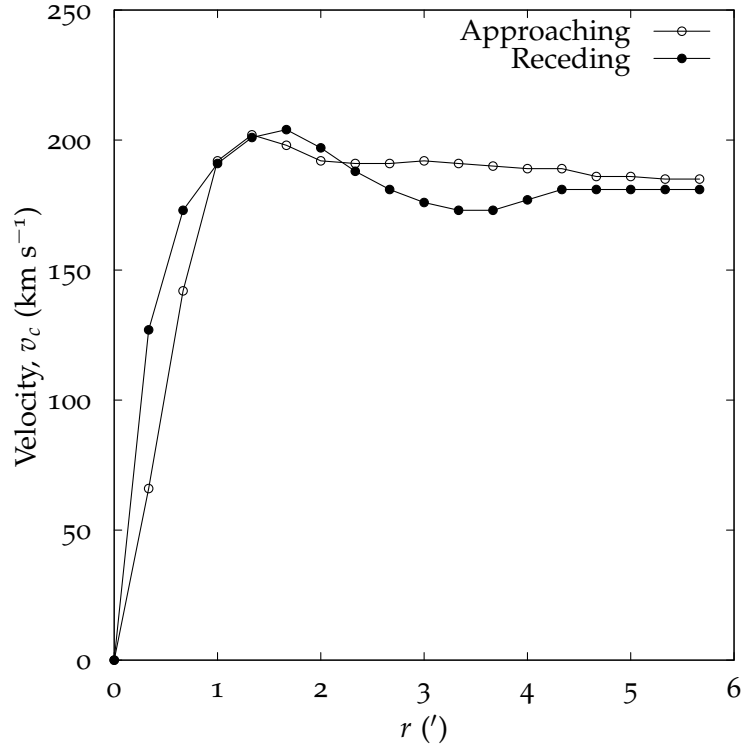
Figure 3.22: Rotation curve for NGC 4157, from VSR.

result of offsetting errors, because the line profiles themselves do not match well.

3.3.5 NGC 4157

NGC 4157 is an *SBd* galaxy in the Ursa Major Cluster of galaxies, and has been observed by VSR with the WSRT . Table 3.8 lists the relevant parameters for NGC 4157, and figures 3.22 and 3.23 show the rotation curve and the surface density profile for the galaxy. NGC 4157 has the highest rotation velocity in the galaxies modeled in this chapter.
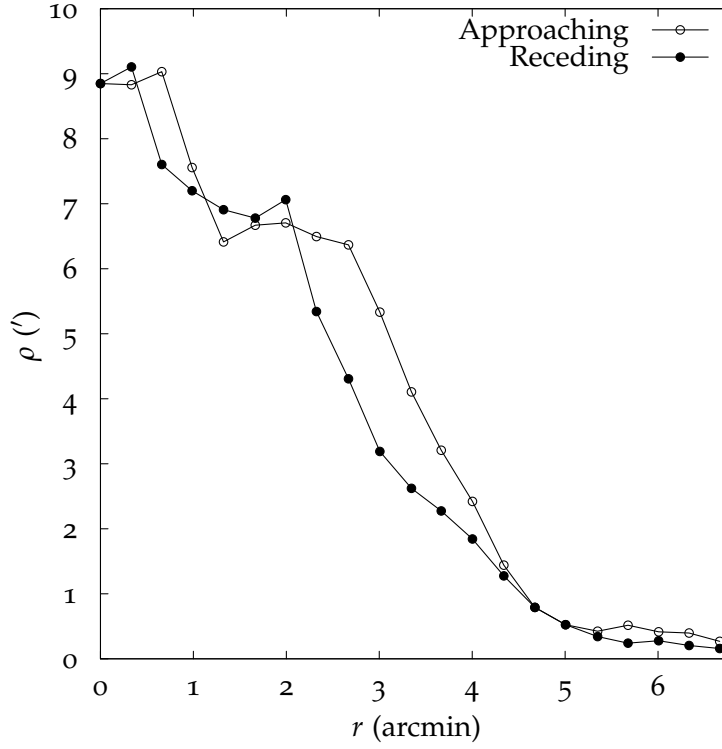
Figure 3.23: Surface density profile for NGC 4157, from VSR.

Parameter	Value	Unit
R.A., α (1950)	12:08:34.2	
Declination, δ (1950)	+50:45:47	
Hubble type (T)	*SBd*	
Distance	11.5	Mpc
P.A.	66°	
Inclination	82°	
D_{HI}	9.2′	
Integrated flux	107.4 ± 1.6	Jy km s^{-1}
W_{20}	427.6 ± 2.2	km s^{-1}
W_{50}	400.7 ± 3.1	km s^{-1}
v_{hel}	774.4 ± 1.8	km s^{-1}
Turbulent velocity, σ_0	12	km s^{-1}
Velocity resolution, R	19.88	km s^{-1}

**Table 3.8:** The parameters used in modeling of NGC 4157. The values are from VSR.
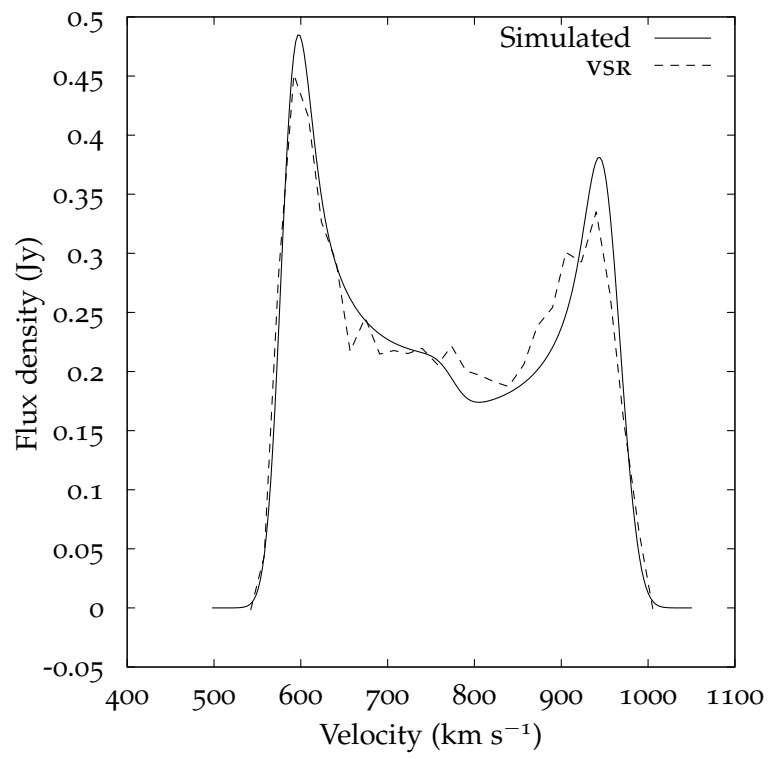
Figure 3.24: Simulated and observed line profiles for NGC 4157.

Parameter	Value	Unit
R.A., α (1950)	12:13:21.6	
Declination, δ (1950)	+47:22:11	
Hubble type (T)	*SBd*	
Distance	17.0	Mpc
P.A.	230°	
Inclination	85°	
D_{HI}	6.4$'$	
Integrated flux	33.8 ± 0.7	Jy km s^{-1}
W_{20}	428.1 ± 5.1	km s^{-1}
W_{50}	395.6 ± 3.8	km s^{-1}
v_{hel}	1028.8 ± 2.7	km s^{-1}
Turbulent velocity, σ_0	10	km s^{-1}
Velocity resolution, R	33.20	km s^{-1}

Table 3.9: The parameters used in modeling of NGC 4217. The values are from VSR.

The integrated flux in NGC 4157 is 107.5 Jy km s^{-1} (VSR), whereas the simulated line profile has a flux of 106.9 Jy km s^{-1}. The simulated values for W_{20} and W_{50} are 416.9 km s^{-1} and 391.0 km s^{-1}. The model and the observational data are in good agreement.

3.3.6   NGC 4217

NGC 4217 is an *SBd* galaxy in the Ursa Major Cluster of galaxies, and has been observed by VSR with the WSRT . Table 3.9 lists the relevant parameters for NGC 4217, and figures 3.25 and 3.26 show the rotation curve and the surface density profile for the galaxy.

Figure 3.25: Rotation curve for NGC 4217, from VSR.
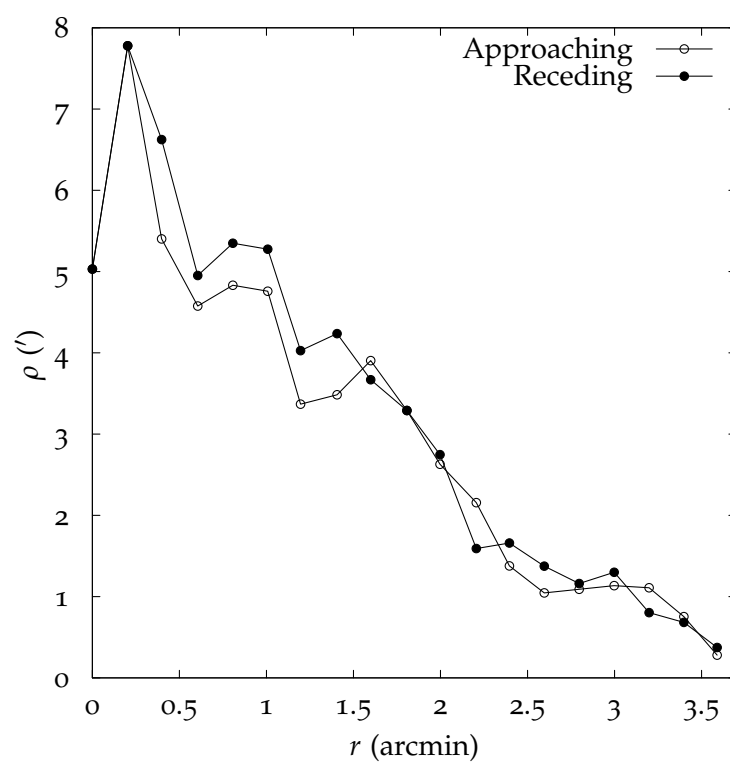
Figure 3.26: Surface density profile for NGC 4217, from VSR.
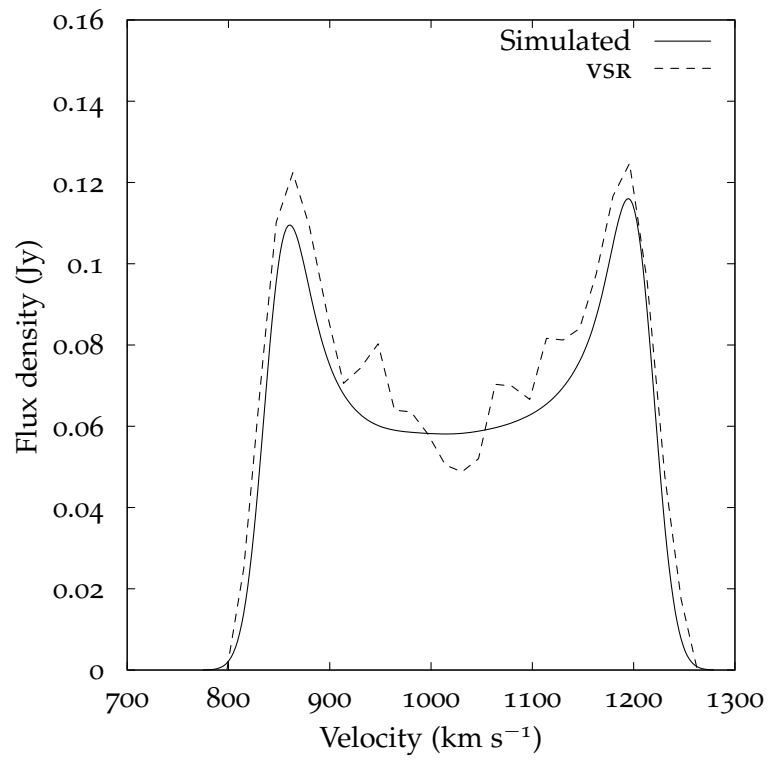
Figure 3.27: Simulated and observed line profiles for NGC 4217.

Parameter	Value	Unit
R.A., α (1950)	11:54:43.1	
Declination, δ (1950)	+49:33:44	
Hubble type (T)	SBd	
Distance	13.4	Mpc
P.A.	$31°$	
Inclination	$28°$	
D_{HI}	$6.4'$	
Integrated flux	42.7 ± 0.3	Jy km s^{-1}
W_{20}	136.5 ± 0.5	km s^{-1}
W_{50}	122.1 ± 0.7	km s^{-1}
v_{hel}	777.2 ± 0.4	km s^{-1}
Turbulent velocity, σ_0	10	km s^{-1}
Velocity resolution, R	8.29	km s^{-1}

Table 3.10: The parameters used in modeling of UGC 6930. The values are from VSR.

The integrated flux of NGC 4217 is 33.8 Jy km s^{-1} (VSR), whereas the simulated line profile has a flux of 30.2 Jy km s^{-1}. The simulated values for W_{20} and W_{50} are 418.7 km s^{-1} and 390.8 km s^{-1}.

3.3.7 UGC *6930*

UGC 6930 is an *SBd* galaxy in the Ursa Major Cluster of galaxies, and has been observed by VSR with the WSRT . Table 3.10 lists the relevant parameters for UGC 6930, and figures 3.28 and 3.29 show the rotation curve and the surface density profile for the galaxy. UGC 6930 is the slowest rotating galaxy of the sample, with $v_{\mathrm{max}} \approx 110$ km s^{-1}.

The simulated line profile for UGC 6930 shows some minor differences with the actual profile. The width of the simulated profile is
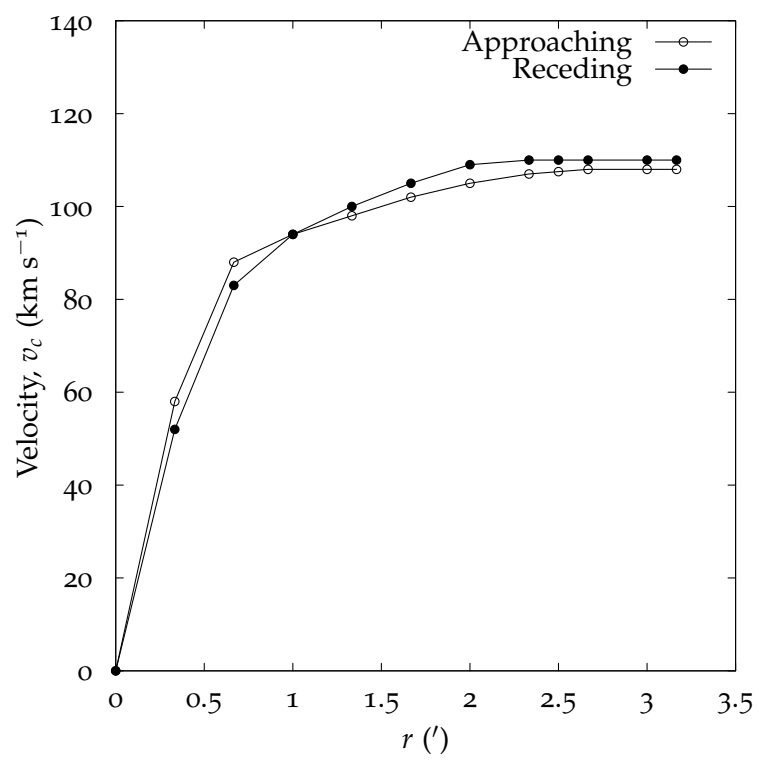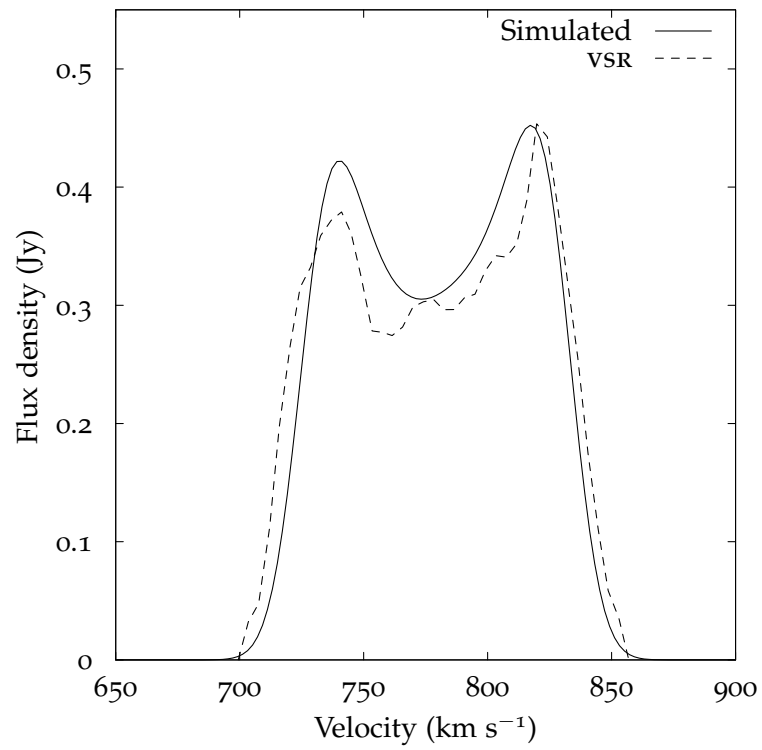
Figure 3.28: Rotation curve for UGC 6930, from VSR.
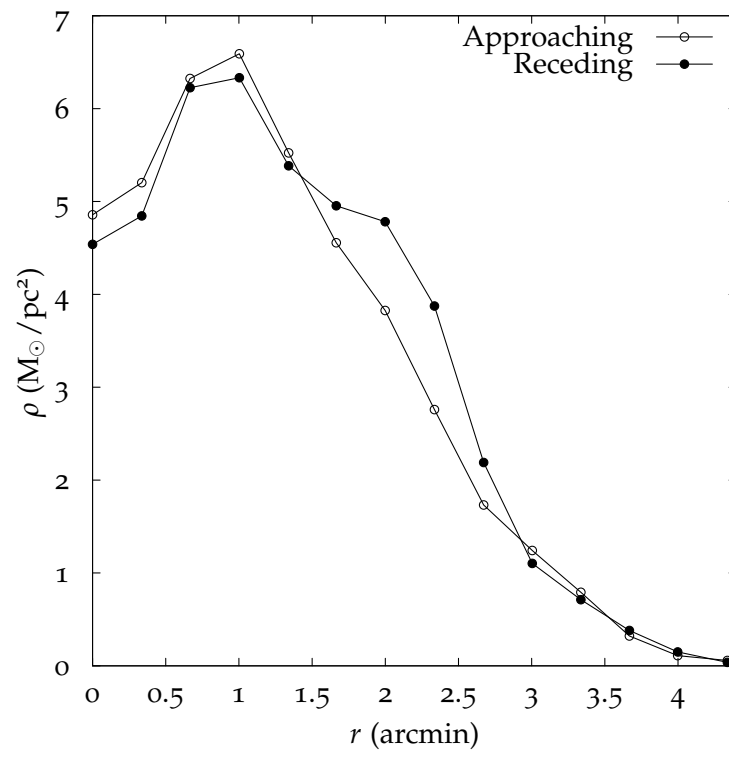
Figure 3.29: Surface density profile for UGC 6930, from VSR.

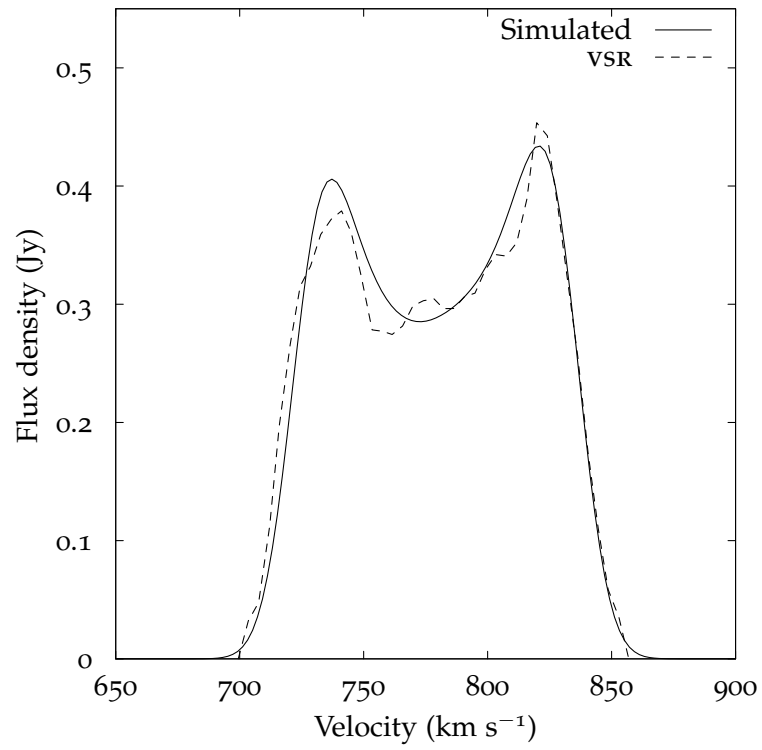**Figure 3.30:** Simulated and observed line profiles for UGC 6930.

smaller, and the overall flux density is higher in the center. If the inclination angle of the galaxy is changed from 28° to 30°, the resulting simulated line profile is much closer to the actual (observed) profile.

The low inclination angle of UGC 6930 means that the determination of an accurate inclination angle and rotation curve for this galaxy is very difficult (Begeman, 1987). The inaccuracies in the rotation curve and inclination angle determined from the observations can account for the differences in the simulated line profiles. The model serves as an important consistency check on the rotation curves and inclination angles derived from the observations. The lack of a good match between the simulated and the observed line profiles shows that the rotation curves and inclination angles as derived from the observations are not very accurate, and also that the derived values are not self-consistent with the observed data.

The integrated flux of UGC 6930 is 42.7 Jy km s^{-1} (VSR), whereas the simulated line profile has a flux of 43.2 Jy km s^{-1}. The simulated values for W_{20} and W_{50} are 126.7 km s^{-1} and 110.8 km s^{-1}. After changing the inclination to 30°, the values of W_{20} and W_{50} are 133.2 km s^{-1} and 117.4 km s^{-1}.

3.4 COMPARISON OF THE MODEL WITH THE OBSERVATIONS

With the results from the model as described in the previous section, it is possible to compare them with the observations quantitatively.

Figure 3.31: Simulated and observed line profiles for UGC 6930. The inclination angle has been changed from 28° to 30°.

The percentage difference between the simulated line widths and the observed line widths is defined as:

$$p(l) = 100 \frac{W_{l,\text{observed}} - W_{l,\text{simulated}}}{W_{l,observed}}, \qquad (3.20)$$

where the subscript l is used to denote the level at which the widths are measured (20% or 50%).

Figure 3.32 shows a plot of the percentage difference using W_{20}, $p(20)$ as a function of the observed value of W_{20}. Similarly, Figure 3.33 shows the plot of the percentage difference using W_{50}, $p(50)$ as a function of the observed value of W_{50}. The simulated widths are obtained with the original galaxy parameters, even for NGC 4088 and UGC 6930.

From the figures, it can be seen that the percentage difference between the simulated and the observed line widths can be as much as $\approx 10\%$. UGC 7321 is the only galaxy in the sample with the observed line width smaller than the simulated width. This is interesting, because UGC 7321 is the only galaxy in the sample that is not from VSR's survey of galaxies in the Ursa Major Cluster of galaxies.

A plot of the percentage difference in the fluxes, defined in the same way as in equation 3.20 is shown in Figure 3.34.

With the results for the 7 galaxies above, it can be seen that the simulated line profiles are different from the observed profiles in a few respects. Some differences are expected, even if the published rotation curves and surface density profiles are accurate. The velocity
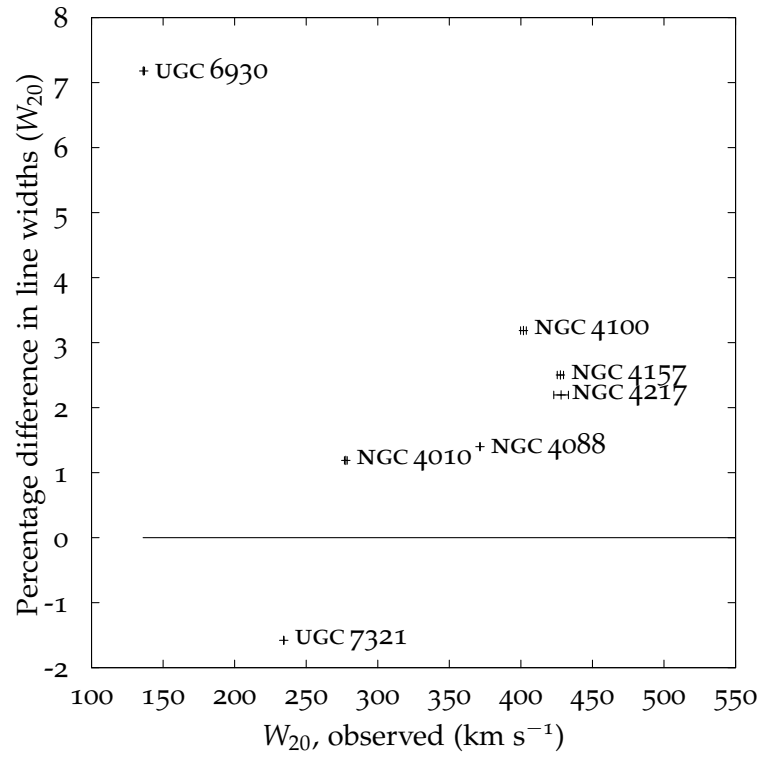
Figure 3.32: Percentage difference between the observed and the simulated (W_{20}) as a function of the observed line width. The horizontal error-bars represent the errors in the observation, if available.
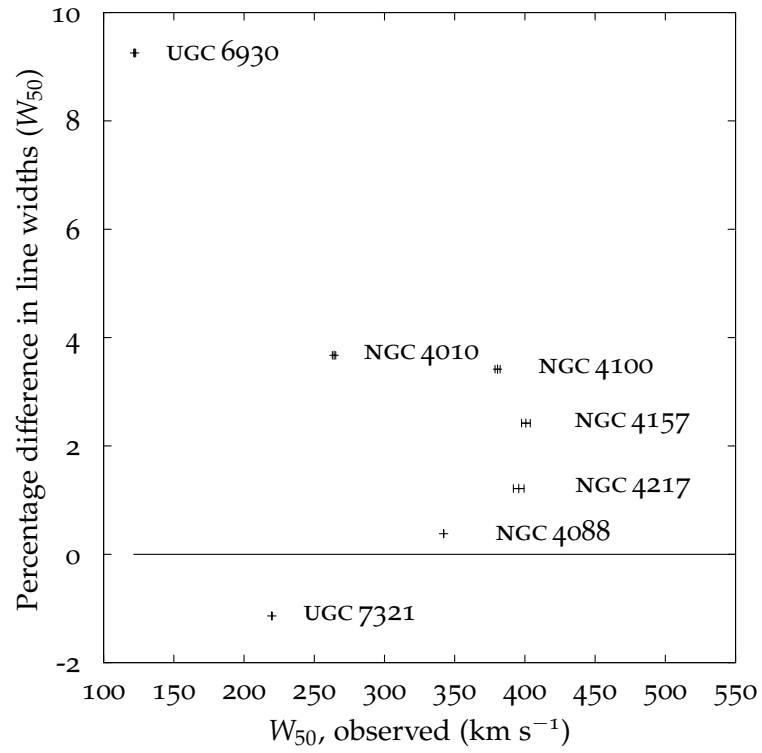
Figure 3.33: Percentage difference between the observed and the simulated (W_{50}) as a function of the observed line width. The horizontal error-bars represent the errors in the observation, if available.
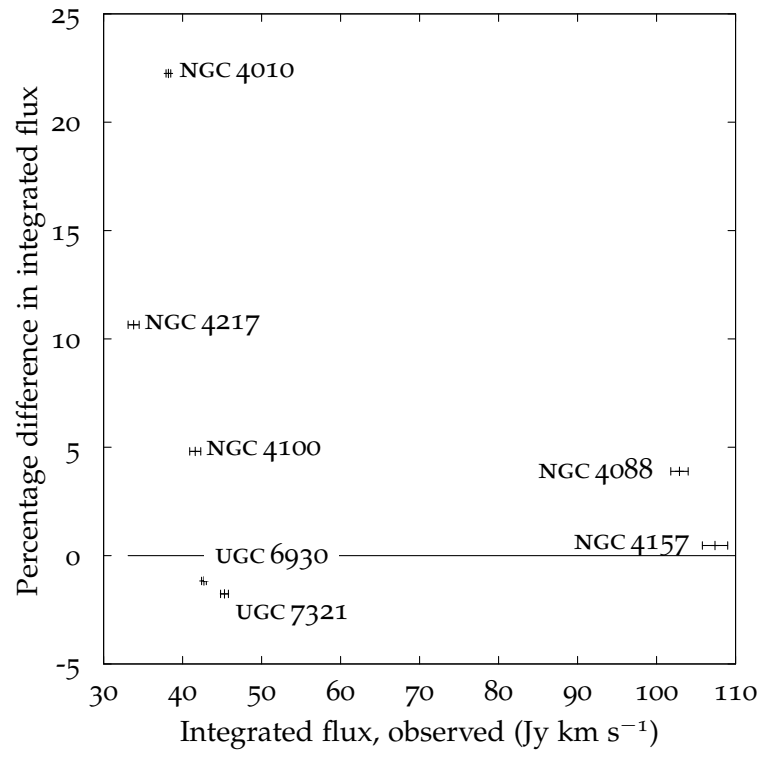
Figure 3.34: Percentage difference between the simulated and observed Hı fluxes as a function of the observed flux.

and surface density distributions in a real galaxy are complex, and using their azimuthal averages will result in differences in the simulated profiles. Similarly, the line-of-sight turbulent motions are not constant for the galaxy, and assuming them to be constant adds to the differences between the observed and simulated line profiles. But these factors alone are unable to explain the amount of differences shown in Figures 3.32–3.34. Specifically, a difference of $\approx$ 10% in the line widths can only be explained by a lack of consistency in the rotation curves, inclinations, and surface density profiles determined from observations.

The integrated fluxes are different by upto $\approx$ 20% from the observed fluxes. Aperture synthesis telescopes miss H$\textsc{i}$ flux in large-scale structures (Taylor et al., 1999). The total H$\textsc{i}$ mass of a galaxy can be calculated from its surface density distribution by integrating it as a function of radius:

$$M_{\mathrm{HI}} = \int_0^R 2\pi r \rho(r) \mathrm{d}\, r. \tag{3.21}$$

This mass can then be converted to flux using equation 2.2. Combining equations 3.21 and 2.2 results in an expression for M_{HI} which depends only upon the angular size of the galaxy, and not its distance. Thus, the mass is independent of other derived factors such as rotation curve, galaxy distance, and depends only upon the surface density profile. The simulated fluxes, derived using equation 2.2, show a difference of upto $\approx$ 20% from the observed fluxes. Even after

discarding the data point for NGC 4010 in Figure 3.34, the differences between the observed and the integrated HI fluxes can be 10%.

RESULTS

कर्मण्येवाधिकारस्ते मा फलेषु कदाचन।
मा कर्मफलहेतुर्भूर्मा ते सङ्गोऽस्त्वकर्मणि॥

श्रीमद्भग्वद्गीता

So far, I have discussed the physical and software model, and used it on a diverse sample of galaxies (chapter 3) in addition to simple velocity- and density-distributions to show that the model is successful at creating single-dish H$_I$ line profiles given some observables for galaxies. The model successfully creates line profiles for simple velocity and density distributions, and they match extremely well with the predicted line profiles for those distributions. For galaxies with interferometric data, the model is successful in creating most H$_I$ line profiles to errors within less than 10% or so, both in integrated H$_I$ flux and also in the line widths.

It is important to emphasize that the model contains, by definition, *known* galaxy parameters, even if they do not correspond to the real parameters of the galaxies from which they are derived to better than 5 or 10%. This allows one to precisely test the accuracy of corrections used in the literature. In particular, the various tur-

bulent motion and instrumental resolution corrections described in sections 1.7.2 and 1.7.3 can be applied to HI line profiles generated from the model, and the effect of corrections on the line profile widths can be studied precisely. In order to do that, I will use the model to generate line profiles for a set of galaxies with a range of turbulent velocities and inclinations that are physically realistic. Turbulent velocity and instrumental resolution corrections should return the line widths that are equal to the zero-turbulence case in the model.

To conserve space and avoid repetition, some of the results are presented only for a subset of galaxies described in chapter 3, but they apply to all of the galaxies modeled.

4.1 EFFECT OF GALAXY ROTATION

As described in section 2.2.1, a galaxy can be rotated in the x-y plane by an angle ψ. Changing the rotation angle of a galaxy with no azimuthal dependence of its parameters has no effect on any of its observed properties. In this section, I discuss the effect of rotation on the observed properties of NGC 4088 and NGC 4157, where the rotation curves and HI density are different for the two halves of the galaxies. For this, the galaxy rotation angle is changed in steps of 10° from 0° to 360°.

4.1.1 NGC *4088*

Figure 4.1 shows a plot of the observed W_{20} and W_{50} as a function of the rotation angle, ψ. Since W_{50} is measured at a higher flux level than W_{20}, and line profile asymmetries are more prominent at higher fluxes, changing the rotation angle affects W_{50} more than W_{20}. A curious feature of figure 4.1 (and the same plot for NGC 4157) is the existence of the flat portions in the two plots, for example for $\psi \lesssim 50°$. This can be explained by the fact that the areas near the peaks of the line profiles are determined mostly by points moving almost directly along the line-of-sight of observations, and these points do not get affected by the rotation of the galaxy unless the rotation is $\gtrsim 50°$.

Figure 4.2 shows the HI line profiles for NGC 4088 for three different values of the rotation angle ($\psi = 0°, 90°, 180°$). A rotation by 90° makes the galaxy symmetric about the line of sight (see Figure 2.1), so the simulated line profile is symmetrical as well. For a galaxy rotated by 180°, the line profile is the mirror image of the line profile in the case of no rotation.

4.1.2 NGC *4157*

Figure 4.3 shows a plot of the observed W_{20} and W_{50} as a function of the rotation angle, ψ. As expected, W_{50} is more sensitive to ψ than W_{20}.
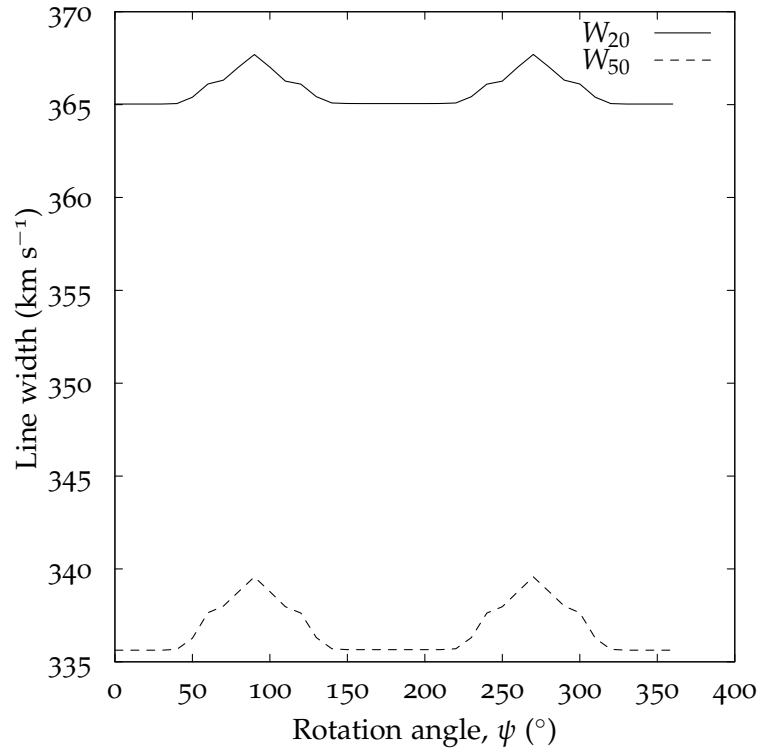
Figure 4.1: Plot of the observed W_{20} and W_{50} for NGC 4088 as a function of the rotation angle ψ, in degrees. The width W_{50}, being measured at a higher level than W_{20} is affected more by the change in the rotation angle.
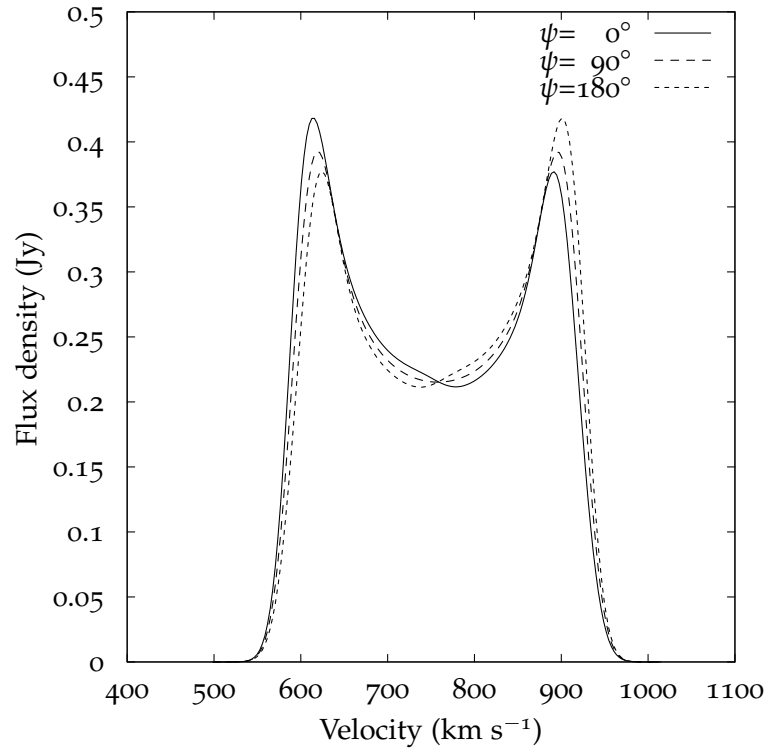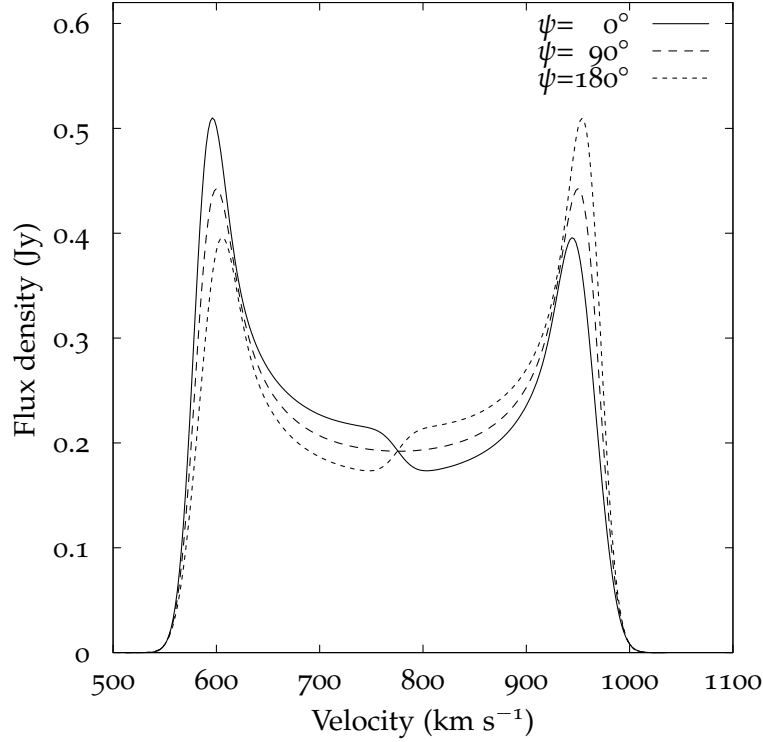
Figure 4.2: Plot of the simulated line profiles for NGC 4088 for three different values of the rotation angle.
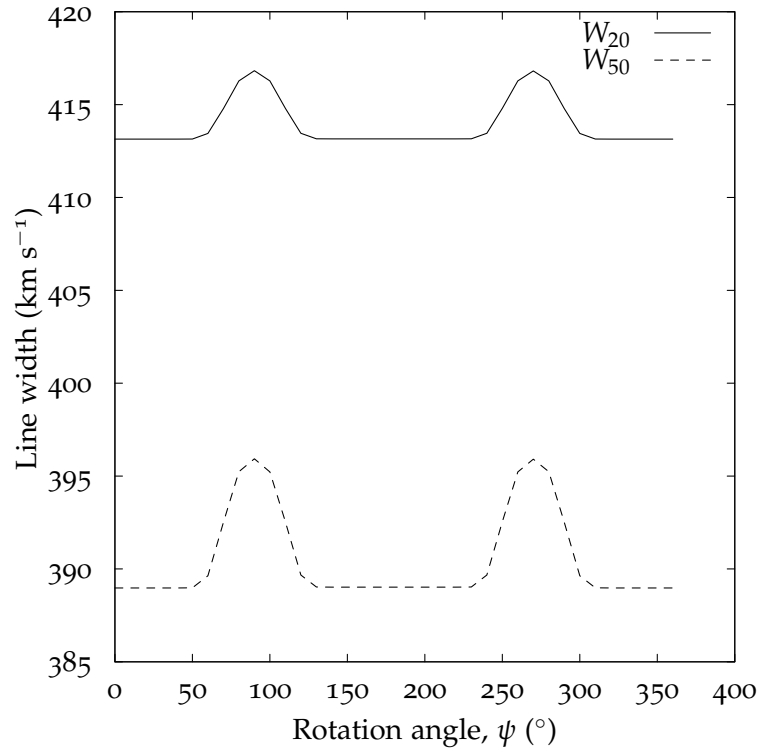
Figure 4.3: Plot of the observed W_{20} and W_{50} for NGC 4157 as a function of the rotation angle ψ, in degrees. The width W_{50}, being measured at a higher level than W_{20} is affected more by the change in the rotation angle.

Figure 4.4 shows the HI line profiles for NGC 4157 for three differ-ent values of the rotation angle ($\psi = 0°, 90°, 180°$). Once again, the line profiles at $\psi = 0°$ and $\psi = 180°$ are mirror images of each other, and the line profile at $\psi = 90°$ is symmetric.

Figure 4.4: Plot of the simulated line profiles for NGC 4157 for three different values of the rotation angle.

Based upon these results, the estimated error in line widths of galaxies with the current model could be as high as $\approx 5\,\mathrm{km\ s^{-1}}$ for W_{20} and $\approx 7\,\mathrm{km\ s^{-1}}$ for W_{50} due to galaxy orientation with azimuthal dependence of rotation velocity and HI distribution. A more complete study of the effect is warranted.

4.2 TURBULENT MOTION CORRECTION

To study the effects of various turbulent motion corrections as described in section 1.7.2, the galaxy described in section 3.1.1 (constant circular speed, uniform surface density) is discussed, and then some of the actual galaxies from section 3.3 are considered.

The turbulent motion corrections applied follow three methods: that from BGPV, TFq, and VSR. Using these three methods will help us in understanding the relative abilities of different turbulent motion correction algorithms.

According to BGPV, the broadening of the line profile at level l of the peak is given by equations 1.19, 1.20 and 1.22. Specifically, the correction to the observed line width according to BGPV is:

$$W_{t,l} = 2\sigma_z \frac{s}{\sqrt{s^2 - (s^2 - 1)\sin^2 i}} k(l), \qquad (4.1)$$

where all the symbols are defined in section 1.7.2. As mentioned in that section, for a Gaussian broadening, $k(20) = 1.80$, and $k(50) = 1.18$. They found that $k(20) = 1.89$, and $k(50) = 0.71$ resulted in a better TF relation, suggesting non-Gaussian broadening. Hence, I have adopted the latter values (1.89 and 0.71) for the correction. Also, I have taken $s = 1$, which means that the turbulent motions in the x-, y-, and z-directions are equal. This is different from $s = 1.5$ assumed by BGPV, but results in a more direct comparison with corrections

from other investigators which all assume $s = 1$. Using the above values, equation 4.1 becomes:

$$W_{t,l} = 2\sigma_z k(l). \tag{4.2}$$

TFq's correction is shown in equation 1.23. The correction proposed by VSR is simpler, because they did not decouple σ_0 and $k(l)$. The correction is given in equation 1.24.

As mentioned in section 1.7.3, there are two parameters that broaden the H I line profile that are relevant here. First is the turbulent motion in the neutral hydrogen in the galaxy itself, and second is the finite resolution R of the observing telescope. While VSR and Bottinelli et al. (1990) account for the instrumental resolution effects in their formulations, it is instructive to first 'decouple' the two parameters by setting $R = 0$. This ensures that the comparison between the various methods is affected only by the turbulent motions in the galaxy, and not because of differences in the correction for R, or the absence of such a correction. Also, as mentioned in section 1.7.2, the finite instrumental resolution broadens the line profile by an amount given by equation 1.30 only if the galaxy line profile is two delta functions. Therefore, equation 1.30 might under-correct for instrumental broadening, and the width VSR obtain after applying this correction might be higher than that obtained in the case when $R = 0 \, \text{km s}^{-1}$.

Once this comparison is done, the effect of finite resolution $R \neq 0$ on the correction can be studied. Note that the broadening due to finite instrumental resolution, as suggested by VSR in equation 1.30 reduces to 0 for $R = 0$, as expected.

In order to study the effects of all the corrections on the corrected line-profile widths, the turbulent motion in a simulated galaxy is varied from $2 \, \mathrm{km \, s^{-1}}$ to $20 \, \mathrm{km \, s^{-1}}$. Therefore, the range of turbulent velocities used spans the typical values of turbulent motions in a galaxy (most galaxies have turbulent velocities in the range of $\sim 7 \, \mathrm{km \, s^{-1}} - 15 \, \mathrm{km \, s^{-1}}$). Also, the corrected line width is converted to v_{max} according to equation 1.20. This helps in testing the assumption that the corrected line widths represent v_{max}.

4.2.1 *Constant circular speed, uniform density galaxy*

As described in section 3.1.1, this 'galaxy' has a rotation curve that is constant at $100 \, \mathrm{km \, s^{-1}}$. The surface density of the galaxy is also constant. For a complete description of the parameters of this galaxy, see table 3.1.

The effect of changing the random motions in this galaxy can be seen in Figure 3.8. By changing the turbulent velocities in this galaxy, and with the instrumental resolution set to zero, the turbulence-corrected line half-widths are shown in Figure 4.5. For comparison, the uncorrected line half-widths are also shown in the figure.
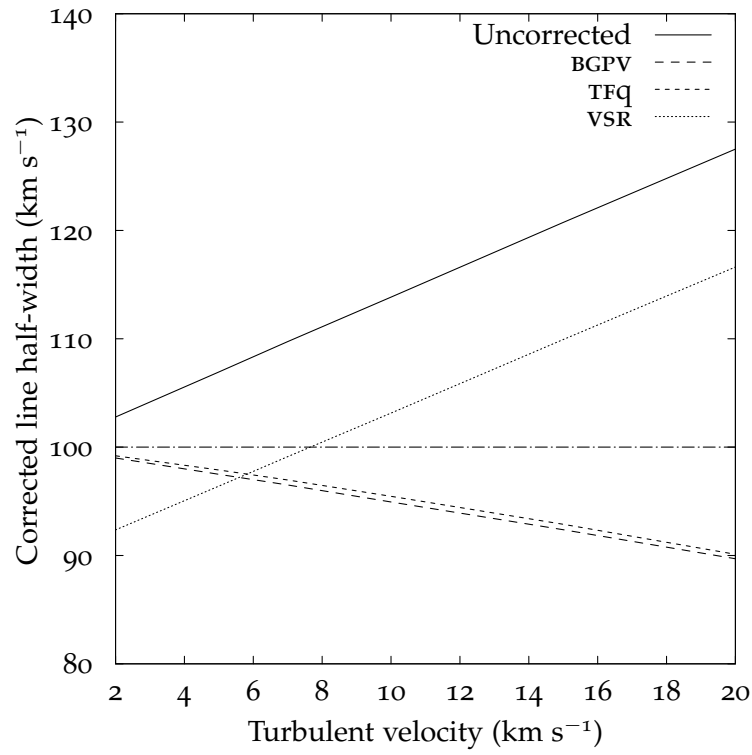
Figure 4.5: The turbulence and inclination corrected line half-widths for the constant circular speed, uniform density galaxy as described in section 3.1.1, at 20% of the peak (using W_{20}). The horizontal line shows the value of v_{max} ($v_{max} = 100\,km\,s^{-1}$).

Similarly, Figure 4.6 shows the corrected half-widths for the galaxy using the above algorithms.
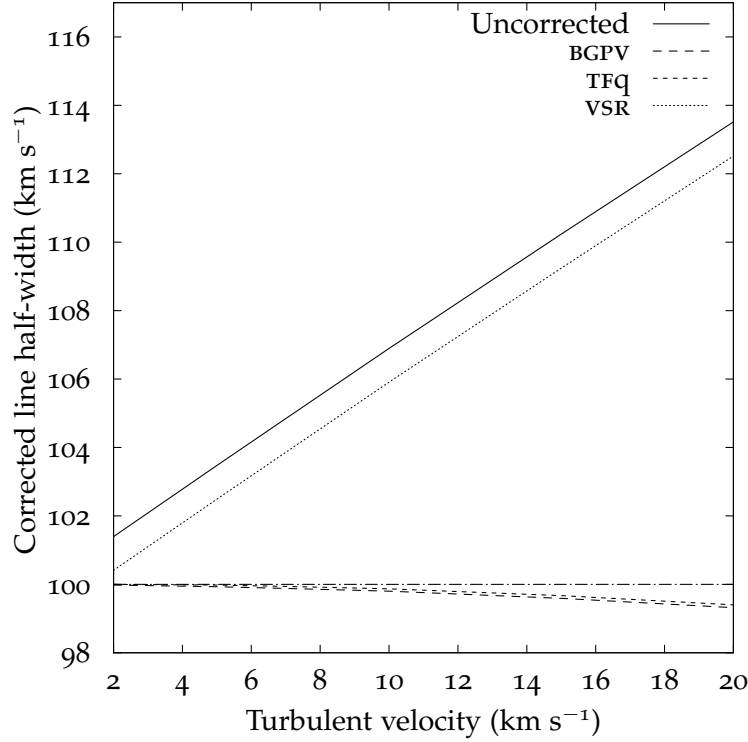
Figure 4.6: The turbulence and inclination corrected line half-widths for the constant circular speed, uniform surface density galaxy as described in section 3.1.1, at 50% of the peak (using W_{50}). The horizontal line shows the value of v_{max} ($v_{max} = 100\,\mathrm{km\,s^{-1}}$).

As expected, VSR's method over-corrects for turbulent velocities less than $\approx 10\,\mathrm{km\,s^{-1}}$. BGPV's and TFq's methods over-correct in general, with the amount of over-correction being very similar. For W_{20}, they over-correct by $\approx 10\,\mathrm{km\,s^{-1}}$ for $\sigma_0 = 20\,\mathrm{km\,s^{-1}}$ and over-correct by $\approx 1\,\mathrm{km\,s^{-1}}$ for $\sigma_0 = 2\,\mathrm{km\,s^{-1}}$. Table 4.1 shows the values of W_{20} and W_{50}, as well as the corrected half-widths determined at 20%

and 50% of the peak using these methods. In general, the deviations from v_{max} are smaller overall for W_{50}.

So far, the inclination angle of the galaxy was fixed at 90°. Now, I will discuss the effect of changing the inclination angle of this galaxy on the various corrections. The inclination angle is varied from 10° to 90° in steps of 10°, and turbulence+inclination-corrected half-widths are calculated for each case at three different values of turbulent velocities: $5\,\mathrm{km\,s^{-1}}$, $10\,\mathrm{km\,s^{-1}}$ and $15\,\mathrm{km\,s^{-1}}$.

The corrected line half-widths, determined from W_{20} using BGPV's method are plotted in Figure 4.7. Their method hugely over-corrects for lower inclinations, the amount of over-correction in the worst case ($i = 10°$, $\sigma_0 = 15\,\mathrm{km\,s^{-1}}$) being as much as $\approx 55\,\mathrm{km\,s^{-1}}$.

Using TFq's method to correct for turbulence motions gives better results. As mentioned in section 1.7.2, their method improves on the method proposed by BGPV in that it uses quadrature subtraction for smaller velocity widths. As the galaxy becomes more face-on (smaller i), the uncorrected line-width becomes smaller, and TFq's method does quadrature subtraction in those cases. For the simple galaxy, this results in significant improvement in the corrected line widths. Figure 4.8 shows the results of applying their correction on this galaxy for W_{20}.

TFq's method works particularly well for inclinations as low as $\approx 25°$, failing only at extreme face-angles. Even then, the method over-corrects for most inclinations, the amount of over-correction is

σ_0	W_{20}	W_{50}	v_{max} (BGPV)		v_{max} (TFq)		v_{max} (VSR)	
			20%	50%	20%	50%	20%	50%
km s^{-1}	km s^{-1}	km s^{-1}	km s^{-1}	km s^{-1}	km s^{-1}	km s^{-1}	km s^{-1}	km s^{-1}
2	205.6	202.8	99.0	100.0	99.2	100.0	92.4	100.4
5	213.9	207.0	97.5	100.0	97.9	100.0	96.4	102.5
7	219.5	209.7	96.5	100.0	97.0	100.0	99.1	103.9
10	227.7	213.8	94.9	100.0	95.5	100.0	103.1	105.9
15	241.5	220.5	92.4	100.0	92.9	100.0	109.9	109.2
20	255.0	227.0	89.7	99.3	90.1	99.4	116.6	112.5

Table 4.1: Turbulence corrected line half-widths for the constant circular speed, uniform surface density galaxy, as determined by various algorithms described in the text. The half-widths are presented at 20% and 50% of the peak.
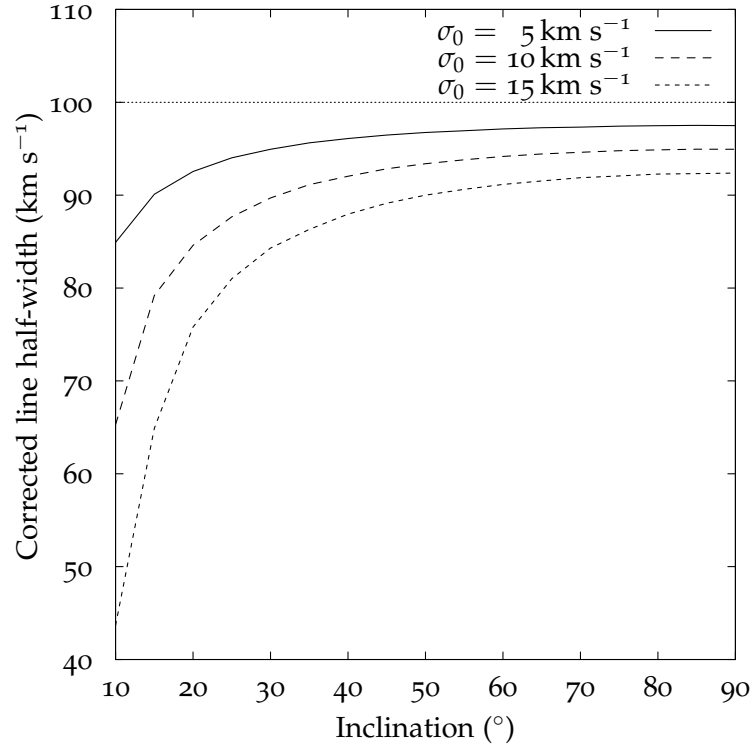
Figure 4.7: The turbulence and inclination corrected line half-widths as a function of inclination angle for the constant circular speed, uniform density galaxy, as described in section 3.1.1, at 20% of the peak, using BGPV's method. The horizontal line shows the value of v_{max} ($v_{max} = 100\,\mathrm{km\,s^{-1}}$). This method over-corrects for random motions, particularly at low inclinations.
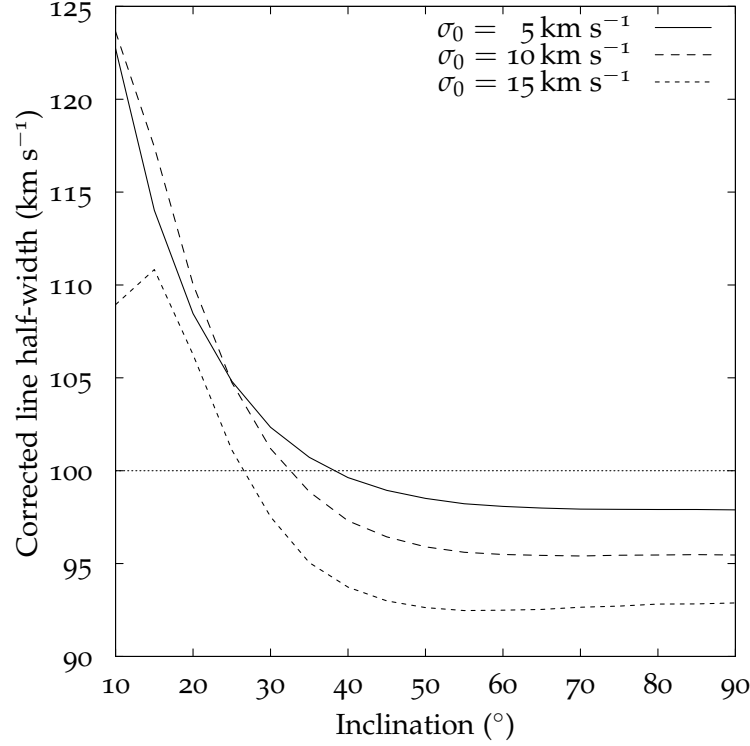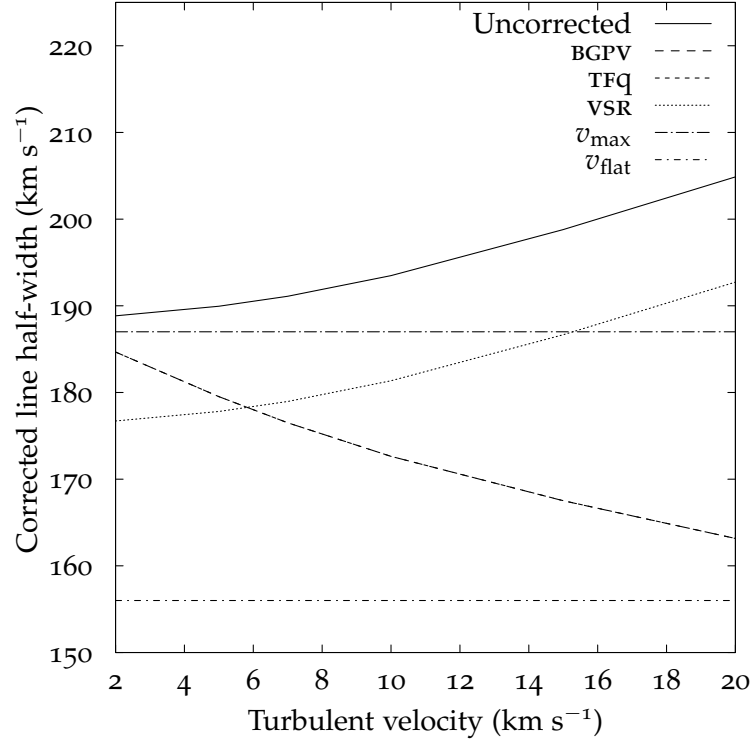
Figure 4.8: The turbulence and inclination corrected line half-widths as a function of inclination angle for the constant circular speed, uniform surface density galaxy as described in section 3.1.1, at 20% of the peak, using TFq's method. The horizontal line shows the value of v_{max} ($v_{max} = 100\,\mathrm{km\,s^{-1}}$). This method is a significant improvement over BGPV's method, particularly for lower inclinations.

as large as $7\,\mathrm{km\,s^{-1}}$ for random motions of $15\,\mathrm{km\,s^{-1}}$. The results for W_{50} are similar.

Finally, Figure 4.9 shows the results of applying VSR's corrections. Also, Figure 4.10 shows the results from VSR using widths at 50%. Their method in general under-corrects for turbulence, except for low turbulent motions ($\sigma_0 = 5\,\mathrm{km\,s^{-1}}$), and using W_{20}, where it over-corrects a bit for most inclinations.
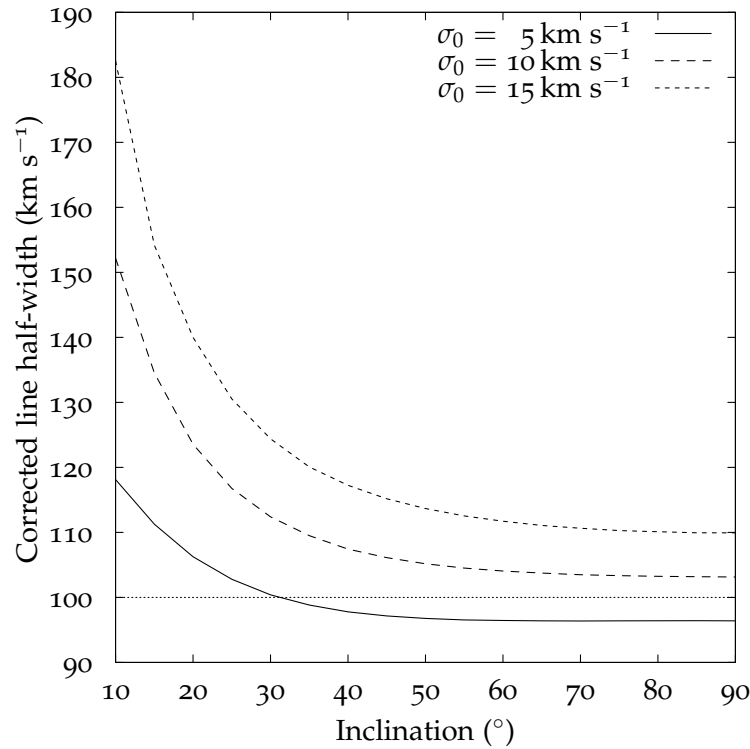
Figure 4.9: The turbulence and inclination corrected line half-widths as a function of inclination angle for the constant circular speed, uniform density galaxy as described in section 3.1.1, at 20% of the peak, using VSR's method. The horizontal line shows the value of v_{max} ($v_{\mathrm{max}} = 100\,\mathrm{km\,s^{-1}}$).
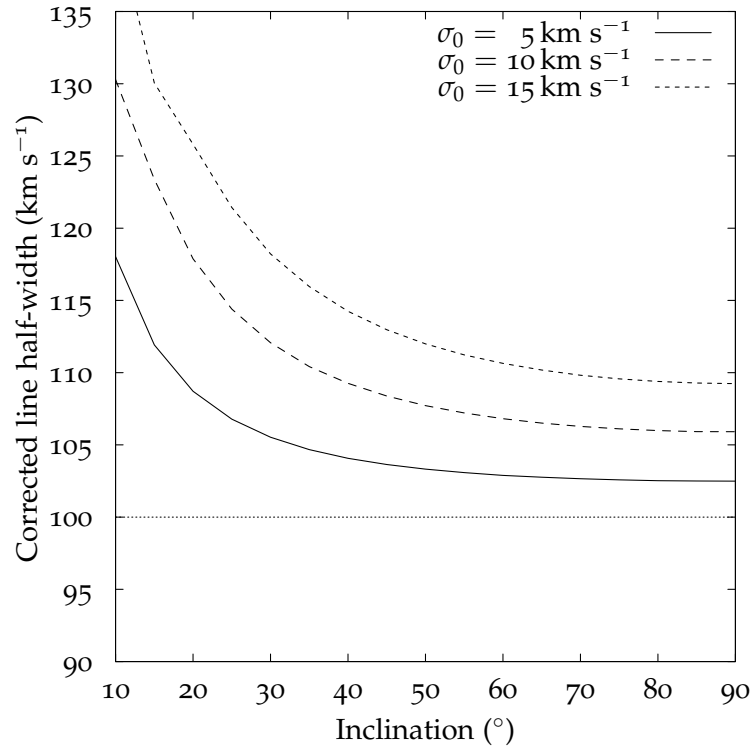
Figure 4.10: The turbulence and inclination corrected line half-widths as a function of inclination angle for the constant circular speed, uniform surface density galaxy as described in section 3.1.1, at 50% of the peak, using VSR's method. The horizontal line shows the value of v_{max} ($v_{max} = 100 \, \text{km s}^{-1}$).

4.2.2   NGC *4088*

For a description of parameters used to model NGC 4088, see section 3.3.2. For this section, as mentioned in that section, the inclination angle used is 65°.

Figures 4.11 and 4.12 show the results of applying the turbulence motion corrections as a function of turbulence motions in NGC 4088. For comparison, and to estimate the amount of corrections applied in each case, the uncorrected line half-widths are also plotted in the figures. The 'uncorrected' line half-widths in these and subsequent figures are still corrected for inclination (dividing the uncorrected line widths by $2 \sin i$) to allow for realistic comparisons of the amount of correction applied by each method.

TFQ's and BGPV's methods reduce to the same in this galaxy, because $W_l \gg W_{c,l}$ in this case. For W_{20}, these methods over-correct for random motions if $v_{\max}$ is considered. The corrected line widths stay within the range v_{flat}–$v_{\max}$. VSR's method tends to work well only for $\sigma_0 \approx 15\,\mathrm{km\ s^{-1}}$, and it over-corrects for smaller values of σ_0. The results for W_{50} are similar.

As in the case of the simple galaxy, the next step is to study the effect of changing the galaxy's inclination angle on the turbulence-corrected line widths. For this purpose, as before, the inclination angle was varied from 10° to 90° in steps of 10°. The turbulent velocities were chosen to be $5\,\mathrm{km\ s^{-1}}$, $10\,\mathrm{km\ s^{-1}}$ and $15\,\mathrm{km\ s^{-1}}$.

Figure 4.11: The turbulence and inclination corrected line half-widths for NGC 4088 at 20% of the peak (using W_{20}). The horizontal lines show the value of $v_{\max}$ (187 km s^{-1}) and v_{flat} (156 km s^{-1}). The corrections due to TFq and BGPV are same for this galaxy, because the uncorrected line width for in this case is high ($W_l \gg W_{c,l}$ in equation 1.23). The 'uncorrected' line half-width is corrected for inclination.
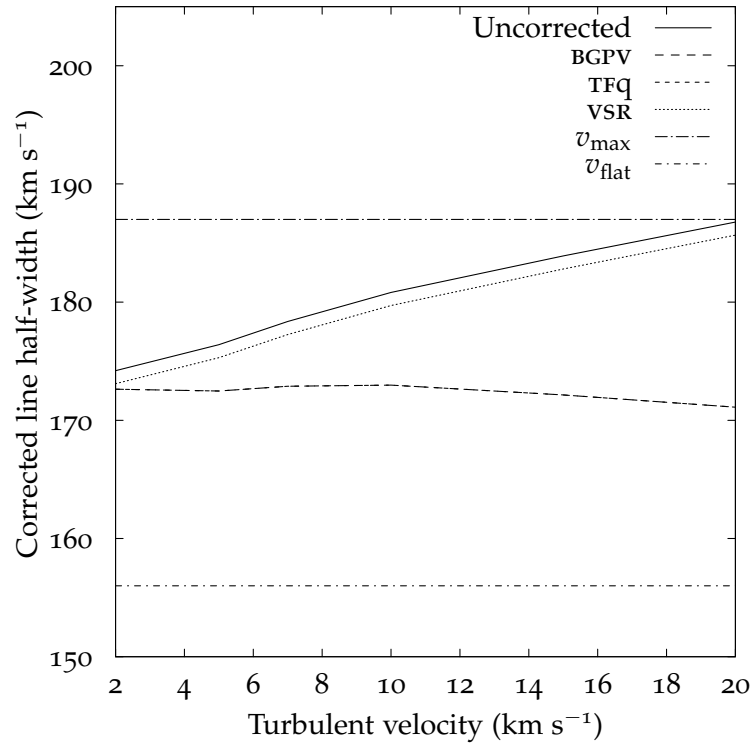
Figure 4.12: The turbulence and inclination corrected line half-widths for NGC 4088 at 50% of the peak (using W_{20}). The horizontal lines show the value of v_{max} (187 km s^{-1}) and v_{flat} (156 km s^{-1}). The 'uncorrected' line half-width is corrected for inclination.

Figure 4.13 shows the results of applying BGPV's corrections on NGC 4088 using W_{20}. As before, the method works moderately well for high inclinations (close to edge-on) and for low turbulent velocities. At lower inclinations ($i < 40°$), however, the method shows serious deviations from v_{max} and v_{flat}. The case for $\sigma_0 = 15\,\text{km s}^{-1}$ results in a deviation of at least $16\,\text{km s}^{-1}$, so even in the best-case scenario, their method over-corrects by $16\,\text{km s}^{-1}$ for $\sigma_0 = 15\,\text{km s}^{-1}$.
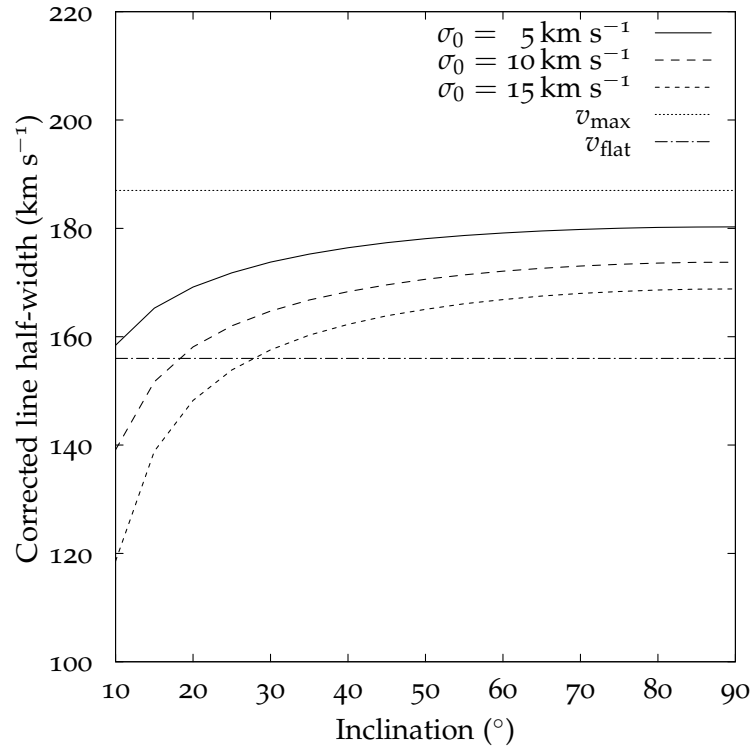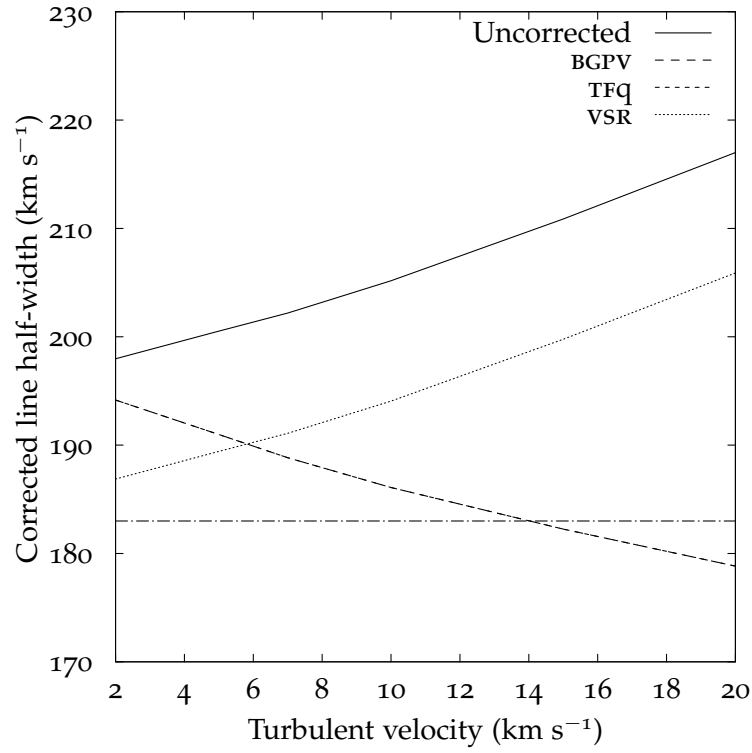

Figure 4.13: The turbulence and inclination corrected line half-widths as a function of inclination angle for the NGC 4088 as described in section 3.3.2, at 20% of the peak, using BGPV's method. The horizontal lines shows the values of v_{max} ($187\,\text{km s}^{-1}$) and v_{flat} ($156\,\text{km s}^{-1}$). This method over-corrects for random motions, particularly at low inclinations.

Figure 4.14 shows the result of applying turbulence motion corrections as defined by TFq on NGC 4088. Their method is better at turbulent motion corrections, resulting in a corrected half-width that stays between v_{max} and v_{flat} for most inclinations. As expected, for higher inclinations, their method is very similar to BGPV's method, but it works much better for low inclinations. As in the case of BGPV's method, the method over-corrects for most inclinations, the amount of minimum over-correction for $\sigma_0 = 15\,\text{km s}^{-1}$ being $\approx 20\,\text{km s}^{-1}$.
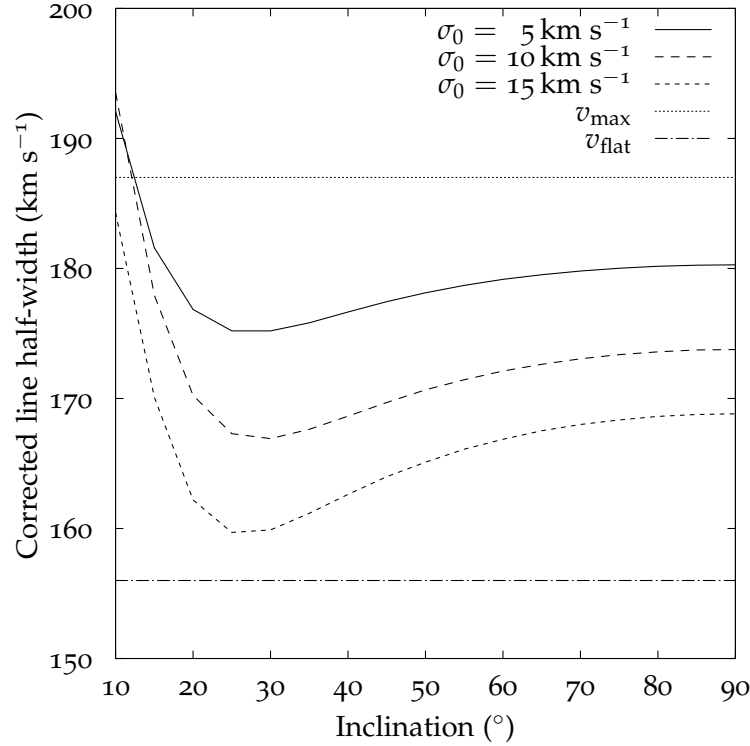
Figure 4.14: The turbulence and inclination corrected line half-widths as a function of inclination angle for the NGC 4088 as described in section 3.3.2, at 20% of the peak, using TFq's method. The horizontal lines shows the values of v_{max} ($187\,\text{km s}^{-1}$) and v_{flat} ($156\,\text{km s}^{-1}$). Note that the vertical scale in this figure is different from the one in figure 4.13.

Figure 4.15 shows the results of applying VSR's corrections. This method also over-corrects for most inclinations, but hugely under-corrects for lower inclinations. The amount of over-corrections is smaller than that from BGPV and TFq cases though, being $\lesssim 10\,\text{km s}^{-1}$ for inclinations $\gtrsim 45°$.
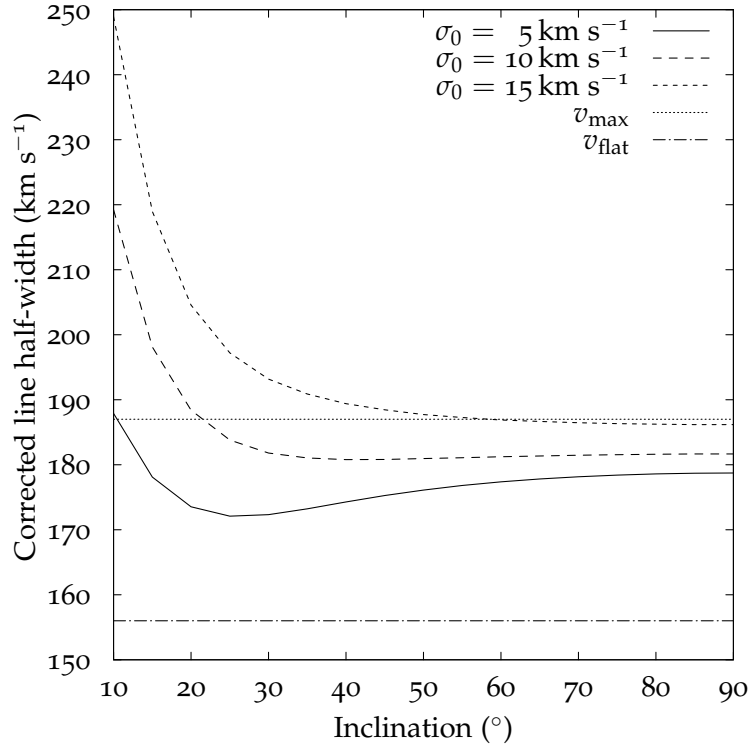
Figure 4.15: The turbulence and inclination corrected line half-widths as a function of inclination angle for the NGC 4088 as described in section 3.3.2, at 20% of the peak, using VSR's method. The horizontal lines shows the values of v_{max} (187 km s^{-1}) and v_{flat} (156 km s^{-1}).

Finally, Figure 4.16 shows the result of applying VSR's correction for W_{50}. Again, their method stays closer to v_{max}, but still shows deviations as large as $\approx 10\,\text{km s}^{-1}$ for higher inclinations.
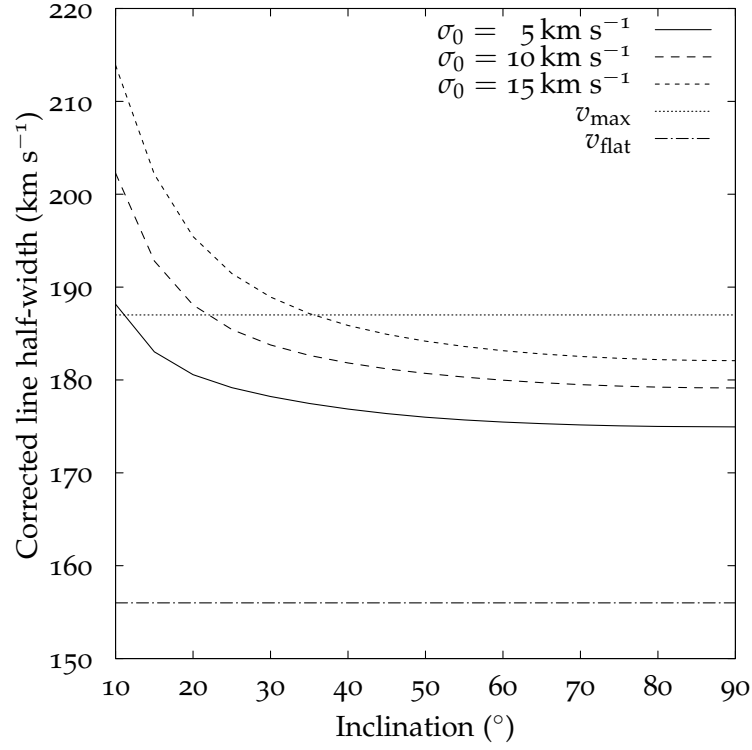
Figure 4.16: The turbulence and inclination corrected line half-widths as a function of inclination angle for the NGC 4088 as described in section 3.3.2, at 50% of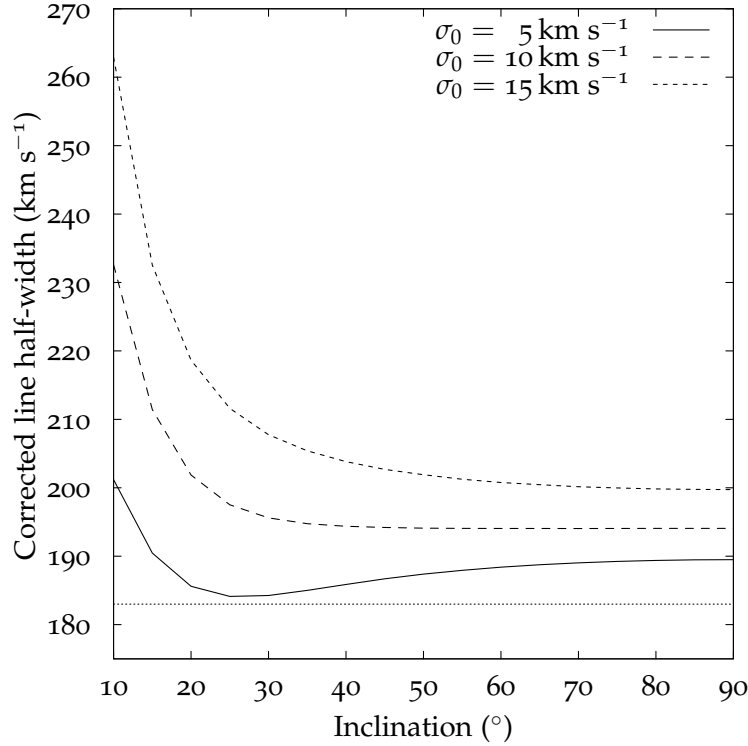 the peak, using VSR's method. The horizontal lines shows the values of v_{max} (187 km s^{-1}) and v_{flat} (156 km s^{-1}).

4.2.3   NGC *4157*

For comparison of various methods of turbulence correction, and their effectiveness, I discuss the galaxy NGC 4157. The galaxy parameters are described in table 3.8 in section 3.3.5. As for NGC 4088, first, I discuss the turbulence correction methods at the observed inclination angle of the galaxy, 82°. Then, I discuss the effect changing the galaxy inclination on these methods.

This galaxy has a rotation curve that flattens out for large r. The values of v_{max} and v_{flat} are almost equal, so this galaxy serves as a good candidate for comparison of turbulence correction by various methods, particularly in order to study the effectiveness of the method proposed by VSR. The galaxy v_{max} and v_{flat} values are $\approx 183\,\text{km s}^{-1}$.

Figures 4.17 and 4.18 show the results of applying the turbulence corrections at 20% and 50% of the peak H1 flux. As for NGC 4088, the 'uncorrected' line half-widths, derived by applying inclination correction on the uncorrected line widths are also shown. From Figure 4.17, VSR's method consistently under-corrects for random motions, even for really small values of σ_0. As before, BGPV's and TFQ's methods are the same for this galaxy at its adopted value of inclination, because the uncorrected line width for this galaxy is also very high. These two methods are better at correcting for random motions, but they work the best for $\sigma_0 \approx 15\,\text{km s}^{-1}$.

Figure 4.17: The turbulence and inclination corrected line half-widths for NGC 4157 at 20% of the peak (using W_{20}). The horizontal line shows the value of v_{max} and v_{flat} (183 km s^{-1}). The 'uncorrected' line half-width is corrected for inclination.

Similarly, from Figure 4.18, vsr's method still under-corrects (W_{50}) for all values of random motions, while bgpv's and tfq's methods are better. They still under-correct, however, the amount of under-correction being $\approx 3\,\mathrm{km\,s^{-1}}$.
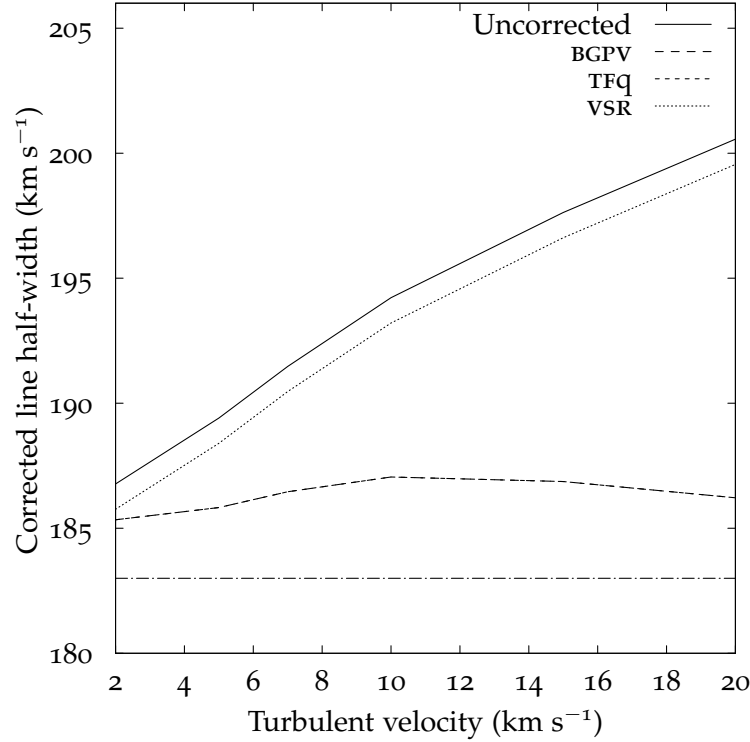
Figure 4.18: The turbulence and inclination corrected line half-widths for NGC 4157 at 50% of the peak (using W_{20}). The horizontal line shows the value of v_{max} and v_{flat} (183 km s^{-1}). The 'uncorrected' line half-width is corrected for inclination.

Figure 4.19 shows the results of applying bgpv's corrections on NGC 4157 using W_{20}. As before, the method works well for high inclinations (close to edge-on) and for low turbulent velocities, but even then, the amount of offset is as large as $\approx 10\,\mathrm{km\,s^{-1}}$. For lower inclinations and/or higher turbulent velocities, their method breaks

down. For $\sigma_0 = 5\,\text{km s}^{-1}$, the best correction by this method is at $i = 90°$, which is still $\approx 10\,\text{km s}^{-1}$ more than needed.
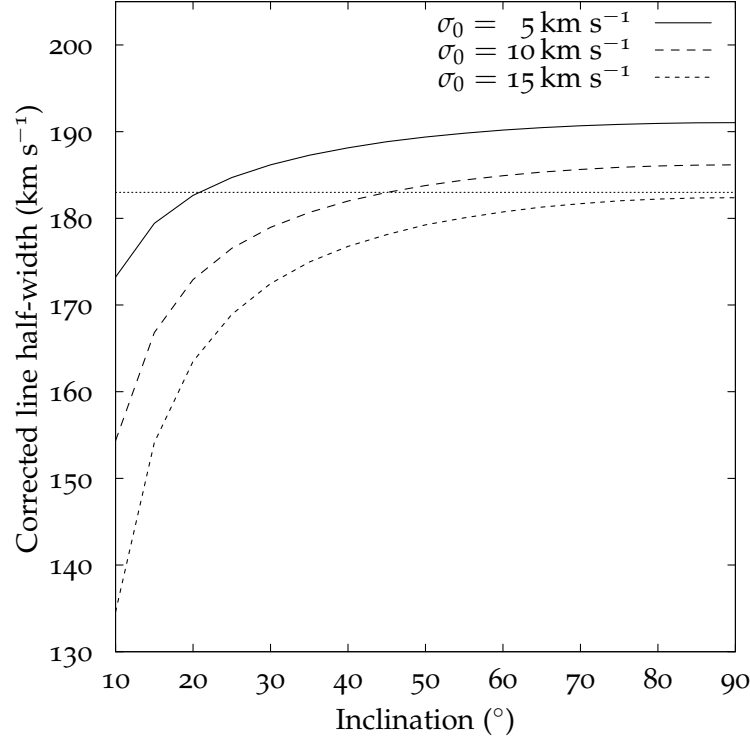
Figure 4.19: The turbulence and inclination corrected line half-widths as a function of inclination angle for the NGC 4157 as described in section 3.3.5, at 20% of the peak, using BGPV's method. The horizontal line shows the value of v_{max} and v_{flat} (183 km s^{-1}). This method over-corrects for random motions, particularly at low inclinations.

Figure 4.20 shows the result of applying turbulence motion corrections as defined by TFq on NGC 4157. Their method is better at correcting higher turbulence motions, but for low turbulence, their method consistently under-corrects, by as much as $\approx 10\,\text{km s}^{-1}$ for $\sigma_0 = 5\,\text{km s}^{-1}$ and $i = 90°$.
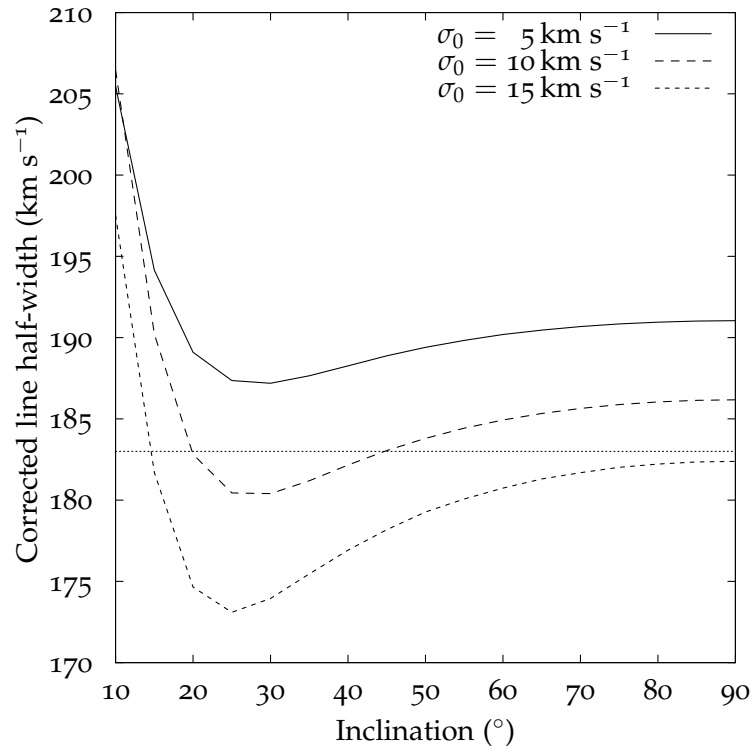
Figure 4.20: The turbulence and inclination corrected line half-widths as a function of inclination angle for the NGC 4157 as described in section 3.3.5, at 20% of the peak, using TFq's method. The horizontal line shows the value of v_{max} and v_{flat} ($183\,\mathrm{km\,s^{-1}}$).

Figure 4.21 shows the results of applying VSR's corrections. Their method consistently under-corrects for random motions, at all inclinations. Even for higher values of inclinations, the best-case scenario for $\sigma_0 = 15\,\mathrm{km\,s^{-1}}$ under corrects by as much as $\approx 17\,\mathrm{km\,s^{-1}}$.

Figure 4.21: The turbulence and inclination corrected line half-widths as a function of inclination angle for the NGC 4157 as described in section 3.3.5, at 20% of the peak, using VSR's method. The horizontal line shows the value of v_{max} and v_{flat} ($183\,\mathrm{km\,s^{-1}}$).

For W_{50}, VSR's method does poorly at all turbulence velocities. The best case scenario occurs at low turbulence velocities and high inclinations ($\sigma_0 = 5\,\mathrm{km\,s^{-1}}$ and $i = 90°$), for which this method under-corrects by $\approx 4\,\mathrm{km\,s^{-1}}$. For turbulence of $15\,\mathrm{km\,s^{-1}}$, the lowest amount of under-correction is $\approx 13\,\mathrm{km\,s^{-1}}$.
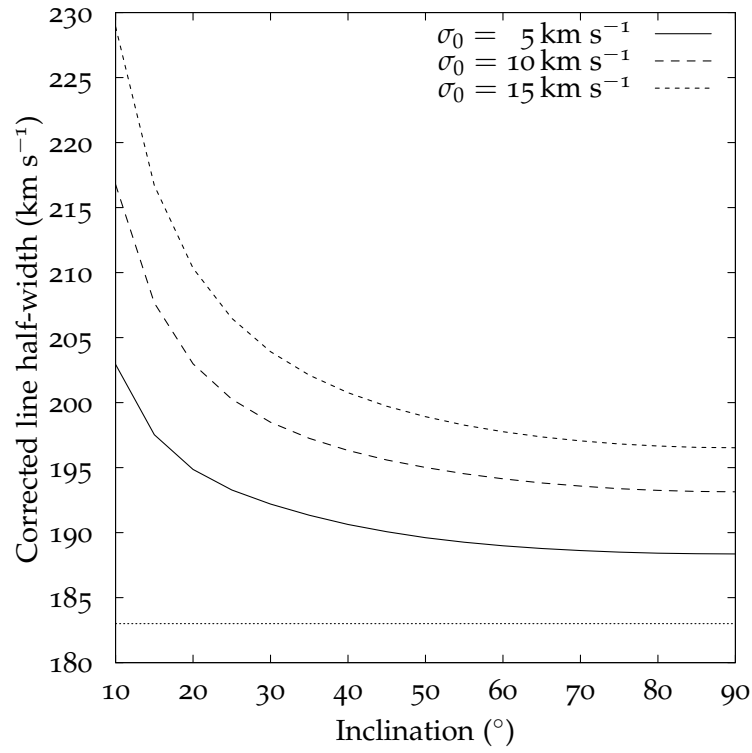
Figure 4.22: The turbulence and inclination corrected line half-widths as a function of inclination angle for the NGC 4157 as described in section 3.3.5, at 50% of the peak, using VSR's method. The horizontal lines shows the values of v_{max} and v_{flat} (183 km s^{-1}).

4.2.4   UGC *6930*

UGC 6930 has the slowest rotation curve of all the galaxies modeled in chapter 3, and it is also the least inclined galaxy of the sample ($i = 30°$). Therefore, for the last example of comparison between various corrections, this galaxy is ideal. In particular, the turbulence corrections as applied by TFq and BGPV should be different for this galaxy, because TFq's method should perform a quadrature subtraction in this case as opposed to reducing to linear subtraction for the previous two galaxies.

The galaxy rotation curve (figure 3.28) starts flattening out only at large values of r. The rotation curve has a maximum value of $v_{\max} = 110 \, \text{km s}^{-1}$, and $v_{\max} = v_{\text{flat}}$ for this galaxy.

Figures 4.23 and 4.24 show the results of applying the turbulence corrections at 20% and 50% of the peak HI flux. The corrections due to BGPV and TFq are different for this galaxy, as expected, with TFq's method working better at all values of turbulent velocities. VSR's method is worse than TFq's method for most turbulent motions, giving better results only in the region around $\sigma_0 \approx 6 \, \text{km s}^{-1}$.

Similarly, for W_{50}, TFq's method is the most accurate for all values of turbulent velocities, with VSR's method doing marginally better only at really low turbulent motions ($\sigma_0 \approx 4 \, \text{km s}^{-1}$).

In both the cases (W_{20} and W_{50}), the best corrections due to turbulent motions are way too large at all turbulent motions.
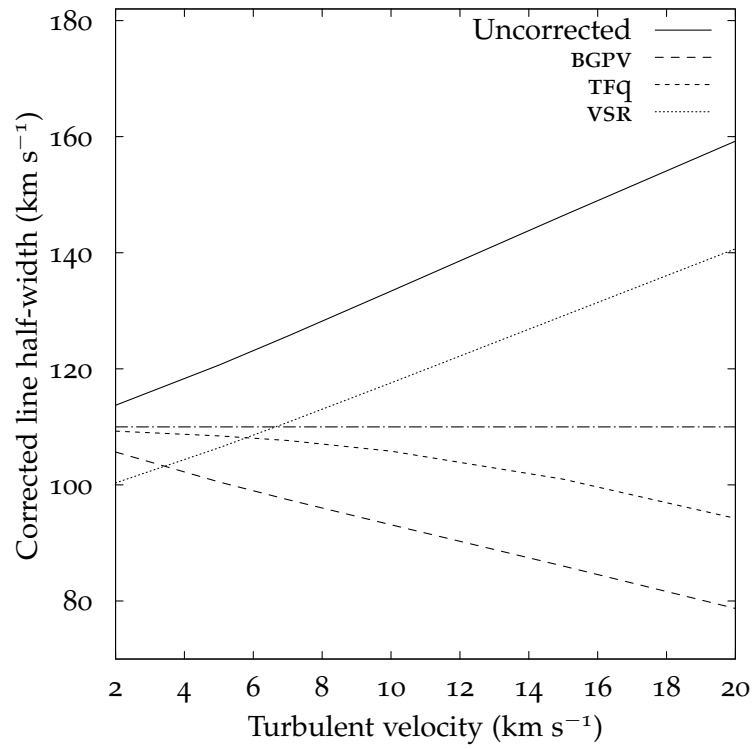
Figure 4.23: The turbulence and inclination corrected line half-widths for ᴜɢᴄ 6930 at 20% of the peak (using W_{20}). The horizontal line shows the value of v_{max} and v_{flat} (110 km s^{-1}). The 'uncorrected' line half-width is corrected for inclination.
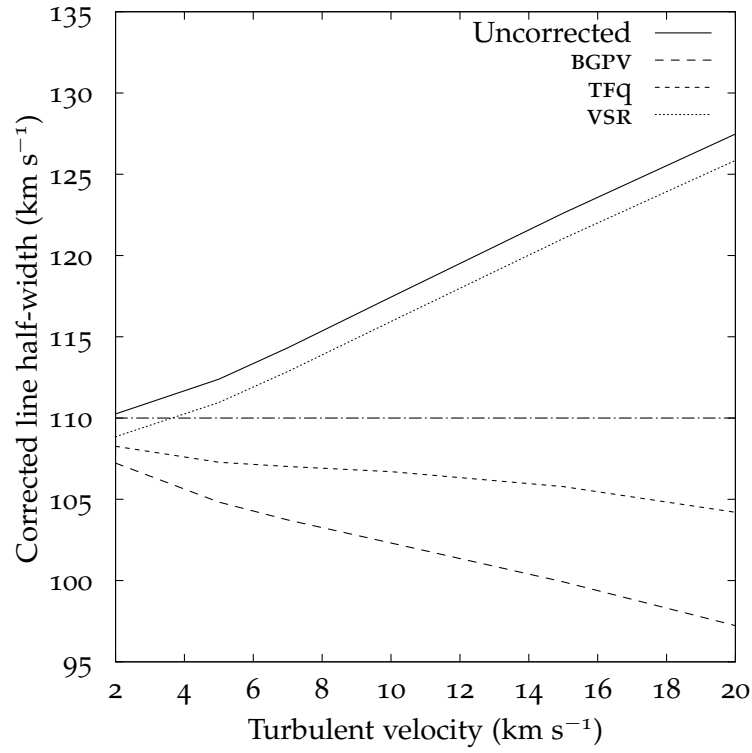
Figure 4.24: The turbulence and inclination corrected line half-widths for UGC 6930 at 50% of the peak (using W_{20}). The horizontal line shows the value of v_{max} and v_{flat} (110 km s^{-1}). The 'uncorrected' line half-width is corrected for inclination.

Figure 4.25 shows the results of applying BGPV's corrections on UGC 6930 using W_{20}. Their method consistently over-corrects for random motions at all inclinations, with the amount of over-correction being particularly large at low inclinations. This means that their method of turbulence correction biases the corrected line widths of such galaxies to be much lower than they should be.
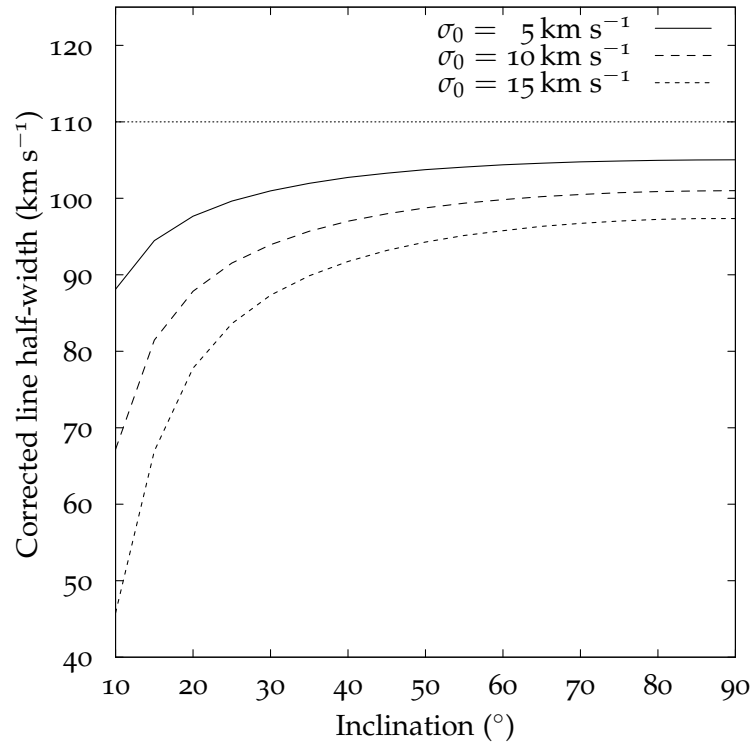
Figure 4.25: The turbulence and inclination corrected line half-widths as a function of inclination angle for the UGC 6930 as described in section 3.3.7, at 20% of the peak, using BGPV's method. The horizontal line shows the value of v_{max} and v_{flat} ($110\,\mathrm{km\,s^{-1}}$). This method over-corrects for random motions, particularly at low inclinations.

Figure 4.26 shows the result of applying turbulence motion corrections as defined by TFQ on UGC 6930. Their method is off by as much

as 10% for $i = 90°$ and $\sigma_0 = 10\,\text{km s}^{-1}$. As expected, their method is much better at turbulence correction at lower inclinations compared to BGPV's method.
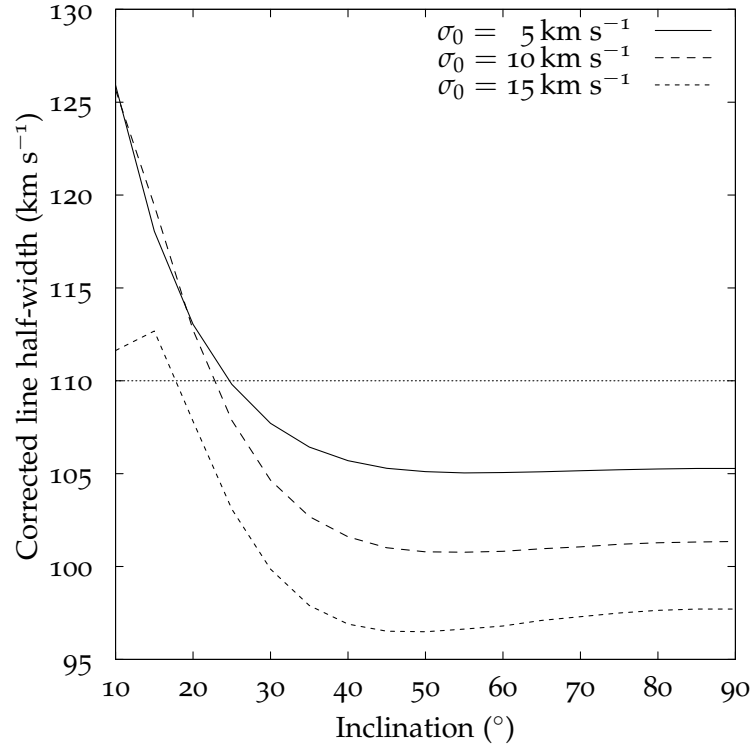
Figure 4.26: The turbulence and inclination corrected line half-widths as a function of inclination angle for the UGC 6930 as described in section 3.3.7, at 20% of the peak, using TFq's method. The horizontal line shows the value of v_{max} and v_{flat} (110 km s^{-1}).

Figure 4.27 shows the results of applying VSR's corrections using W_{20} as a function of inclination. Their method works best with turbulent motions around 10 km s^{-1}, but under-corrects at lower inclinations. In particular, the amount of under-correction is as large as $\approx 20\%$ for inclinations around 30°.
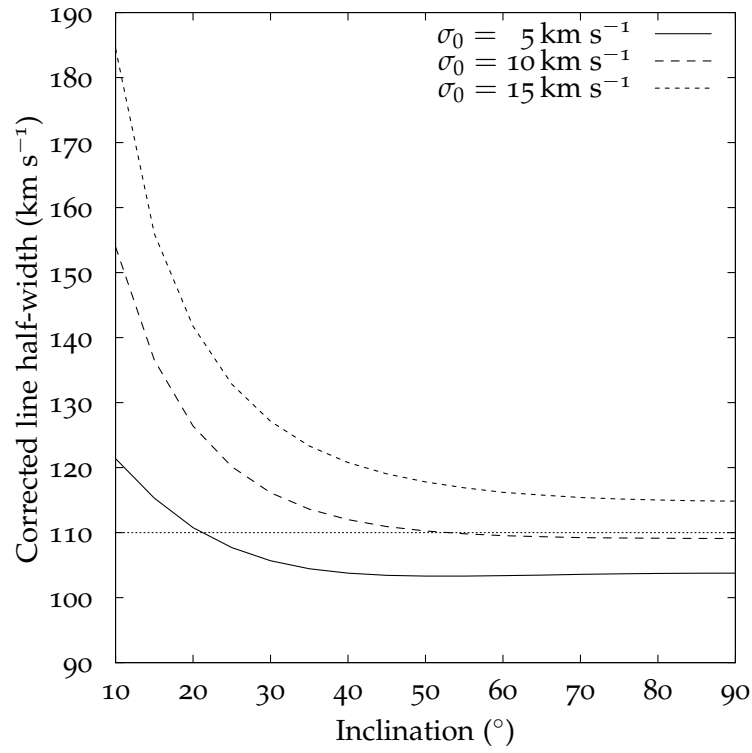
Figure 4.27: The turbulence and inclination corrected line half-widths as a function of inclination angle for the UGC 6930 as described in section 3.3.7, at 20% of the peak, using VSR's method. The horizontal line shows the value of v_{max} and v_{flat} (110 km s^{-1}).

Figure 4.28 shows the results of applying vsr's corrections using W_{50}. At W_{50}, their method consistently under-corrects for turbulence, except for really small values of random motions and high inclinations.
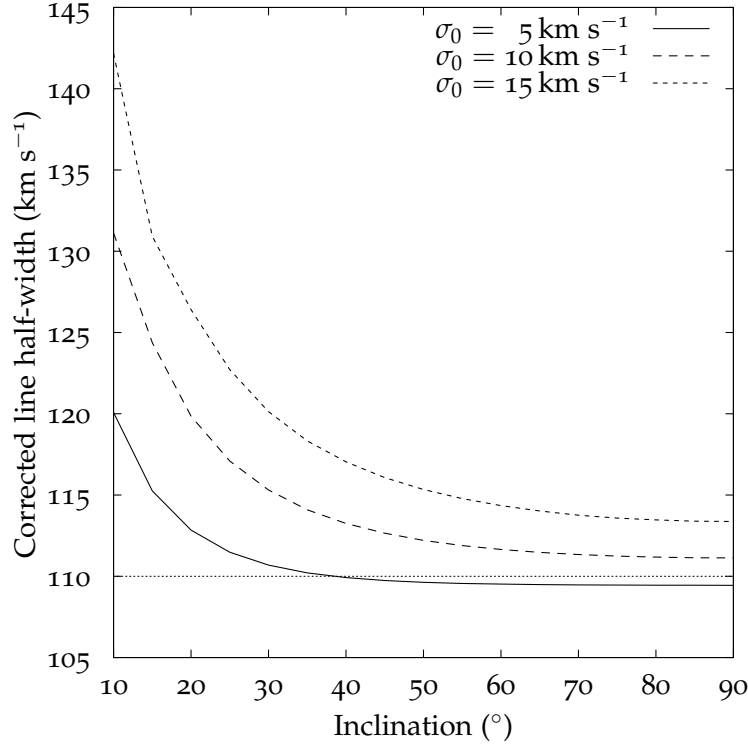
Figure 4.28: The turbulence and inclination corrected line half-widths as a function of inclination angle for the ugc 6930 as described in section 3.3.7, at 50% of the peak, using vsr's method. The horizontal lines shows the values of v_{max} and v_{flat} ($110\,km\,s^{-1}$).

4.2.5   *Effects of turbulent motion corrections alone*

By looking at the results for the galaxies in the previous sections, it is clear that the turbulent motion corrections either over- or under-

correct for most inclinations and most turbulent velocities. BGPV's method always over-corrects for the random motions. This is mainly because of their use of $k(l)$, which is higher than the half-width of a Gaussian (with dispersion 1) at $l\%$ of its peak. TFQ's method also over-corrects for random motions at all inclinations and all turbulent velocities. Their method is a significant improvement over the method proposed by BGPV, but the amount of over-correction is still way too large, being $\approx 10\%$ in most cases.

VSR's method, in general, does not work well for most cases, giving good results only with specific combinations of inclinations and turbulent motions. This is expected for two reasons. First, their method of turbulent motion correction should be applied after their method of instrumental resolution correction is applied. If their method of instrumental resolution correction is inefficient in the sense that it does not fully correct for line profile broadening due to instrumental resolution, then their method of turbulence correction will be inaccurate for zero turbulence case. Second, their method of turbulence correction is based on data for real galaxies, where $\sigma_0 \approx 10\,\mathrm{km\,s^{-1}}$, so the method is expected to work only for turbulent velocities at around $10\,\mathrm{km\,s^{-1}}$.

Therefore, in the next few sections, I study the effect of applying instrumental and turbulence corrections as proposed by VSR on line profiles created by the model with finite instrumental resolution and a range of turbulent velocities and inclination angles.

4.3 INSTRUMENTAL RESOLUTION CORRECTION

Based upon the results from the above two galaxies, and also from the simple galaxy, it can be seen that all the currently used methods of turbulent motion correction have quite significant errors in most circumstances. They sometimes work for specific cases of turbulent motions and inclination angles, but are hard to generalize. The above examples assumed that the instrumental resolution, R is zero. In this section, I discuss the effect of a finite instrumental resolution on the method of turbulence and instrumental resolution correction as proposed by VSR on the above two galaxies. Since BGPV and TFq did not discuss the effects of instrumental resolution on HI line profiles, they cannot be used in to do a comparison as was done for turbulence motion correction. Bottinelli et al. (1990) defined a method of instrumental resolution correction, but their method is very similar to that used by VSR, so I have not used that method below. Also, in order to conserve space, only the line widths at 20% of the peak (W_{20}) is used. The results for W_{50} are similar. The observations are simulated with an instrumental resolution of their actual observations.

The method proposed by VSR is described in section 1.7.3. In this method, first the instrumental correction δW_{20} as defined in equation 1.30 is subtracted from the observed line width, W_{20}. Then, the turbulence motion correction of equation 1.24 is applied. Finally, the inclination correction defined in equation 1.12 is applied, and the

result is divided by 2 to obtain the corrected half-width that can be compared with v_{max} and v_{flat}.

Ideally, the line widths after subtracting δW_{20} from the observed line width should be the same as the line widths in the case of zero instrumental resolution. As seen below, this is not the case. The reason for this discrepancy is that the calculation of δW_{20} assumes the galaxy line profile wings to be Gaussian. This would be true only for extremely large values of turbulent motions, and/or when the observed line profile itself is close to a Gaussian. For most 'regular' galaxies, this is not the case. For such galaxies, the instrumental correction as defined by vsr is too low.

4.3.1   NGC *4088*

After modeling the galaxy at the observed instrumental resolution, and at various values of turbulent velocities, the instrumental resolution corrected line profile width is calculated. These calculated widths are then plotted against the corresponding widths with zero instrumental resolution. The results for W_{20} and W_{50} are shown in Figure 4.29. As expected, the difference between the instrumental resolution corrected widths and widths with zero instrumental resolution approaches zero for high turbulence motions. Also, the instrumental resolution correction as defined by vsr, and shown

in equation 1.30 does not completely correct for the instrumental resolution broadening for this galaxy.
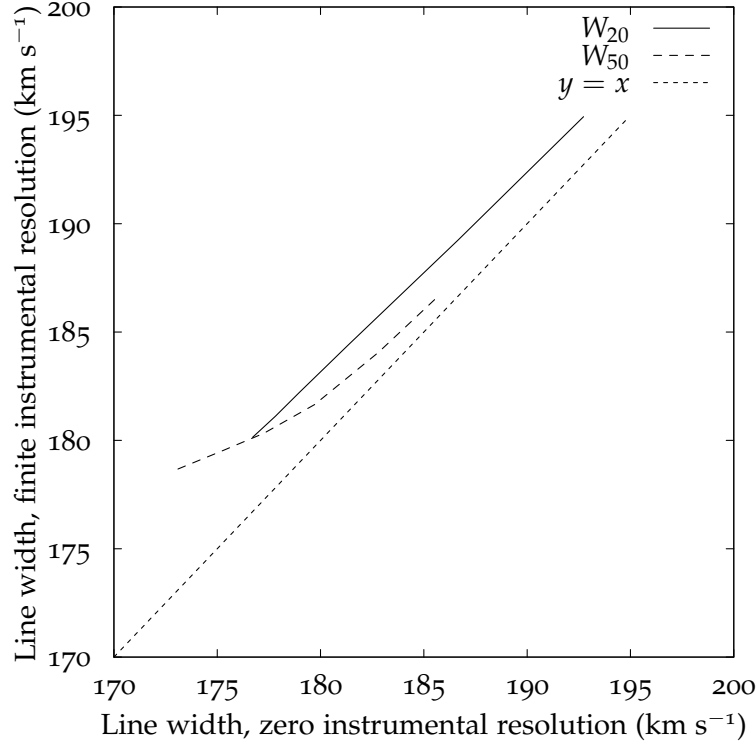
Figure 4.29: Instrumental resolution corrected line widths (W_{20} and W_{50}) vs. zero instrumental resolution line widths for NGC 4088. If the instrumental resolution correction is perfect, then the two lines should lie on $y = x$, also plotted in the figure. The line widths are corrected for instrumental resolution effects as proposed by VSR.

Figure 4.30 shows the instrumental resolution, turbulence, and inclination corrected line widths (using W_{20}) for NGC 4088 for various values of turbulent velocities and inclinations. Figure 4.31 shows the same data, but for W_{50}.

In both the figures, the corrections half-widths are closer to v_{max} than in Figures 4.15 and 4.16. In particular, for $\sigma_0 = 10\,\mathrm{km\,s^{-1}}$, the
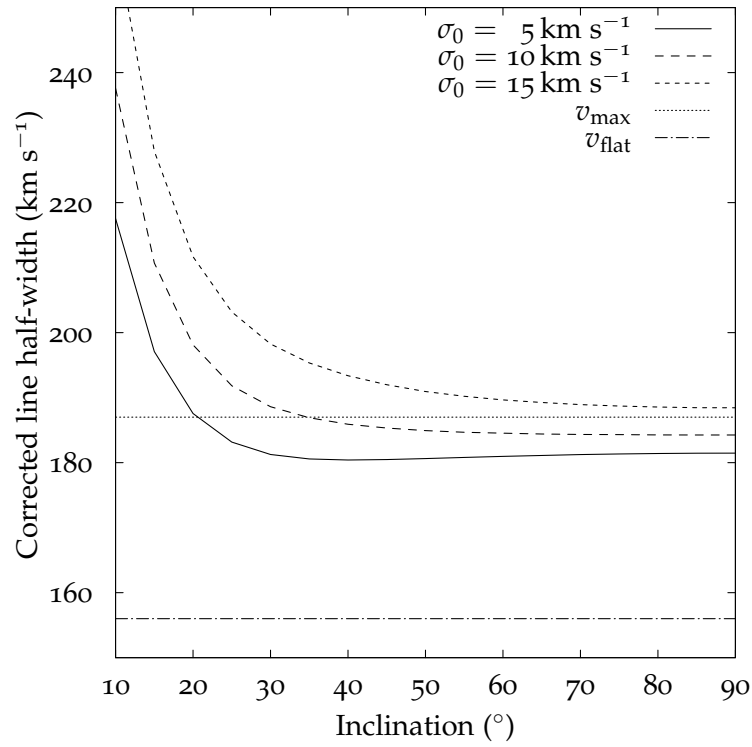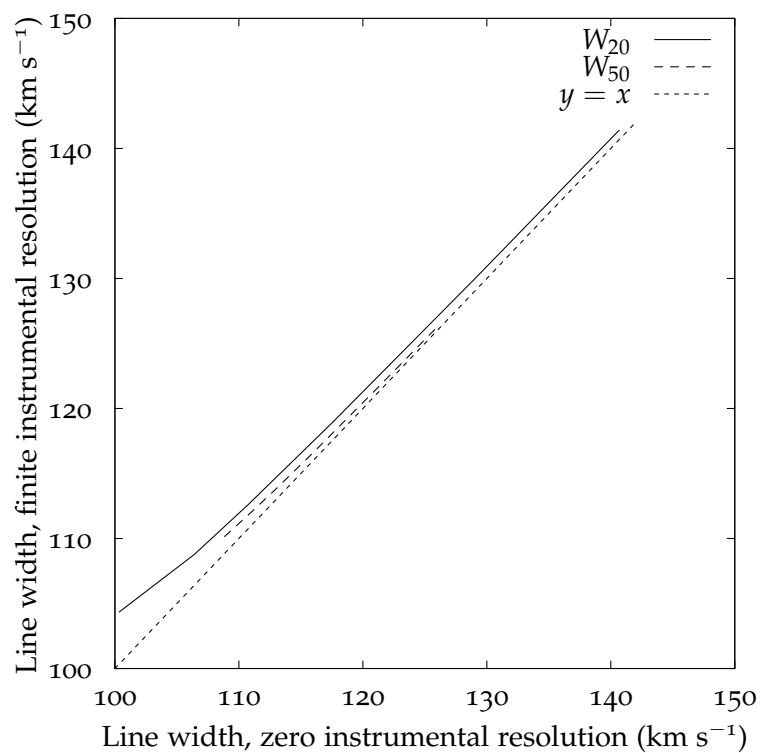
Figure 4.30: The corrected line half-widths for NGC 4088 (as defined by VSR) as a function of inclination for three values of turbulent motions, using W_{20}. The instrumental resolution is finite in this case, and instrumental resolution correction was applied first before applying the other corrections.

corrected line half-widths are much closer to v_{max} in the case of finite instrumental resolution. This is most likely due to offsetting of errors.
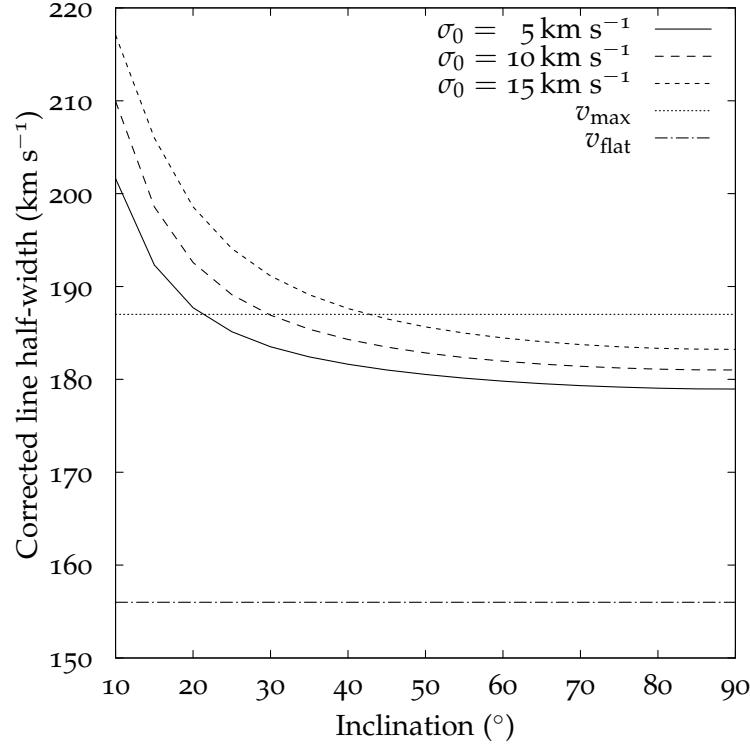
Figure 4.31: The corrected line half-widths (as defined by VSR) as a function of inclination (NGC 4088) for three values of turbulent motions, using W_{50}. The instrumental resolution is finite in this case, and instrumental resolution correction was applied first before applying the other corrections.

4.3.2 NGC 4157

Figure 4.32 shows the plot of instrumental resolution corrected line widths as a function of the line widths with zero instrumental res-

olution. As in Figure 4.29, the two widths are different, and the differences decrease with increasing turbulent velocities.
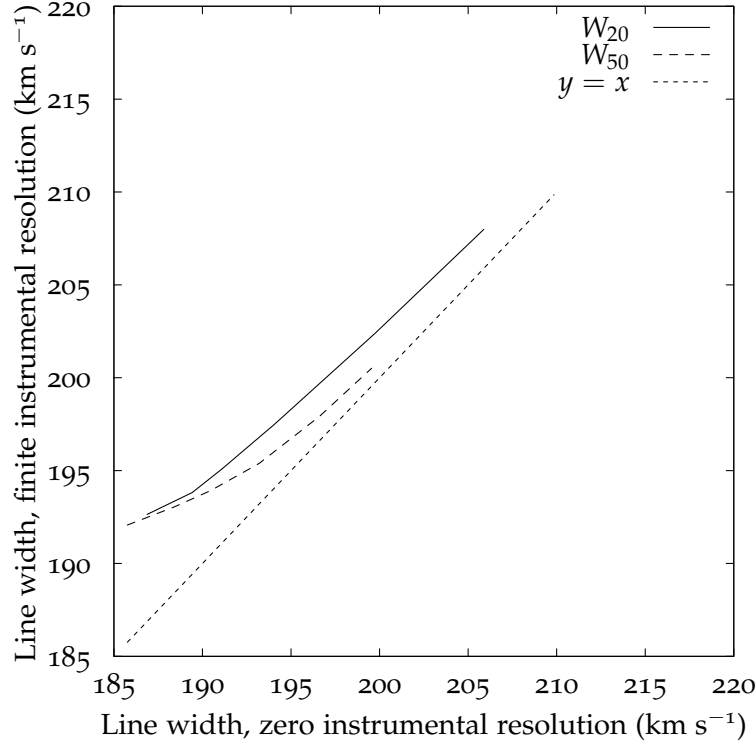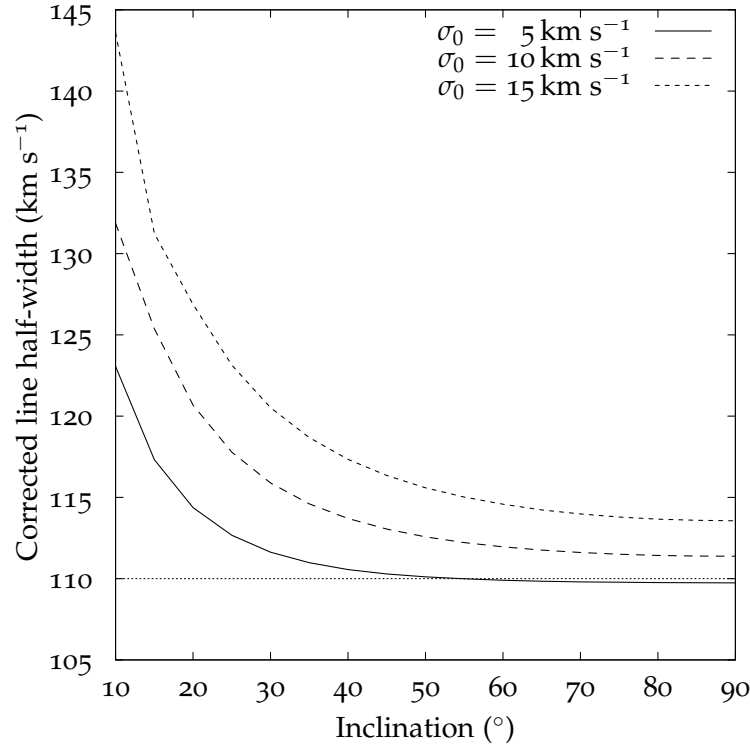

Figure 4.32: Instrumental resolution corrected line widths (W_{20} and W_{50}) vs. zero instrumental resolution line widths for NGC 4157. If the instrumental resolution correction is perfect, then the two lines should lie on $y = x$, also plotted in the figure.

Figures 4.33 and 4.34 show the corrected line widths for W_{20} and W_{50} in this case. As was the case with zero instrumental resolution, the corrected line half-widths are higher than v_{flat}.

For NGC 4157, the instrumental and turbulence corrected line half-widths using VSR's method are very similar to the ones obtained with just the turbulence corrected line widths in the case of zero instrumental resolution. The instrumental and turbulence corrected
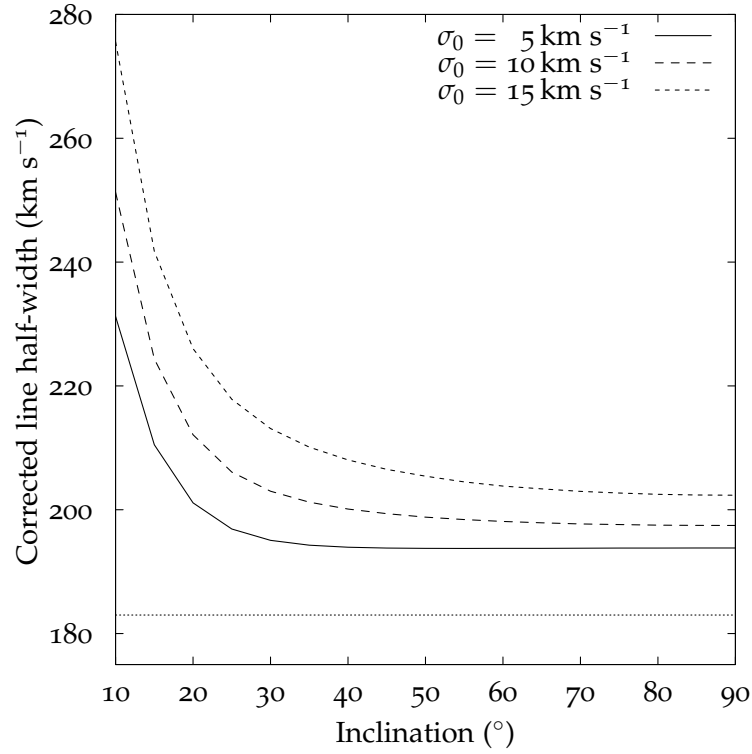
Figure 4.33: The corrected line half-widths for NGC 4157 (as defined by VSR) as a function of inclination for three values of turbulent motions, using W_{20}. The instrumental resolution is finite in this case, and instrumental resolution correction was applied first before applying the other corrections. The solid horizontal line shows v_{flat} (183 km s^{-1}).

half-widths are a bit higher than the turbulence corrected widths, suggesting that for galaxies with faster rotation curves such as NGC 4157, their method under-corrects more than for galaxies with medium rotation curves (such as NGC 4088). To verify this, more testing is needed on a larger sample of galaxies.
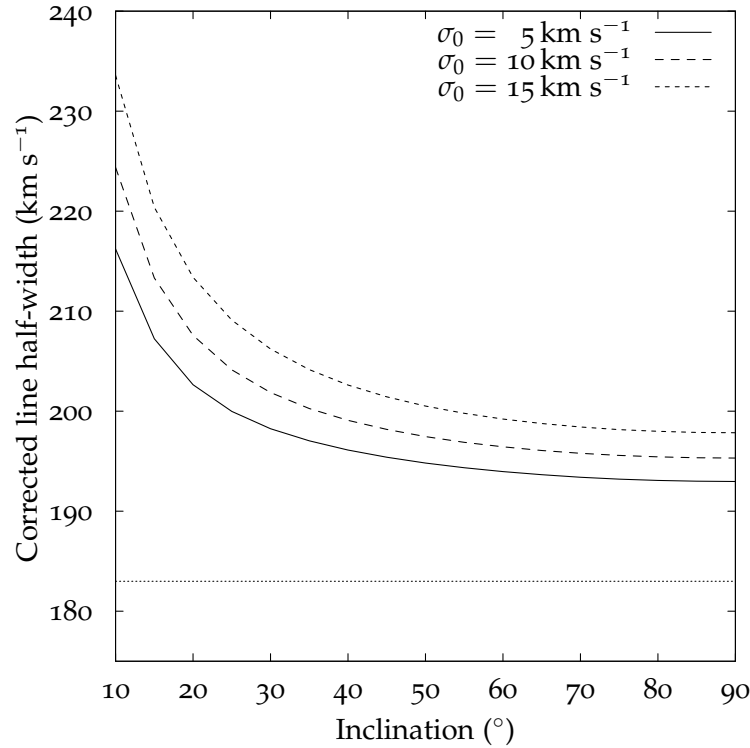
Figure 4.34: The corrected line half-widths for NGC 4157 (as defined by VSR) as a function of inclination for three values of turbulent motions, using W_{50}. The instrumental resolution is finite in this case, and instrumental resolution correction was applied first before applying the other corrections.

4.3.3 UGC 6930

To compare the effect of a finite instrumental resolution on the amount of corrections, UGC 6930 is modeled with the observed value of instrumental resolution, $8.29 \, \text{km s}^{-1}$, and the instrumental resolution correction as defined by VSR is applied on the line widths at 20% and 50% of the peak. These corrected widths are then plotted against the corresponding widths with zero instrumental resolution. The results for W_{20} and W_{50} are shown in Figure 4.35. As expected, the difference between the instrumental resolution corrected widths and widths with zero instrumental resolution approaches zero for high turbulence motions. The instrumental resolution correction as defined by VSR, and shown in equation 1.30 does not completely correct for the instrumental resolution broadening for this galaxy as well.

Figure 4.36 shows the instrumental resolution, turbulence, and inclination corrected line widths (using W_{20}) for UGC 6930 for various values of turbulent velocities and inclinations using VSR's methods. Figure 4.37 shows the same data, but for W_{50}.

Comparing the figures with figures 4.27 and 4.28, the instrumental resolution and turbulence corrected line half-widths are a poorer match to v_{max} and v_{flat} than the turbulence corrected line widths with zero instrumental resolution. The result is surprising, because VSR's method is optimized to work better when both the corrections are

Figure 4.35: Instrumental resolution corrected line widths (W_{20} and W_{50}) vs. zero instrumental resolution line widths for UGC 6930. If the instrumental resolution correction is perfect, then the two lines should lie on $y = x$, also plotted in the figure. The line widths are corrected for instrumental resolution effects as proposed by VSR.
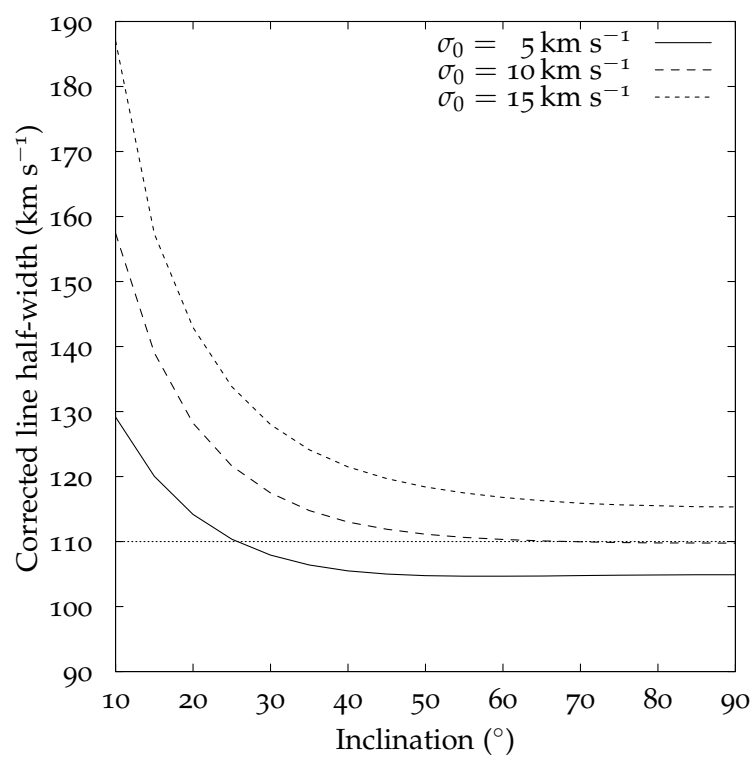
Figure 4.36: The corrected line half-widths for UGC 6930 (as defined by VSR) as a function of inclination for three values of turbulent motions, using W_{20}. The instrumental resolution is finite in this case, and instrumental resolution correction was applied first before applying the other corrections.

applied than when only turbulence correction is applied for galaxies with zero instrumental resolution. This indicates that the instrumental resolution correction they use might be ill-suited for small galaxies (low rotation speeds), but more testing is needed before this claim can be verified.

Figure 4.37: The corrected line half-widths for UGC 6930 (as defined by VSR) as a function of inclination for three values of turbulent motions, using W_{50}. The instrumental resolution is finite in this case, and instrumental resolution correction was applied first before applying the other corrections.

4.3.4 *Effects of turbulent motion and instrumental resolution corrections*

Given the results above, the following conclusions can be made:

- The amount of correction due to finite instrumental resolution of the observing telescope does not yield the line width that would be observed in case of zero instrumental resolution.

- The corrected line half-widths do not match well with either v_{flat} or v_{max}. The effect of instrumental corrections seems to worsen the determination of v_{flat} or v_{max} from the line widths for smaller galaxies (low rotation speed) and possibly for larger galaxies (high rotation speed) as well, but this needs more testing.

- Also, the fact that the TF relation has relatively low intrinsic scatter in it implies that either the assumption that the corrected line width represents v_{flat} or v_{max} is wrong; or that finding a way of determining v_{max} or v_{flat} more accurately should decrease the scatter in the TF relations even more. The second case assumes that $v_{\text{max}}$and/or v_{flat}have an intrinsic value in the TF relation. They may not, and the line widths with zero turbulence and zero instrumental resolution (intrinsic line widths) corrected for inclination may be more valuable for use in the TF relation.

The above results also apply to the other simulated galaxies from chapter 3.

4.4 EFFECT OF TURBULENT MOTION CORRECTION ON LINE WIDTHS

In this section, I discuss the errors in the turbulence motion correction in the line profiles. The method proposed by BGPV is, in general, less efficient in correcting for the turbulence effects than the methods given by TFq and VSR, and therefore, only the latter two methods are discussed in this section.

4.4.1 *Using real galaxies*

First, for the 7 galaxies modeled in chapter 3, I calculate the intrinsic line widths of those galaxies by using their published rotation curves and surface density profiles, and setting the instrumental resolution and turbulence motions in the galaxies to be zero. After that, I calculate the 'corrected' line widths by first modeling the galaxies with finite turbulent velocities, and applying turbulence motion corrections on the line widths thus obtained. For corrected line widths obtained using TFq's method, the instrumental resolution is set to zero while modeling the galaxies. For VSR's method, the instrumental resolution is set to the actual value of instrumental resolution from observations. The reason for using finite instrumental resolution for VSR's method is that their instrumental and turbulence correction methods work together. As mentioned in section 4.3, the instrumental

resolution correction used by them is lower than needed, and therefore, their turbulent motion correction algorithm needs to correct for the deficiency in the instrumental correction as well. For TFq's case, they did not use any correction due to instrumental broadening, hence to study the effect of their corrections, the instrumental resolution used in that case is zero.

Figures 4.38 and 4.39 show plots of the ratio of the intrinsic line widths to the corrected line widths (using W_{20} and W_{50} respectively) as a function of the intrinsic line widths for the 7 galaxies. The intrinsic and corrected line widths are corrected for inclination using equation 1.12. If the corrections are accurate, the ratio should be 1. If, on the other hand, the corrections are biased with respect to the galaxy rotation speed, we should see a dependence of this ratio on the intrinsic line width.

From the two figures, the ratio deviates from 1 by as much as 10% in some cases. Particularly, for UGC 6930, which has the slowest rotation curve in the sample, the errors are large. The amount of deviation from 1 does not seem to have a dependence on the intrinsic line width. The result for UGC 6930 may indicate that the errors are particularly large for slowly rotating galaxies.

For all galaxies except UGC 6930, the corrections from VSR's method work better for W_{20}. The corrections using TFq's method work better for W_{50}. As stated earlier, both corrections can deviate from the intrinsic line widths by as much as 10%.
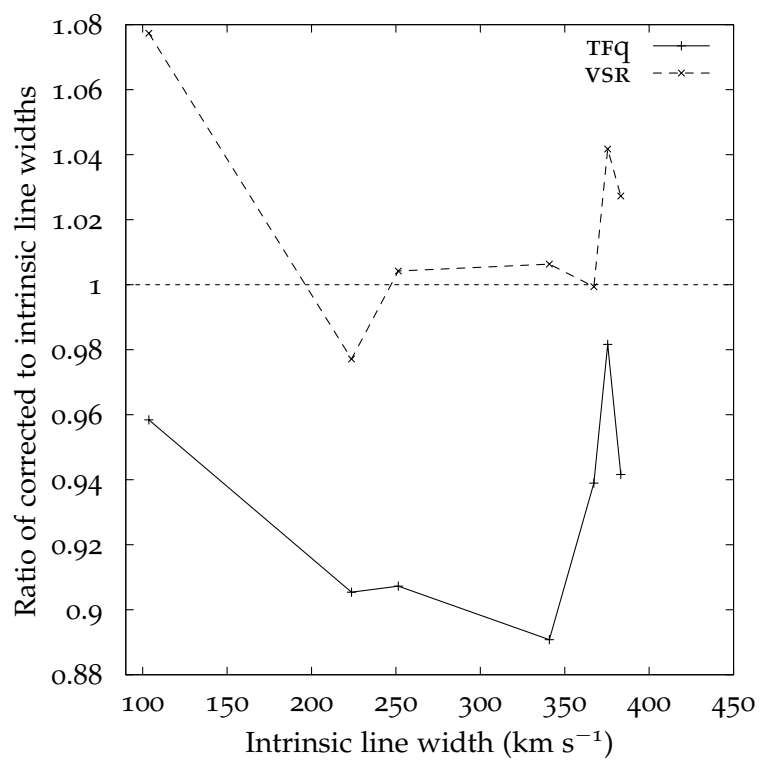
Figure 4.38: A plot of the ratio of corrected line widths to the intrinsic line widths using W_{20} as a function of the intrinsic line widths for various galaxies. The line widths are corrected for inclination.
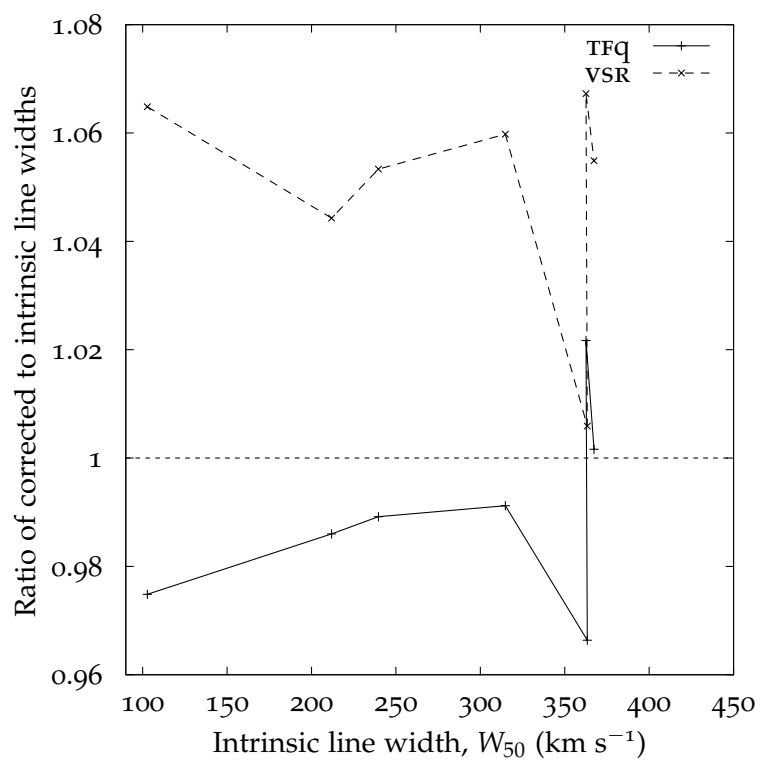
Figure 4.39: A plot of the ratio of corrected line widths to the intrinsic line widths using W_{50} as a function of the intrinsic line widths for various galaxies. The line widths are corrected for inclination.

4.4.2 *Using scaled rotation curves*

In order to further see the effects of these corrections as a function of the intrinsic line widths, a galaxy can be modeled with its rotation curve scaled appropriately to get different intrinsic line widths. All other parameters of the galaxy, such as inclination angle, surface density profile, are kept the same, so this method studies the effects of these corrections only on the intrinsic line profile widths. Also, since the rotation curve is scaled in order to get different intrinsic line widths, the effects due to a particular rotation curve *shape* are minimized as well. While the results obtained in this manner could depend upon the density distribution, inclination, and the rotation curve shape, it is still instructive to see how the two methods of turbulence and instrumental resolution correction work in such a case. For this exercise, three galaxies are used: UGC 6930, NGC 4088, and NGC 4157. These three galaxies cover the range of rotation speeds for the 7 galaxies modeled in chapter 3, and also cover different rotation curve shapes.

The galaxies were modeled by scaling their rotation curves so that the maximum rotation velocity, v_{max}, was 75, 100, ..., 300 km s^{-1} respectively. Figures 4.40, 4.41, and 4.42 show the effect of applying the corrections for UGC 6930, NGC 4088, and NGC 4157 respectively. The plots show the results using W_{20}, but the plots for W_{50} are similar.

The plots have the same *y*-range, to allow easy comparison between galaxies.
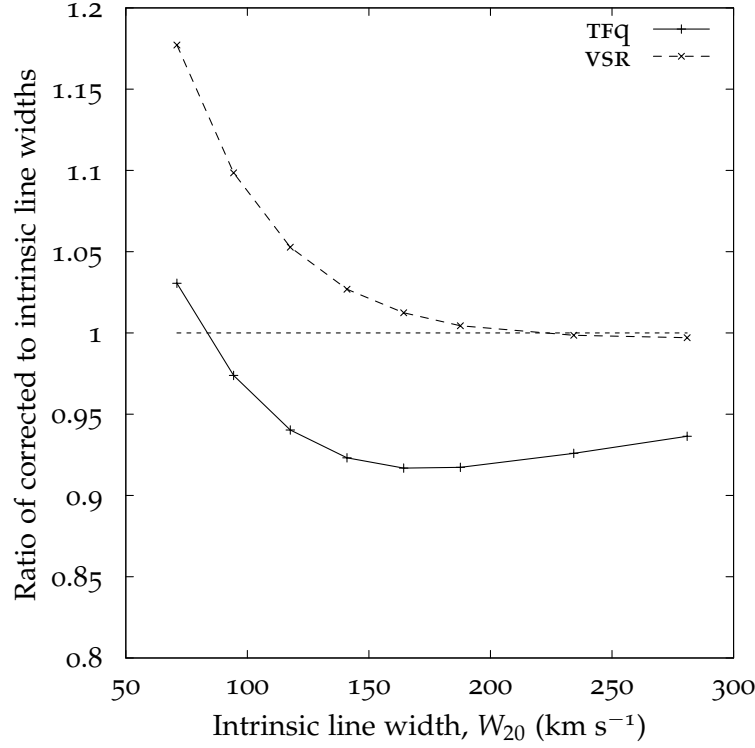
Figure 4.40: A plot of the ratio of corrected line widths to the intrinsic line widths using W_{20} as a function of the intrinsic line widths for UGC 6930. The intrinsic line width of UGC 6930 was changed by scaling its rotation curve. The line widths are corrected for inclination.

Based upon these plots, the turbulence (and instrumental resolution, in case of VSR) corrected line widths are biased as a function of the intrinsic line widths. The galaxies with smaller rotation speeds have corrected widths that are consistently higher (VSR) or lower (TFq) than the galaxies with higher rotation speeds. This has important implications on the TF relation because it changes the slope of the
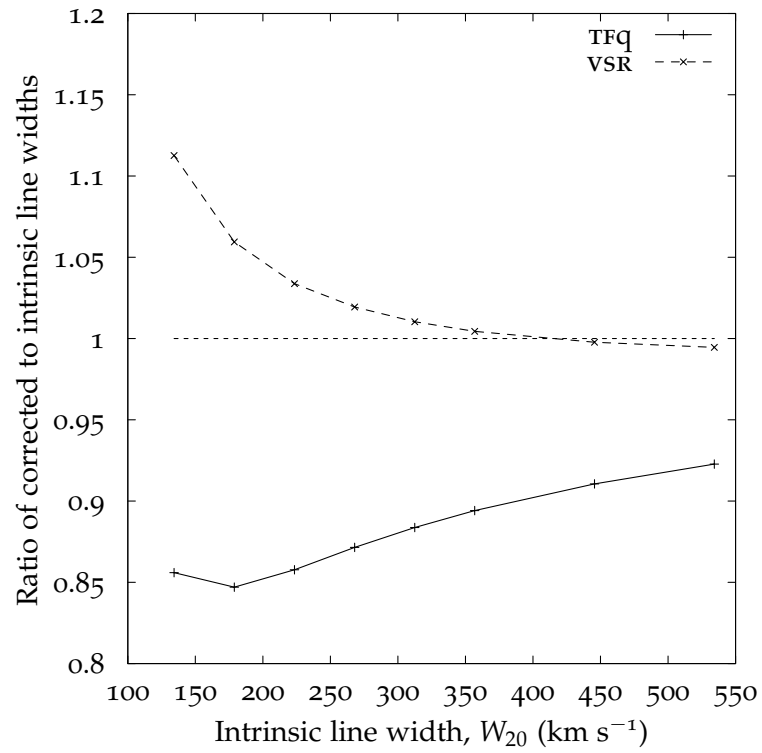
Figure 4.41: A plot of the ratio of corrected line widths to the intrinsic line widths using W_{20} as a function of the intrinsic line widths for NGC 4088. The intrinsic line width of NGC 4088 was changed by scaling its rotation curve. The line widths are corrected for inclination.
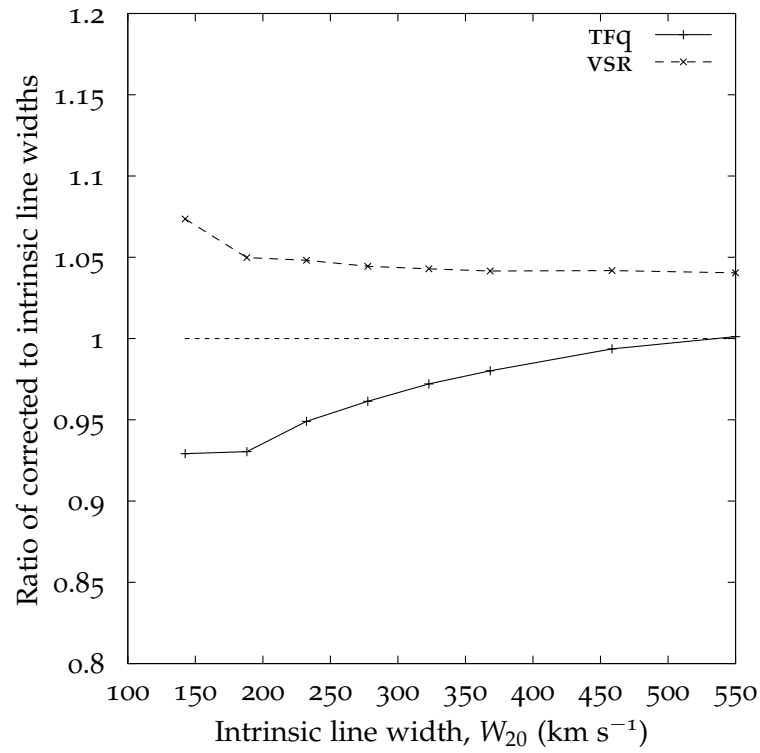
Figure 4.42: A plot of the ratio of corrected line widths to the intrinsic line widths using W_{20} as a function of the intrinsic line widths for NGC 4157. The intrinsic line width of NGC 4157 was changed by scaling its rotation curve. The line widths are corrected for inclination.

relation depending upon the amount and the sign of bias in the corrections. Data from more simulations of real galaxies is needed before a change in this slope can be determined.

5

CONCLUSION AND FUTURE RESEARCH

> 'Would you tell me, please, which
> way I ought to go from here?'
> 'That depends a good deal on where
> you want to get to.'
> 'I don't much care where –'
> 'Then it doesn't matter which way
> you go.'
>
> Lewis Carroll, *Alice's Adventures in*
> *Wonderland*

In this chapter, I present a summary of the main results, conclusions, and some directions for future research.

5.1 SUMMARY

I have created a 3-dimensional model of neutral hydrogen (HI) in disk galaxies, with the aim of understanding the connection between galaxy kinematics and HI line widths. Another aim of the model is to use it to understand the effect of different corrections, such as corrections due to turbulent motions, finite instrumental resolution, on various galaxies. The model also serves as a useful test for consistency in the observed data.

The model uses data such as rotation curves, surface density profiles, derived from radio observations of galaxies, and then synthesizes their HI line profiles. Using simple rotation curves and surface density profiles, and also observational data for 7 galaxies, the model generates accurate HI line profiles of galaxies.

Using the published rotation curves, inclinations, and surface density profiles for 7 galaxies, the model does fairly well in creating the line profiles that match the observations. For some galaxies, such as UGC 6930 and NGC 4088, the inclination angles need to be changed slightly from their published values in order to achieve a better match to the observed line profiles. This is an example of the inherent uncertainties associated with measuring the inclination angles and rotation curves. Based upon the results for simple HI distributions and rotation curves, the model reproduces their line profiles to a high degree of accuracy. The line profiles created for real galaxies using the model do not show such degree of accuracy. Part of the reason for this is inaccuracies in the parameters determined from the observations. Thus, the model can be used to understand the data determined from such observations and serves as a check on such data.

The use of the model to create HI line profiles, and then applying the most commonly used corrections in the literature shows that the corrections for turbulent motions and finite instrumental resolutions are not accurate (see chapter 4). In particular, the corrections applied

by using VSR's methods are too low, while those applied by TFq are too high. More importantly, the corrections are biased in the sense that the over- or under-correction is inversely related to the rotation speed of galaxies. Thus, galaxies with slower rotation curves have higher errors in corrected line widths than galaxies with faster rotation curves (see figures 4.40–4.42). This changes the slope of the TF relations.

One of the reasons for the corrections being too large or too small is that the effect of broadening due to both random motions and finite instrumental resolutions is estimated assuming broadening due to a Gaussian in velocity domain having a width defining the random motions and/or instrumental resolutions. This is simplistic. Another reason could be that because the line profiles are a result of a convolution of the appropriate Gaussians with the intrinsic line profiles having zero random motions and zero instrumental resolution. This convolution brings the peaks of the intrinsic line profile down, and the value of peak-reduction is dependent on the turbulent motions as well as the instrumental resolution (section 3.2.2). Thus, *for a given galaxy*, determining the line widths at a certain fraction of the peak of the HI line profile has a far less physical meaning than determining it at a certain fixed flux level. Varying the instrumental resolution and/or turbulent motions in a galaxy will cause the line widths to be determined at different flux levels.

Looking at figure 3.8, it seems that there are points on the line profile of the simple galaxy where the line profile width seems to be fairly independent of the turbulent velocity. This is the subject of discussion in appendix C. As mentioned in the appendix, there exist points on the HI line profiles of galaxies where such a width can be determined. However, determination of such a width without the simulation is not easy, and needs more investigation before it can be done successfully (if at all).

5.2 FUTURE WORK

An ambitious, but useful project would be to create a 'library' of simulated HI line profiles and then compare the effects of the methods of line-width corrections on them. In particular, figures like 4.40 could then be created with real galaxies instead of using scaled rotation curves. That should give us more insight into the exact biases introduced by the various line-width correction algorithms. Also, with such a library at hand, useful correlations between rotation curve shapes, surface density distributions, inclinations, and other galaxy properties on the line profile shapes, the errors in the corrected line widths using conventional algorithms, etc., can be determined. Once the turbulence independent line widths (W_I) for all the galaxies in the library are found, it would be possible to do an analysis of their dependence on many of the observed galaxy properties. In partic-

ular, one should be able to study the correlation between W_I and the turbulent motions, maximum slopes of the rising and the falling edges of the line profiles, the integrated H I flux, the peak H I flux, the fraction of the peak at which W_I is defined, etc. With enough galaxies, a principal component analysis or a similar approach should prove very useful in exploring these correlations, and isolating the most significant independent parameters defining W_I.

Another extension to the current model, which is partly underway, would be creating H I 'channel maps', which are values of H I flux as a function of three variables: the two-dimensional position on the sky and the velocity (or frequency). The model can then create such a 'data cube', and the cube can then be directly compared to the data cube obtained from aperture synthesis observations. Similarly, another addition to the model (also partly underway) will be to create position-velocity (p-v) diagrams of the galaxies. Position-velocity diagrams are plots of H I intensity as a function of position (along the major or minor axis) and observed (optical) velocity. Comparison of the simulated p-v diagrams with the observed p-v diagrams should tell us more about the distribution of H I in the galaxy.

An important additional feature addition to the model is the ability to add many of the properties of H I in real galaxies, such as flaring, warping, and high-velocity clouds.

The current emphasis of the modeling process is in two directions. First, the database of simulated galaxies needs expansion, possibly to

various different types of galaxies in different environments. Second, the ability to create channel maps and p-v diagrams in order to further test the model and the consistency of observations. Both of these projects are currently in progress.

A

ALGORITHMS

> Let us try the concept of an algorithm with that of a cookbook recipe. A recipe presumably has the qualities of finiteness (although it is said that a watched pot never boils), input (eggs, flour, etc.), and output (TV dinner, etc.), ...
>
> Donald E. Knuth, *The Art of Computer Programming*

A.1 CREATING HI LINE PROFILES

Section 2.3 describes the galaxy software model. In this section, I will explain the algorithms used in creating line profiles using the software model.

After the line-of-sight velocity of each cell is determined using equation 2.5, the line profile for the whole galaxy is determined by first assuming that the turbulent velocity σ_0 and the instrumental resolution, R are both zero. In this case, the line profile from each cell is a delta function at the line-of-sight velocity of the cell, with the area under the delta function equal to the density of the cell. The

term 'delta function' with an area a here means a Kronecker delta function with peak a.

The model creates the H$_I$ line profile for a galaxy which is a set of (v_j, f_j) values, where v_j denotes a velocity and f_j is the flux density at that velocity ($j = 1, 2, \ldots n_{\text{lp}}$). The velocity values are separated by $v_{j+1} - v_j$ (v_res in appendix B). The velocity separation is uniform ($v_{j+1} - v_j = \delta v,\ \forall j$). In general, the line-of-sight velocity v_i of the ith cell will not coincide with any particular v_j, but will lie between v_j and v_{j+1} for some j. In order for better accuracy, the H$_I$ flux from cell i is divided proportionately to velocities v_j and v_{j+1}.

After calculating the line profile for $\sigma_0 = 0$ and $R = 0$, the actual line profile is calculated by convolving it with a Gaussian representing the broadening of the line profile due to the two effects (see equation 1.26).

A.2 DETERMINING LINE WIDTHS

In order to accurately determine the line widths, the peak of the calculated H$_I$ line profile is found. Then, the flux values surrounding the peak flux (one on each side) are found. A parabola is fitted to the three flux values, and the peak of the parabola is used as the peak H$_I$ flux. The peak determined in this way is slightly higher than the maximum value of the calculated line profile.

After that, the velocities on the rising edge are found where the flux becomes just greater than the required fraction of the peak. Linear interpolation is used to determine the velocity v_l where the flux would be equal to the required fraction of the peak. The same procedure is then repeated for the falling edge of the line profile to give v_h, the velocity at which the flux on the falling edge is at the required level. The line width is then determined as $W_l = v_h - v_l$.

A.3 FINDING TURBULENCE-INDEPENDENT LINE WIDTHS

The galaxy inclination angle is changed from 10° to 90° (from close to face-on to edge-on), and at each inclination, the galaxy is modeled at turbulent velocities ranging from $2 \, \mathrm{km \, s^{-1}}$ to $20 \, \mathrm{km \, s^{-1}}$.

For any given inclination, the line profiles for all the values of random motions are then used to determine the turbulence independent line width, W_I at that inclination. In order to do that, the peak flux of the line profile with the highest value of turbulent velocity $f_{p,20}$ is used. The line widths at flux levels $0, 0.1 f_{p,20}, \ldots, f_{p,20}$ are determined, and the level at which the scatter in the widths is the least is determined. This step is then repeated for flux levels close to the level just determined, and again the line width with minimum scatter is determined. This procedure is repeated until the amount of relative change in the scatter in the line widths is $\leq 1 \times 10^{-8}$.

B

BASIC USE OF THE MODEL

> 'It is certainly an idea you have there,' said Poirot, with some interest.
> 'Yes, yes, I play the part of the computer. One feeds in the information –'
> 'And supposing you come up with all the wrong answers?' said Mrs. Oliver.
> 'That would be impossible,' said Hercule Poirot.
> 'Computers do not do that sort of a thing.'
> 'They're not supposed to,' said Mrs. Oliver, 'but you'd be surprised at the things that happen sometimes.'
>
> Agatha Christie, *Hallowe'en Party*

Here, I describe the use of the model to create line profiles, and comparing them with the observed line profiles.

B.1 FILES

The model is implemented in Python. It also uses scipy (Jones et al., 2001–), numpy, and matplotlib modules in order to create and plot the line profiles.

The files in the model are:

galaxy.py This file implements the module `galaxy`. The module defines the `Galaxy` `class` object. The `class` has methods to create a galaxy, create its line profile, and helper functions to plot the line profile in various formats, etc.

constants.py This file makes the definitions of some of the commonly used constants available to all the other files.

util.py Utility functions are defined in this file. They are used by *galaxy.py*, but the functions defined in this file are generic enough that they could be used in other places as well.

data.py Defines a class and associated methods to ease reading of data from files.

parse.py Contains definitions of functions to parse and return values read from configuration files. The functions defined in this file take care of error handling, making the code in *galaxy.py* much more compact.

A galaxy to be modeled needs its files in a subdirectory of the main galaxy module. The subdirectory name identifies the galaxy. For example, for modeling the galaxy NGC 4157, a subdirectory named n4157 is needed, which contains the files that define the galaxy and its properties. In the following description, I assume that the galaxy being modeled is NGC 4157, but the description applies to any

galaxy being modeled, with appropriate changes in filenames and directory names.

In the directory `n4157`, the file `n4157.cfg` contains the galaxy parameters, as well as parameters defining an observation of the galaxy. An example configuration file is shown in Figure B.1.

```
# Configuration file for NGC 4157
distance = 11.5              # Mpc
i = 82.0                     # Inclination, degrees
a = 22290.8                  # Semi-major axis, pc
nx = 1001                    # Number of cells in x
nz = 1                       # Number of cells in z
rot = 0.0                    # Rotation angle in degrees
s = 1.0                      # vdx/vdz, according to BGPV
vd = 10.0                    # vdx (or vdy), km/s
vhel = 774.1                 # Heliocentric velocity, km/s
sd_bhw = 8.7                 # Beam half-width, in arcmin
v_res = 19.88                # Instrumental resolution, km/s
sd_lp = 'n4157.lp.gbt.dat'   # File for single-dish line profile
sy_lp = 'n4157.lp.ver.dat'   # File for synthesis line profile
lp_rms = 1.34e-3             # RMS noise per channel in Jy
```

Figure B.1: A sample galaxy configuration file.

B.2   A SAMPLE RUN

In order to model a galaxy, first, the `galaxy` module needs to be loaded (in the examples in the chapter, >>> denotes the Python prompt):

```
>>> import galaxy
```

After loading the module, the galaxy needs to be created:

```
>>> g = galaxy.BasicGalaxy('n4157')

WARNING: a[22290.8] > rmax[18956.2] in n4157/vc.dat, extrapolating
```

This creates a galaxy object g, which is used to model NGC 4157. The warning message tells the user that the rotation curve specified in vc.dat file does not go out to the maximum radius of the galaxy, so the model extrapolated the rotation curve to make things consistent. For an explanation, see section 3.3.

Once the galaxy is created, one can query some of its parameters:

```
>>> g.i

82.0

>>> g.mass

3332293966.0580502

>>> g.int_flux

106.94791935509707

>>> g.name

'n4157'
```

The inclination angle (in degrees) is g.i, which is 82° as specified in the configuration file. Also, based upon the surface density profile, the galaxy HI mass is available as g.mass (in this case, it is $3.3 \times 10^9 \, M_\odot$). Also, since the HI mass is known, the integrated HI flux can be calculated from equation 2.2. The HI flux for NGC 4157 should be 106.9 Jy km s^{-1}. The galaxy name is available as g.name.

After creating the galaxy, the line profile for the galaxy can be created:

```
>>> g.line_profile()
```

This creates the galaxy line profile, that can be accessed directly as `g.lp`. Based upon the noise per channel specified in the configuration file, the noisy line profile is available in `g.lp_noisy`.

After the line profile is created, the galaxy line widths are known:

```
>>> g.w20
413.14142576376651
>>> g.w50
388.97705334057366
>>> g.get_w_level(40)
396.26399694777871
```

The above commands list W_{20}, W_{50} and W_{40} for the galaxy.

To plot the line profile, or to write the line profile data (optical velocity and flux density) to a file, `g.plot_lp()` and `g.write_lp()` can be used:

```
>>> g.plot_lp(show=True, color=True, plot_sd=False, plot_sy=True)
>>> g.write_lp()
```

The first command above plots the line profile as a function of heliocentric optical velocity and shows the plot on the screen. The synthesis line profile is plotted as well, to allow comparison of the observed line profile with the calculated one (the synthesis and/or single dish profiles are assumed to be in files specified in the configuration file). The second command saves the line profile data in a file,

for analysis later. `g.plot_lp()` can also save the line profile directly to a file instead of showing it on screen:

```
>>> g.plot_lp(show=False)
```

The default format for the saved files is encapsulated postscript, but it can be changed by specifying the `fname` parameter to `plot_lp()`. The plot format is determined from the extension of the filename specified in the `fname` parameter.

While creating a galaxy, any galaxy parameter can be changed from the value specified in the configuration file:

```
>>> g = galaxy.BasicGalaxy('n4157', i=60)
```

The above statement creates a galaxy with inclination 60° instead of the default inclination specified in the configuration file.

A full list of parameters that can be specified in the configuration file or while creating a galaxy is shown in table B.1. The parameters specified on the commandline have precedence over the parameters specified in the configuration file, which in turn, have precedence over the default values, if any.

Parameter	Symbol	Module parameter	Default value
Distance	d	distance	$10\,\mathrm{Mpc}$
Inclination	i	i	$90°$
Semi-major axis	a, b	a, b	$1.5 \times 10^4\,\mathrm{pc}$
Number of cells in x- and y		nx, ny	61
Number of cells in z		nz	1
Rotation angle	ψ	rot	$0°$
Turbulent velocity	σ_x	vdx	$10\,\mathrm{km\ s^{-1}}$
σ_x / σ_z	s	s	1
Heliocentric velocity	v_{hel}	vhel	$0\,\mathrm{km\ s^{-1}}$
Single dish beam half-width		sd_bhw	$10'$
Velocity resolution for line profiles		vdiff	$1\,\mathrm{km\ s^{-1}}$
Instrumental resolution	R	v_res	$5\,\mathrm{km\ s^{-1}}$
RMS noise per channel		lp_rms	$1\,\mathrm{mJy}$

Table B.1: Galaxy parameters that can be specified on the commandline or in the configuration file.

C

CALCULATION OF TURBULENCE INDEPENDENT LINE WIDTHS

> All right – I'm glad we found it out detective fashion; I wouldn't give shucks for any other way.
>
> Tom Sawyer (1884)

From Figure 3.8 in section 3.2.2, it can be seen that there are points on the line profile for a constant circular speed, uniform surface density galaxy where the line width seems to be fairly independent of the turbulent velocity. If such line widths exist for all real galaxies, then they could serve as a basis for use in the TF relation. In this appendix, the line profiles for the galaxies in chapter 3 are calculated at various values of turbulence velocities and inclinations, and a quantitative approach is used to determine the turbulence independent line widths (W_I), if they exist at all.

At any given inclination, a galaxy's line profiles are calculated for turbulent velocities ranging from $2 \, \text{km s}^{-1}$ to $20 \, \text{km s}^{-1}$. For these line profiles, a flux level is iteratively determined at which the line profile width is fairly independent of the turbulent velocity. This is done by minimizing the standard deviations in the line profile

widths as a function of the flux level. Note that since the widths are measured at a certain flux level for all values of random motions, and also that turbulent motions affect the peak flux in a line profile (see section 3.2.2), the flux level does not correspond to a constant fraction of the line profile peak.

Figure C.1 shows a plot of the standard deviation (in a root-mean-square sense) of the line widths (W_I) as a function of inclination angle for the galaxies modeled in section 3.3.
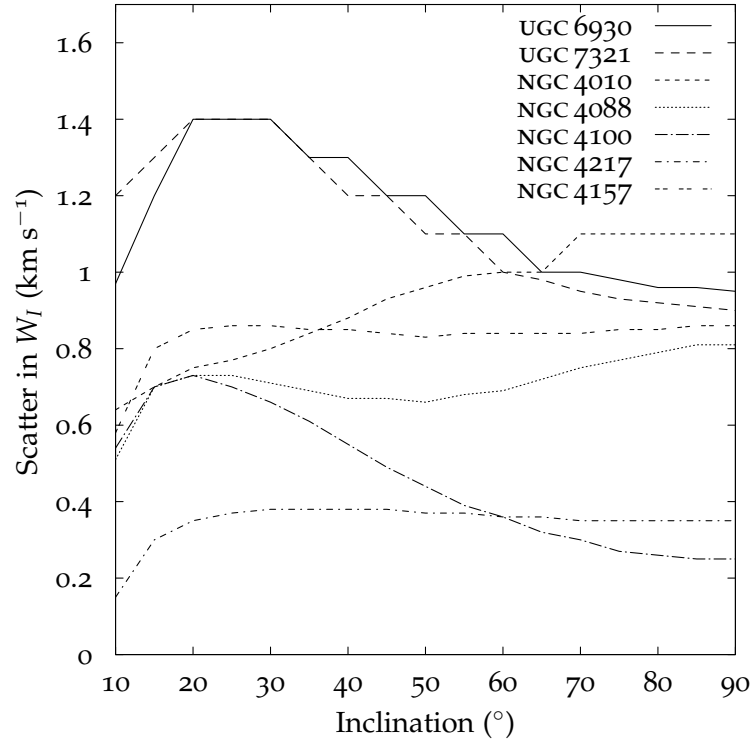
Figure C.1: A plot of the scatter in W_I (turbulent independent line width) as a function of inclination angle for various galaxies.

Figure C.2 shows the inclination corrected line half-widths using W_I and without applying any additional (turbulence or instrumental resolution) corrections on them.
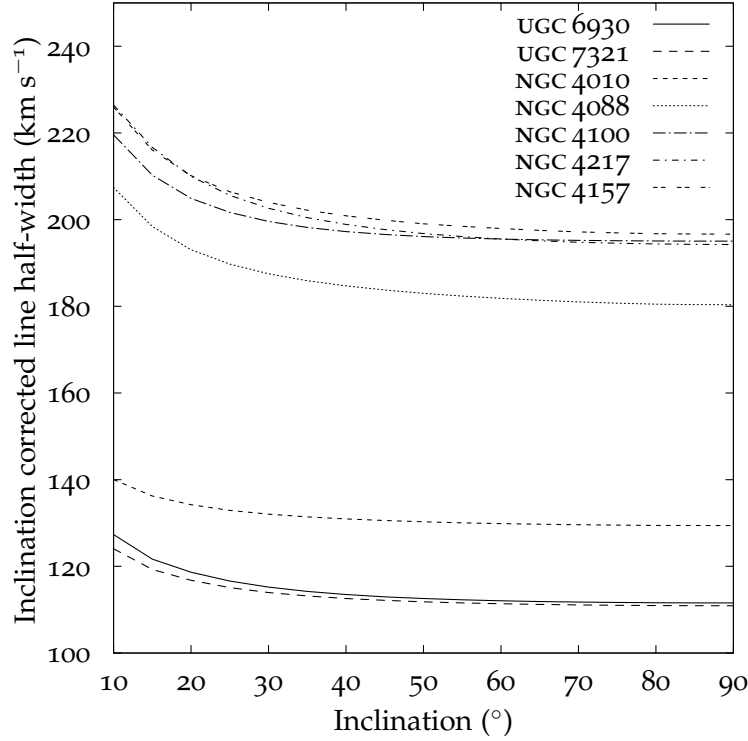
Figure C.2: A plot of the inclination corrected line half-widths (using W_I) as a function of inclination angle for various galaxies.

The scatter in all the galaxies is quite small, with the maximum scatter being $1.4\,\mathrm{km\,s^{-1}}$. Given that the results apply in the range of inclinations from $10°$ to $90°$, and random motions in the range $2\,\mathrm{km\,s^{-1}} - 20\,\mathrm{km\,s^{-1}}$, the small magnitude of this scatter looks promising if a method of determining the flux level for which the value of W_I can be determined.

Also, in Figure C.2, the corrected half-widths are fairly constant upto inclination angles of $\approx 30°$, and therefore, W_I seems to be a good candidate for use as (corrected) line widths in the TF relation.

For the galaxies above, W_I was determined by changing the turbulent motions, and then minimizing the scatter. To be applicable for real galaxies, this width should be easily determined from the single dish line profile of galaxies, and other observable galaxy parameters.

D

DATA SOURCES AND TELESCOPES

This research has made use of various data sources, this appendix lists all of them.

- This research has made use of the SIMBAD database, operated at CDS, Strasbourg, France.

- This research has made use of the NASA/IPAC Extragalactic Database (NED), which is operated by the Jet Propulsion Laboratory, California Institute of Technology, under contract with the National Aeronautics and Space Administration.

- We acknowledge the usage of the HyperLeda database (Paturel et al., 2003)

- A part of the research involved observations of galaxies with the Green Bank Telescope (GBT), operated by the National Radio Astronomy Observatory (NRAO). The NRAO is a facility of the National Science Foundation operated under cooperative agreement by Associated Universities, Inc.

REFERENCES

> There are no answers, only cross-references.
>
> ———————————————
> Weiner's Law of Libraries

Begeman, K. G. 1987, PhD thesis, Kapteyn Institute

Binggeli, B., Sandage, A., & Tammann, G. A. 1985, *AJ*, 90, 1681

Binney, J. & Merrifield, M. 1998, Galactic Astronomy (Princeton University Press)

Bottinelli, L., Gouguenheim, L., Fouqué, P., & Paturel, G. 1990, *A&AS*, 82, 391

Bottinelli, L., Gouguenheim, L., Paturel, G., & de Vaucouleurs, G. 1983, *A&A*, 118, 4

Bringhurst, R. 2004, The elements of typographic style, 3rd edn. (Hartley and Marks Publishers)

Broeils, A. H. 1992, PhD thesis, Univ. Groningen, (1992)

Burstein, D. & Heiles, C. 1978, *ApJ*, 225, 40

de Vaucouleurs, G. 1959, Handbuch der Physik, 53, 275

de Vaucouleurs, G. & de Vaucouleurs, A. 1964, Reference Catalogue of Bright Galaxies (University of Texas Press)

—. 1972, *PASP*, 84, 461

de Vaucouleurs, G., de Vaucouleurs, A., & Buta, R. 1983, *AJ*, 88, 764

Dickey, J. M. 2002, in Astronomical Society of the Pacific Conference Series, Vol. 278, Single-Dish Radio Astronomy: Techniques and Applications, ed. S. Stanimirovic, D. Altschuler, P. Goldsmith, & C. Salter, 209–225

Fouqué, P., Bottinelli, L., Gouguenheim, L., & Paturel, G. 1990, *ApJ*, 349, 1

García-Ruiz, I., Sancisi, R., & Kuijken, K. 2002, *A&A*, 394, 769

Giovanelli, R., Haynes, M. P., Herter, T., Vogt, N. P., Wegner, G., Salzer, J. J., da Costa, L. N., & Freudling, W. 1997, *AJ*, 113, 22

Goldberg, D. 1991, ACM Comput. Surv., 23, 5

Haynes, M. P., Giovanelli, R., Salzer, J. J., Wegner, G., Freudling, W., da Costa, L. N., Herter, T., & Vogt, N. P. 1999, *AJ*, 117, 1668

Haynes, M. P., van Zee, L., Hogg, D. E., Roberts, M. S., & Maddalena, R. J. 1998, *AJ*, 115, 62

Heidmann, J., Heidmann, N., & de Vaucouleurs, G. 1972, *MmRAS*, 75, 85

Hewitt, J. N., Haynes, M. P., & Giovanelli, R. 1983, *AJ*, 88, 272

Holmberg, E. 1946, Lund Obs. Medd. II, 117, 1

Holmberg, E. 1958, Meddelanden fran Lunds Astronomiska Observatorium Serie II, 136, 1

Hubble, E. P. 1926, *ApJ*, 64, 321

Jones, E., Oliphant, T., Peterson, P., et al. 2001–, SciPy: Open source scientific tools for Python

Kahan, W. 2004, How futile are mindless assessments of roundoff in floating-point computation?, World-Wide Web document

Kamphuis, J. & Sancisi, R. 1993, *A&A*, 273, L31+

Keel, W. C. 2008, Galaxies and the Universe – Galaxy Classification, http://www.astr.ua.edu/keel/galaxies/classify.html

Kornreich, D. A., Haynes, M. P., Jore, K. P., & Lovelace, R. V. E. 2001, *AJ*, 121, 1358

Longair, M. S. 1994, High energy astrophysics. Vol.2: Stars, the galaxy and the interstellar medium, 2nd edn. (Cambridge: Cambridge University Press)

Matthews, L. D. 2000, *AJ*, 120, 1764

Matthews, L. D. & Wood, K. 2003, *ApJ*, 593, 721

Monniaux, D. 2007, The pitfalls of verifying floating-point computations, arXiv:cs/0701192v4

Paturel, G., Petit, C., Prugniel, P., Theureau, G., Rousseau, J., Brouty, M., Dubois, P., & Cambrésy, L. 2003, *A&A*, 412, 45

Richter, O.-G. & Sancisi, R. 1994, *A&A*, 290, L9

Roberts, M. S. 1975, Radio Observations of Neutral Hydrogen in Galaxies, ed. A. Sandage, M. Sandage, & J. Kristian (Chicago University Press), 309–+

Rohlfs, K. & Wilson, T. L. 2000, Tools of Radio Astronomy, 3rd edn. (Springer)

Sancisi, R. 1999, *Ap&SS*, 269, 59

Sandage, A. 1975, Classification and Stellar Content of Galaxies Obtained from Direct Photography (Galaxies and the Universe), 1–+

Sandage, A., Sandage, M., & Kristian, J. 1975, Galaxies and the Universe (Galaxies and the Universe)

Springob, C. M., Haynes, M. P., Giovanelli, R., & Kent, B. R. 2005, *ApJS*, 160, 149

Stanimirovic, S., Altschuler, D., Goldsmith, P., & Salter, C., eds. 2002, Astronomical Society of the Pacific Conference Series, Vol. 278, Single-Dish Radio Astronomy: Techniques and Applications, ed. S. Stanimirovic, D. Altschuler, P. Goldsmith, & C. Salter

Taylor, G. B., Carilli, C. L., & Perley, R. A., eds. 1999, Astronomical Society of the Pacific Conference Series, Vol. 180, Synthesis Imaging in Radio Astronomy II, ed. G. B. Taylor, C. L. Carilli, & R. A. Perley

Tully, R. B. & Fisher, J. R. 1977, *A&A*, 54, 661

Tully, R. B. & Fouqué, P. 1985, *ApJS*, 58, 67

Tully, R. B., Shaya, E. J., & Pierce, M. J. 1992, *ApJS*, 80, 479

Uson, J. M. & Matthews, L. D. 2003, *AJ*, 125, 2455

van der Kruit, P. C. & Shostak, G. S. 1982, *A&A*, 105, 351

Verheijen, M. A. W. & Sancisi, R. 2001, *A&A*, 370, 765

Yuan, Q.-R. & Zhu, C.-X. 2004, Chinese Astronomy and Astrophysics, 28, 127

INDEX

If you don't find it in the Index, look very carefully through the entire catalogue.

> Sears, Roebuck and co.,
> *Consumers Guide (1897)*

Important references are given in boldface. Italicized numbers indicate fleeting references, whereas numbers in parentheses refer to mere implications or unwarranted extrapolations. Asterisks are used to identify particularly distasteful passages.

> Prof. Peter Schickele, *The Definitive Biography of P. D. Q. Bach*